

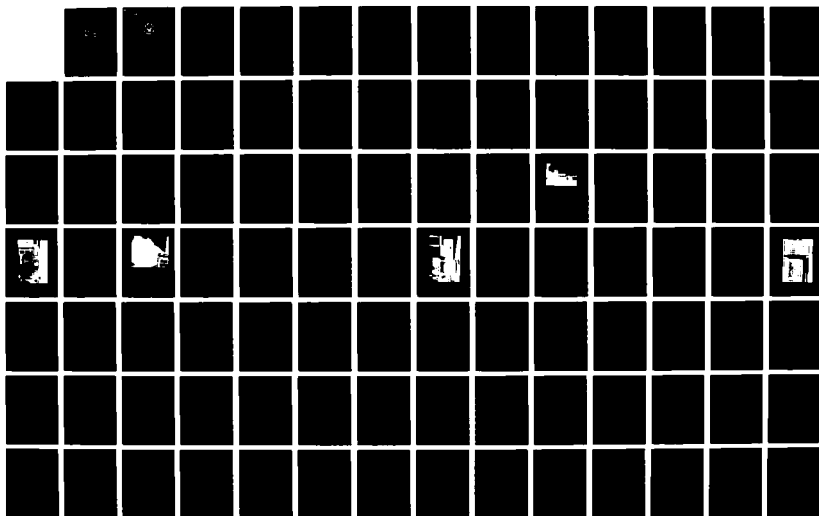
AD-A184 110

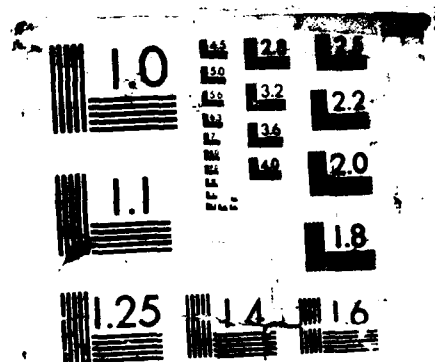
A COMPARISON OF HIGH DAMPING SHAPE MEMORY ALLOYS WITH  
CU-MN-BASED AND FE-CR-BASED ALLOYS(U) NAVAL  
POSTGRADUATE SCHOOL MONTEREY CA J T CRONAUER JUN 87

1/2

UNCLASSIFIED

F/G 11/6. 1 NL





MICROCOPY RESOLUTION TEST CHART

DTIC FILE COPY

②

# NAVAL POSTGRADUATE SCHOOL

## Monterey, California

AD-A184 110



# THESIS

A COMPARISON OF HIGH DAMPING SHAPE MEMORY  
ALLOYS WITH CU-MN-BASED AND FE-CR-BASED  
ALLOYS

by

Joseph Thomas Cronauer

June 1987

Thesis Advisor:

Jeff Perkins

Approved for public release; distribution is unlimited



87 9 1 264

UNCLASSIFIED

SECURITY CLASSIFICATION OF THIS PAGE

## REPORT DOCUMENTATION PAGE

1a REPORT SECURITY CLASSIFICATION <b>UNCLASSIFIED</b>			1b RESTRICTIVE MARKINGS		
2a SECURITY CLASSIFICATION AUTHORITY			3 DISTRIBUTION/AVAILABILITY OF REPORT Approved for public release; distribution is unlimited		
2b DECLASSIFICATION/DOWNGRADING SCHEDULE			5 MONITORING ORGANIZATION REPORT NUMBER(S)		
4 PERFORMING ORGANIZATION REPORT NUMBER(S)			7a NAME OF MONITORING ORGANIZATION Naval Postgraduate School		
6a NAME OF PERFORMING ORGANIZATION Naval Postgraduate School		6b OFFICE SYMBOL (if applicable) Code 69	7b ADDRESS (City, State, and ZIP Code) Monterey, California 93943-5000		
6c ADDRESS (City, State, and ZIP Code) Monterey, California 93943-5000		8a NAME OF FUNDING/SPONSORING ORGANIZATION			
8b ADDRESS (City, State, and ZIP Code)		8b OFFICE SYMBOL (if applicable)		9 PROCUREMENT INSTRUMENT IDENTIFICATION NUMBER	
10 SOURCE OF FUNDING NUMBERS		PROGRAM ELEMENT NO			
		PROJECT NO		TASK NO	
				WORK UNIT ACCESSION NO	
11 TITLE (Include Security Classification) A COMPARISON OF HIGH DAMPING SHAPE MEMORY ALLOYS WITH CU-MN-BASED AND FE-CR-BASED ALLOYS					
12 PERSONAL AUTHOR(S) Cronauer, Joseph T.					
13a TYPE OF REPORT Master's Thesis		13b TIME COVERED FROM TO		14 DATE OF REPORT (Year Month Day) 1987, June	
15 PAGE COUNT 104					
16 SUPPLEMENTARY NOTATION					
COSAT CODES			18 SUBJECT TERMS (Continue on reverse if necessary and identify by block number)		
FIELD	GROUP	SUB-GROUP	High Damping; Shape Memory Alloys; Ti-Ni; Cu-Zn-Al; Fe-Tr-Mo; Cu-Mn-Al		
19 ABSTRACT (Continue on reverse if necessary and identify by block number) The strain dependence and temperature dependence of damping in the thermoelastic martensitic (shape memory) alloys titanium-nickel and copper-zinc-aluminum was compared to predetermined optimum damping behavior in the "quiet" alloys copper-manganese-aluminum and iron-chromium-molybdenum. Damping measurements were taken using a modified resonant dwell technique, in which cantilever beams were evaluated for damping at their first three resonant modes at temperatures between ambient and 110°C. Differential scanning calorimetry was used to correlate microstructural changes with damping capacity. All alloys that were conditioned for high damping showed a trend of low damping at low strains, a strain threshold, and increased damping with strains above the threshold. Damping was directly related to the progress of					
20 DISTRIBUTION/AVAILABILITY OF ABSTRACT <input checked="" type="checkbox"/> UNCLASSIFIED/UNLIMITED <input type="checkbox"/> SAME AS RPT <input type="checkbox"/> DTIC USERS			21 ABSTRACT SECURITY CLASSIFICATION Unclassified		
22a NAME OF RESPONSIBLE INDIVIDUAL Prof. Jeff Perkins			22b TELEPHONE (Include Area Code) (408) 646-2216		22c OFFICE SYMBOL Code 69Ps

UNCLASSIFIED

SECURITY CLASSIFICATION OF THIS PAGE (When Data Entered)

#19 - ABSTRACT - (CONTINUED)

martensitic transformation in the ~~Ti-Ni~~ alloy. The  
Cu-Zn-Al alloy was examined in a condition which did  
not develop high damping. Damping in the ~~Fe-Cr-Mo~~  
alloy was insensitive to temperature change. The  
damping of the Fe-Cr-Mo alloy was sensitive to  
temperature and time at temperature.

TITANIUM NICKEL

Copper,  
Zinc,  
Aluminum

IRON,  
CHROMIUM,  
MOLYBDENUM

UNCLASSIFIED

SECURITY CLASSIFICATION OF THIS PAGE (When Data Entered)

Approved for public release; distribution is unlimited

A Comparison of High Damping Shape Memory Alloys  
with Cu-Mn-based and Fe-Cr-based Alloys

by

Joseph T. Cronauer  
Lieutenant, United States Navy  
B.S., United States Naval Academy, 1981

Submitted in partial fulfillment of the  
requirements for the degree of

MASTER OF SCIENCE IN MECHANICAL ENGINEERING

from the

NAVAL POSTGRADUATE SCHOOL  
June 1987

Accession For	
NTIS GRA&I	<input checked="checked" type="checkbox"/>
DTIC TAB	<input type="checkbox"/>
Unannounced	<input type="checkbox"/>
Justification	
By _____	
Distribution/	
Availability Codes	
Dist	Avail and/or Special
A-1	

QUALITY  
INSPECTED  
2

Author:

Joseph T. Cronauer  
Joseph T. Cronauer

Approved by:

A.J. Perkins  
A.J. Perkins, Thesis Advisor

A.J. Healey  
A.J. Healey, Chairman  
Department of Mechanical Engineering

Gordon E. Schacher  
Gordon E. Schacher,  
Dean of Science and Engineering

### ABSTRACT

The strain dependence and temperature dependence of damping in the thermoelastic martensitic (shape memory) alloys titanium-nickel and copper-zinc-aluminum was compared to predetermined optimum damping behavior in the "quiet" alloys copper-manganese-aluminum and iron-chromium-molybdenum. Damping measurements were taken using a modified resonant dwell technique, in which cantilever beams were evaluated for damping at their first three resonant modes at temperatures between ambient and 110°C. Differential scanning calorimetry was used to correlate microstructural changes with damping capacity. All alloys that were conditioned for high damping showed a trend of low damping at low strains, a strain threshold, and increased damping with strains above the threshold. Damping was directly related to the progress of martensitic transformation in the Ti-Ni alloy. The Cu-Zn-Al alloy was examined in a condition which did not develop high damping. Damping in the Fe-Cr-Mo alloy was insensitive to temperature change. The damping of the Fe-Cr-Mo alloy was sensitive to temperature and time at temperature.

## TABLE OF CONTENTS

I.	INTRODUCTION -----	11
	A. INTEREST AND APPLICATIONS -----	11
	B. BACKGROUND -----	12
	C. MACROSTRUCTURAL DAMPING -----	13
	D. MICROSTRUCTURAL DAMPING MECHANISMS -----	20
II.	OBJECTIVES -----	29
III.	EXPERIMENTAL PROCEDURES -----	30
	A. HEAT TREATMENTS -----	30
	B. DIFFERENTIAL SCANNING CALORIMETRY -----	31
	C. SPECTRAL ANALYSIS -----	36
	D. DAMPING MEASUREMENT REPRODUCIBILITY -----	59
IV.	RESULTS AND DISCUSSION -----	69
	A. SHAPE MEMORY ALLOYS -----	69
	B. INCRAMUTE (CU-MN-AL) -----	83
	C. FE-CR-MO -----	90
	D. 1020 STEEL -----	96
V.	CONCLUSIONS -----	98
VI.	RECOMMENDATIONS FOR FURTHER STUDY -----	99
	LIST OF REFERENCES -----	100
	INITIAL DISTRIBUTION LIST -----	103



# LIST OF TABLES

I.	DAMPING CHARACTERISTICS OF SELECTED METALS AT ROOM TEMPERATURE -----	14
II.	DAMPING SPECIMEN DIMENSIONS -----	38
III.	TI-NI PHASE TRANSFORMATION TEMPERATURES -----	69
IV.	INCRAMUTE'S SDC VARIATION WITH EXPOSURE TIME ----	90

## LIST OF FIGURES

1.1	Damping Factor -----	16
1.2	Quality Factor -----	17
1.3	Phase Diagram of Copper-Manganese Binary System -----	22
1.4	Phase Diagram of Iron-Chromium Binary System -----	28
3.1	Schematic of Differential Scanning Calorimeter and Strip Chart Recorder Output -----	33
3.2	Photograph of Differential Scanning Calorimeter and Strip Chart Recorder -----	35
3.3	Resonant Dwell Method Specimen Geometry -----	37
3.4	First Three Modes of Cantilever Beam Response ---	39
3.5	Modified Resonant Dwell Technique Equipment Arrangement -----	40
3.6	Block Diagram of Equipment Setup to Obtain SDC --	41
3.7	Photograph of Electromagnetic Shaker and Beam Assembly -----	42
3.8	Block Diagram of Equipment Setup to Measure Strain -----	44
3.9	Photograph of Elevated Test Temperature Control System -----	47
3.10	Test Temperature Settling Time at 110°C Set Point -----	49
3.11	Test Temperature Settling Time at 75°C and 40°C Set Points -----	50
3.12	Beam Temperature Characterization -----	52
3.13.	Photograph of Signal Analyzer -----	53
3.14	Broad Band Transfer Function and Coherence -----	55

3.15	Narrow Band Transfer Function and Coherence -----	56
3.16	Narrow Band Transfer Function and Phase -----	57
3.17	Narrow Band Transfer Function Real and Imaginary -----	58
3.18	Broad Band Strain (EU) Distribution -----	60
3.19	Narrow Band Strain (EU) Distribution -----	61
3.20	SDC Data via Half-Power Method -----	66
3.21	SDC Data via Vector Technique -----	67
4.1	Ti-Ni Calorimetry -----	70
4.2	Cyclic Strain Dependence of SDC in 100% Martensitic Ti-Ni -----	71
4.3	Strain Dependence of SDC for Ti-Ni Heated to 57°C-64°C -----	73
4.4	Strain Dependence of SDC for Ti-Ni Heated to 93°C-109°C -----	75
4.5	Strain Dependence of SDC for Ti-Ni Cooled to 40°C-46°C -----	76
4.6	Summary of Damping in Ti-Ni as a Function of Cyclic Strain and of Test Temperature -----	77
4.7	SDC Sensitivity to Temperature Change, at a Constant Strain -----	79
4.8	Comparison of Heating Portions of Ti-Ni Calorimetry and SDC-Temperature Sensitivity Study -----	81
4.9	Comparison of Cooling Portions of Ti-Ni Calorimetry and SDC-Temperature Sensitivity Study -----	82
4.10	Strain Dependence of SDC for Cu-Zn-Al at Room Temperature -----	84
4.11	Strain Dependence of SDC for Cu-Zn-Al Heated to 88°C-105°C -----	85
4.12	Strain Dependence of SDC for INCRAMUTE at Test Temperature 21°C -----	86

4.13	Strain Dependence of SDC for INCRAMUTE at Test Temperature 43°C -----	87
4.14	Strain Dependence of SDC for INCRAMUTE at Test Temperature 66°C -----	88
4.15	Strain Dependence of SDC for Fe-Cr-Mo at Room Temperature -----	92
4.16	Strain Dependence of Fe-Cr-Mo Heated to 36°C-41°C -----	93
4.17	Strain Dependence of Fe-Cr-Mo Heated to 60°C-69°C -----	94
4.18	Strain Dependence of Fe-Cr-Mo Heated to 92°C-109°C -----	95
4.19	Strain Dependence of SDC for 1020 Steel at Room Temperature -----	97

### ACKNOWLEDGEMENTS

The author would like to express his appreciation to Professor Jeff Perkins whose support and guidance made this task a worthwhile and enjoyable learning experience. Gratitude is also expressed to Professor Young Shin for providing meaningful advice on the test technique utilized herein.

Special thanks is extended to the Material Science staff, the Naval Engineering curriculum staff, and the Mechanical Engineering shop staff for their valuable assistance throughout all stages of this project.

Mrs. Cathy Wong and Mr. Bob Hardy of NSRDC are recognized for their continued support of the work being done at the Naval Postgraduate School.

## I. INTRODUCTION

### A. INTEREST AND APPLICATIONS

Noise and vibration are physical realities generated by any dynamic, mechanical system. These physical perturbations have numerous adverse effects on the systems which produce them and upon equipment and personnel in their environment. For example:

- a. reduced or impaired performance of extremely sensitive electronics or alignment-critical physical systems;
- b. shortened fatigue life, and thus service life, of equipment;
- c. elevated ambient noise levels in work spaces, thus increasing potential hearing loss hazards to personnel;
- d. amplification of underwater acoustic emissions of Naval submarine and surface vessels.

Consequently, this principle of noise abatement and vibration control is of critical interest to the Naval service.

Schetky and Perkins [Ref. 1] categorize the noise reduction techniques currently in use as:

1. Isolation: reduced energy transmission between sources and adjoining surfaces that can radiate the energy.
2. Dissipation: attenuation of the energy in isolation pads physically mounted on the structures.

The effectiveness of the present methods must be weighed against the fact that they monopolize considerable valuable

space, add weight, and increase installation costs. These are all precious commodities on naval vessels. Thus Schetky and Perkins detail a viable alternative, in which the structural or machine components themselves are made from high-strength, energy-absorbing, high-damping metals. This thesis is part of a research program aimed at exploring in detail the damping characteristics of these "quiet" alloys from a microstructural point of view, with the aim of understanding and controlling their damping mechanisms and properties.

## B. BACKGROUND

Damping is a property of a structure which describes how rapidly vibration decays once it is excited within that structure. All materials exhibit some degree of vibrational damping capability. This damping capacity has been found to be a function of many variables including geometry, excitation frequency, temperature, stress/strain amplitudes, and material microstructure. Currently most metals utilized in structural and machinery applications have very low damping capacities at the stress magnitudes generated by noise and vibration. A commonly used measure of the vibration damping capability of a material is the specific damping capacity (SDC)--the percent of strain energy that is dissipated per cycle of oscillation. SDC will be described in detail in the next section. High-damping alloys will be regarded here as those with SDC values in excess of 20%.

The SDCs of most conventional structural alloys, including steels, brasses, bronzes, aluminum alloys, and many high-strength alloys, are less than 5%. In the past, gray cast iron has been considered the most energy-absorbing material among common structural alloys, yet its SDC value is merely in the range from 5% to 10%, much lower than the high-damping levels achievable by "quiet metal" alloys (see Table I). Alloy systems on which high-damping alloys can be based include the Cu-Mn, Ti-Ni, Cu-Zn-Al, Cu-Al-Ni, and Fe-Cr systems. [Ref. 1:pp. 202-204]

### C. MACROSTRUCTURAL DAMPING

#### 1. Vibration Damping Theory

A simple and general model which can be used for the case of forced vibration in a structure or system with viscous damping, is known as the Kelvin-Voigt model. This model consists of a mass suspended from a spring and a dashpot in parallel with each other. The general differential equation of motion for this model is of the form:

$$m\ddot{y} + c\dot{y} + ky = F \quad (1.1)$$

where

$m$  = mass

$c$  = viscous damping coefficient

$k$  = spring constant

$y$  = displacement



TABLE I  
DAMPING CHARACTERISTICS OF SELECTED METALS  
AT ROOM TEMPERATURE [Ref. 1:p. 203]

Metal	SDC (%)	Yield Strength ( $10^3$ psi)	Density (gm/cm <sup>3</sup> )
Magnesium (wrought)	49	26	1.74
Cu-Mn alloys (Ingramute, Sonoston)	40	45	7.5
Ni-Ti alloy (Nitinol)	40	25	6.45
Fe-Cr-Al alloy (Silentalloy)	40	40	7.4
High-C gray iron	19	25	7.7
Nickel (pure)	16	10	7.86
Martensitic stainless steel	8	85	7.7
Gray cast iron	6	25	7.8
SAP (aluminum powder)	5	20	2.55
Low-carbon steel	4	50	7.86
Ferritic stainless steel	3	45	7.75
Malleable, modular cast irons	2	50	7.8
Medium-carbon steel	1	60	7.86
Austenitic stainless steel	1	35	7.8
1100 Aluminum	0.3	5	2.71
Aluminum alloy 2024-T4	<0.2	47	2.77
Nickel-base superalloys	<0.2	Range	8.5
Titanium alloys	<0.2	Range	4.5
Brasses, bronzes	<0.2	Range	8.5

$\dot{y}$  = velocity

$\ddot{y}$  = acceleration

F = time-dependent, complex forcing function.

The state solution to Equation (1.1) is of the form [Ref. 2: p. 130]:

$$y = Ye^{i(\omega t - \theta)} = Fe^{i\omega t} / [(k - m\omega^2) + i\omega c] \quad (1.2)$$

where

y = displacement (response)

Y = amplitude of the displacement

$\theta$  = phase angle between response and excitation.

For a single degree of freedom system there occurs a specific frequency,  $\omega_n$ , at which the vibrating structure resonates.

Numerous parameters are utilized to quantify a material's ability to dampen vibration. Their definitions and relationships follow:

- a. Critical damping coefficient ( $c_c$ ) [Ref. 3:p. 50]

$$c_c = 2m\omega_n \quad (1.3)$$

- b. Damping factor ( $\zeta$ ) [Ref. 3:pp. 50-51] (see Figure 1.1)

$$\zeta = \frac{c}{c_c}, \quad 0 \leq \zeta \leq 1 \quad (1.4)$$

- c. Logarithmic decrement ( $\delta$ )--the natural logarithm of the ratio of any two successive amplitudes, in a system exhibiting oscillating free decay [Ref. 3:pp. 30-31]

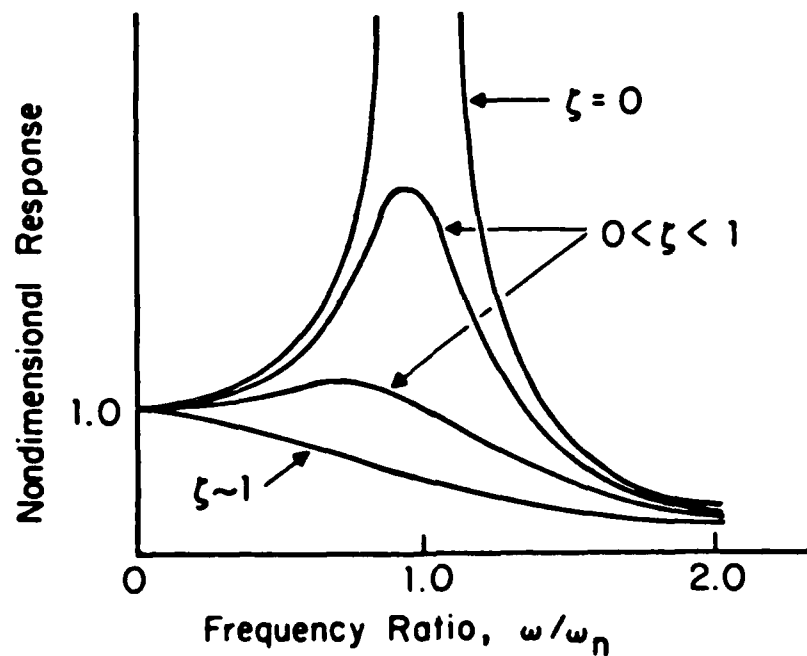


Figure 1.1 Damping Factor

$$\delta = \ln \frac{a_1}{a_2} = \frac{2\pi\zeta}{\sqrt{1-\zeta^2}} \quad (1.5)$$

- d. Quality factor (Q)--a measure of the sharpness of the resonant peak, in forced vibration. Assuming  $\zeta \ll 1$  [Ref. 3:pp. 76-77] (see Figure 1.2)

$$Q = \frac{\omega_n}{\omega_2 - \omega_1} = \frac{1}{2\zeta} \quad (1.6)$$

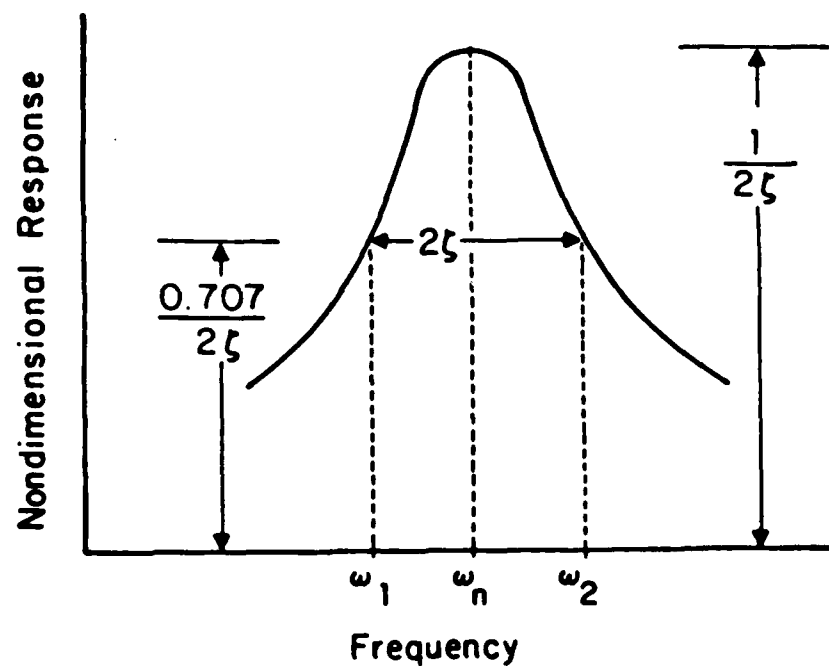


Figure 1.2 Quality Factor

- e. Internal friction ( $Q^{-1}$ ) [Ref. 4:p. 41]

$$Q^{-1} = \frac{\omega_2 - \omega_1}{\omega_n} \quad (1.7)$$

- f. Phase angle ( $\alpha$ )--the angle at which strain lags stress in a metal exposed to cyclic strain [Ref. 5:p. 445]

$$\tan \alpha = Q^{-1} = \frac{\delta}{p} \quad (1.8)$$

This is true provided damping is small.

- g. Specific damping capacity (SDC)--the fractional loss of energy per cycle in an oscillating system [Ref. 5:pp. 444-445]

$$SDC = \frac{A_1^2 - A_2^2}{A_1^2} \quad (1.9)$$

Where  $A_1$  and  $A_2$  are the amplitudes at the beginning and end of the cycle. Assuming that  $(A_1 - A_2)$  is small,

$$SDC = \frac{2(A_1 - A_2)}{A_1} \quad (1.10)$$

Again, if the damping is small,

$$SDC = 2\delta \quad (1.11)$$

The above definitions yield the following relationships, provided damping is small:

$$SDC = 2\pi Q^{-1} = 4\pi\delta \quad (1.12)$$

and therefore,

$$SDC (\%) = 200\pi Q^{-1} = 200\pi \left( \frac{\omega_2 - \omega_1}{\omega_n} \right) \quad (1.13)$$

## 2. Macrostructural Damping Measurement

Numerous techniques have been successfully utilized to measure a material's vibration damping capability. A method which is particularly applicable to the objectives of this thesis, and those of the research project that it supports, is the resonance dwell technique. This procedure

determines the stress/strain and frequency dependence of material damping at engineering stress levels. An additional advantage is the fact that it monitors forced, continuous excitation, rather than observing free decay. An electro-magnetic shaker is utilized to excite the clamped end of a cantilever beam specimen. A low power optical microscope with a rectical is used to measure the beam tip's vertical displacement (specimen response). The response of the supporting system is measured with an accelerometer mounted on the clamp at the root of the beam. These responses are then utilized to determine the specimen's internal friction. Reference 6 details the operation of the apparatus and the calculation of the "loss factor."

Professor Y.S. Shin, of the Naval Postgraduate School, has modified this test technique by measuring the cantilever beam response with an accelerometer rather than the optical microscope. The signals from the input (root) accelerometer and output (beam tip) accelerometer are processed by a spectrum analyzer to produce the vibrating beam's frequency response. A strain gage is mounted at the beam root, in order to measure strain amplitude at modal frequencies.

Part of this thesis was the design and implementation of an elevated temperature control system to study the temperature dependence of a material's damping capacity.

#### D. MICROSTRUCTURAL DAMPING MECHANISMS

In any metallic material there are numerous mechanisms responsible for vibration damping. For high damping "quiet metal" alloys the energy dissipation mechanisms are unique, and closely affiliated to processes of a cooperative type. These include coupled phenomena which link elastic deformation with other physical processes, for instance crystallographic transformations, magnetic transitions, etc. [Refs. 7,8]

##### 1. Shape Memory Alloys

Shape memory alloys have the unique ability to be able to recover from strains which are in the normal range of permanent plastic deformation. Such non-elastic strains, generated by deformation in an appropriate temperature range, will be recovered if heated to a slightly higher temperature. During this heating, these metal alloys regain their original shape. The temperature range for recovery corresponds to a return of the microstructure to the austenitic condition. Some common shape memory alloy systems are Ti-Ni, Cu-Zn-Al, and Cu-Al-Ni. [Ref. 9:p. 130]

It has been firmly established that on the microscopic level, some extent of thermoelastic martensitic transformation is a requirement for shape memory behavior. Typically, deformation mechanisms associated with shape memory behavior are activated by one or both of two situations: (1) deformation-induced transformation of the

high temperature phase to martensite, and/or (2) deformation of existing martensite.

When the thermoelastic martensitic transformation is induced by external stress applied at temperatures above the martensite transformation start temperature ( $M_s$ ), the energy dissipation or damping mechanism is probably affiliated with the chemical free energy hysteresis of stress-induced transformation, and microstructurally with the movement of parent/martensitic interfaces. For the case in which the microstructure is fully martensitic at the outset, that is at temperatures below the martensite transformation finish temperature ( $M_f$ ), the applied stress results in intervariant boundary motion. This rearranging of variants leads to a self-accommodating configuration. In this situation, the energy dissipation mechanism probably originates largely from the hysteresis due to lattice friction upon intervariant boundary motion. [Refs. 10,11]

## 2. Cu-Mn-Based Alloys

An understanding of some of the physical properties of the Cu-Mn alloy system is required to explain its potential microstructural damping mechanisms. Cu-Mn binary alloys display a broad single-phase solid miscibility of Mn in Cu at elevated temperatures. This FCC gamma ( $\gamma$ )-phase, existing above approximately 700°C, is evident in the Cu-Mn alloy system phase diagram (Figure 1.3). [Refs. 12,13] For alloys composed of less than 50% Mn, the FCC  $\gamma$ -phase is



## PHASE DIAGRAM OF CU-MN SYSTEM

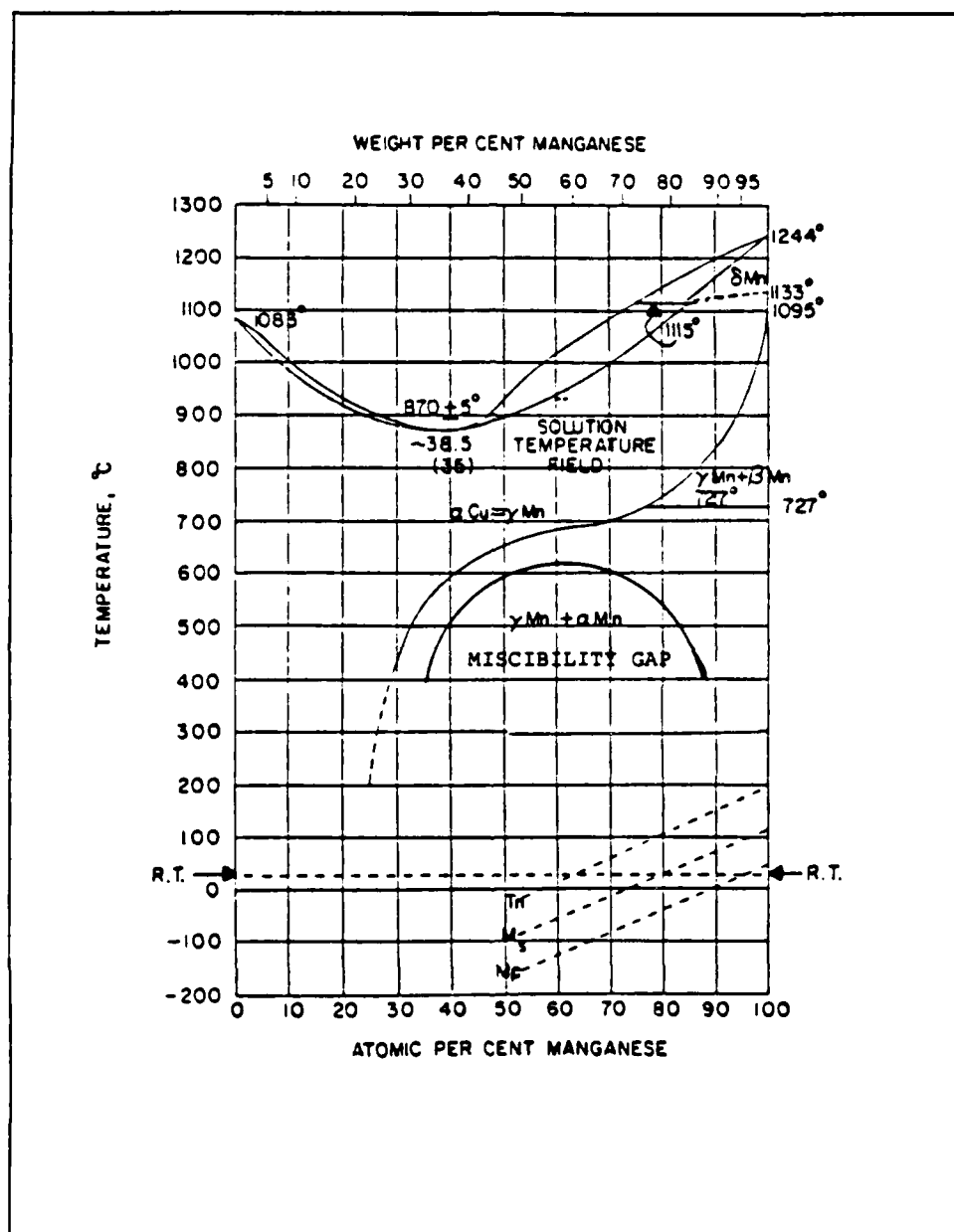


Figure 1.3 Phase Diagram of Copper-Manganese Binary System

retained after quenching to room temperature [Refs. 14,15: pp. 114,119]. These as-quenched Cu-Mn alloys are characterized by low strength, high ductility, and low damping capacity.

A high-damping microstructure can be generated in these alloys by performing a conditioning aging treatment within an intermediate temperature range (300°C to 600°C). Studies of this aging effect have proposed a continuous decomposition process in the  $\gamma$ -phase before the final precipitation of an equilibrium  $\alpha$ -Mn phase. [Ref. 16, p. 4853] This decomposition process is thought possibly to be associated with the presence of a miscibility gap in the Mn-Cu phase diagram (Figure 1.3). The exact location of this miscibility gap is uncertain; Vintaykin, et al. [Ref. 13] established the extent of the gap to be between about 40 and 88 a/o Mn at 700K (427°C) with a curve apex at 60 a/o Mn at about 875K (600°C). The decomposition reaction that is considered to occur during aging within the miscibility gap, results in the formation of fine scale Mn-rich regions [Refs. 16,17,18:pp. 10,106,142]. These Mn-rich areas provide potential sites for the nucleation of a tetragonal (FCT) phase upon quenching. Thus by aging, the FCC to FCT transformation temperature is raised high enough to allow the formation of a tetragonal martensitic twin structure upon cooling to room temperature. It has often been described that a cooperative realignment of the twinned FCT

martensitic microstructure under cyclic stress is the high damping mechanism in these alloys. [Refs. 19,20,21,22:pp. 43,137,2104,451]

Damping in Cu-Mn-based alloy systems has been determined to be dependent on the following conditions [Ref. 23, p. 23-25,31].

a. Aging

Damping capacity should increase with aging time at elevated temperature to a maximum point, after which overaging reduces the damping toward preaged levels.

b. Composition

For the same aging condition, alloys with higher Mn content will have greater damping potential. However, the lower Mn alloys can be properly aged to attain high damping levels.

c. Test Temperature

For high damping capacity to be possible, the test temperature must be less than the Neel temperature ( $T_N$ ).  $T_N$  is a concentration-dependent, critical temperature, below which the atomic magnetic dipoles of adjacent Mn atoms become aligned in an antiferromagnetic (antiparallel) manner, and domains are formed with mismatches of the antiferromagnetic alignment at the domain boundaries [Ref. 24:p. 473]. This arrangement results in zero net magnetism. If test temperature is above  $T_N$ , the

alignment is destroyed [Ref. 24], and high damping cannot be achieved.

#### d. Strain or Stress

Depending on the alloy's thermomechanical history, strain or stress may activate the alloy's damping mechanisms. Generally, damping capacity will increase with applied stress or strain. Eventually, the damping value reaches a peak, after which it decreases with added stress or strain.

### 3. Fe-Cr-Based Alloys

The potential damping mechanisms in ferromagnetic materials are considered to be magneto-mechanical hysteresis loss (primary mode) and dislocation damping (secondary mode). Ferromagnetic materials have the ability to be magnetized and to maintain their magnetic state even in the absence of an applied magnetic field [Ref. 24:p. 464]. Magnetization in ferromagnetic materials is said to be irreversible. This leads into the occurrence of magneto-mechanical hysteresis energy loss (damping). This coupling of magnetism and elasticity effects is explained in Refs. 25 and 26 in the following manner. Ferromagnetic materials contain magnetically ordered regions called domains, within which magnetization is equal to the saturation magnetism. Upon application of a magnetic field or an external stress, the initially randomly oriented domains respond so as to align themselves, either with the magnetic field or in the

direction of the resultant strain. This domain movement results in an irreversible change in the materials physical dimensions and in its magnetization. This irreversible change is known as "magnetostriction." When a stress-strain curve for an unmagnetized ferromagnetic metal is plotted, it shows a strain that exceeds what would be predicted by Hooke's Law. Upon relaxation of loading, the elastic strain diminishes to zero (provided negligible plastic deformation occurs), but the magnetostrictive strain remains. This causes the hysteresis loop. The larger the area of the hysteresis loop, the greater the damping capacity of the material.

The secondary mode of damping in the ferromagnetic materials is known as dislocation damping. Dislocations are line defects within a crystalline material. As the material is cyclically stressed these dislocations move, and thus energy is absorbed (damping).

Some of the most critical factors affecting the damping capacity of Fe-Cr-based alloys are briefly described.

a. Strain or Stress

At low strains damping is relatively low. But as stress is elevated the damping mechanisms are activated, and damping capacity rapidly increases with strain. The damping capacity has been observed to peak at a certain strain level, beyond which the damping diminishes slowly.

This effect is obviously due to the development of some sort of damping saturation condition, the mechanism of which must in some way involve the inhibition of movement of magnetic domain walls. [Ref. 27]

#### b. Chromium Content of the Alloy System

Examining the Fe-Cr binary phase diagram (Figure 1.4) shows the existence of two single-phase solid solution ranges in the 10%-15% Cr-content region. The body-centered cubic (BCC) structured  $\alpha$ -ferrite is ferromagnetic at room temperature, while the face-centered cubic (FCC) structured  $\gamma$ -ferrite is paramagnetic (nonmagnetic) at all temperatures. Thus in order for the alloy to have any potential for high damping, the Cr-content must be sufficiently high to avoid the " $\gamma$ -loop" upon solution treatment. The width of the " $\gamma$ -loop" has been found to increase with the addition of austenizing elements, particularly carbon and nitrogen. [Refs. 28,29:pp. 291,5-2,5-3]

#### c. Test Temperature

A magnetic transformation temperature, known as the Curie temperature, exists for this ferromagnetic alloy at approximately 700°C (see Figure 1.4). At temperatures above the Curie temperature, the added thermal energy sufficiently reduces the magnetization of the ferromagnetic material to allow the domains to become randomly oriented. This results in a complete transition to paramagnetic (and non-damping) behavior. [Refs. 28,24:pp. 291,473]

## Cr-Fe (Chromium-Iron)

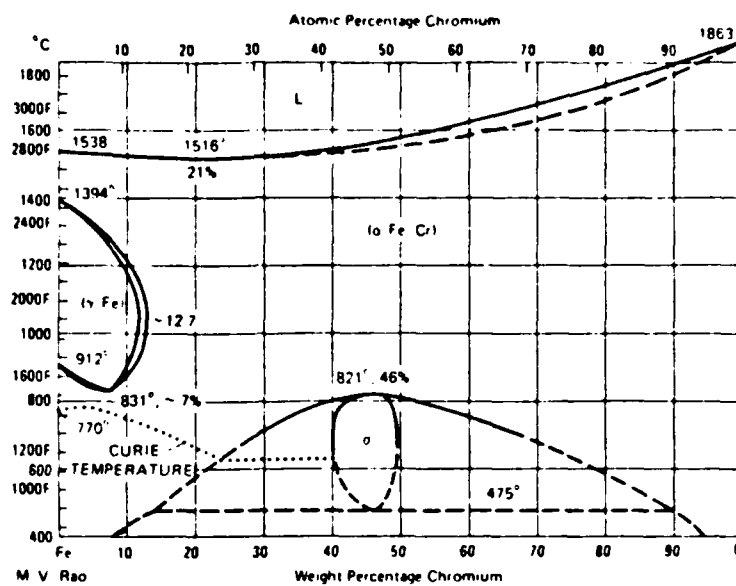


Figure 1.4 Phase Diagram of Iron-Chromium Binary System

## II. OBJECTIVES

The work reported here is part of an ongoing program of research in which quantitative analysis of damping behavior will be used to develop an understanding and means of control of microscopic damping mechanisms in high damping "quiet metal alloys." This research program has been conducted for the last few years at the Naval Postgraduate School under the sponsorship of David W. Taylor Naval Ship Research and Development Center.

The following goals guided the present research:

- To design, construct, and utilize an elevated temperature control system for conducting vibration damping studies
- To determine the strain dependence and temperature dependence of damping in the thermoelastic martensitic (shape memory) alloys Ti-Ni and Cu-Zn-Al
- To verify previously determined optimum damping behavior in quiet metal alloys based on the Cu-Mn-Al and Fe-Cr-Mo alloy systems
- To compare the damping behaviors of the shape memory alloys to the Fe-Cr-based and Cu-Mn-based alloys and explain distinctions between them.



### III. EXPERIMENTAL PROCEDURES

#### A. HEAT TREATMENTS

Summarized below are the heat treatments performed on the various alloys studied in this research.

1. Ti-Ni (Composition 49 a/o Ti, 39 a/o Ni, 10 a/o Cu)

This alloy was tested in the as-cast condition. it was provided in bulk form as a plate with average thickness 0.212 cm.

2. Cu-Zn-Al (Composition 70.6 w/o Cu, 25.8 w/o Zn, 3.6 w/o Al)

This alloy was already fabricated into cantilever beams when provided for this study. These beams were solution treated at 900°C for 20 minutes in a tube furnace, followed by a water quench to room temperature.

3. Fe-Cr-Mo (Composition 84.7 w/o Fe, 11.3 w/o Cr, 2.5 w/o Mo)

This alloy was previously studied by O'Toole [Ref. 30], and the cantilever beams from the earlier work were reused in the present study. O'Toole investigated eight different heat treatments, with variations in annealing temperature and cooling rate. Based on his results, the optimum damping microstructure was developed by annealing one hour at 1100°C, and then furnace cooling to room temperature. A constant flow of argon gas was maintained through the furnace tube throughout the annealing and

cooling processes, in order to minimize oxidation of the metal surfaces.

4. INCRAMUTE (Composition 53.1 w/o Cu, 44/8 w/o Mn, 1.6 w/o Al)

This alloy was previously studied by Reskusich [Ref. 23], and the cantilever beams used in the earlier work were reused in the present research. Reskusich investigated seven different heat treatments, with variations in aging time at 400°C. Based on his results, the optimum damping microstructure was developed by solution treating at 800°C for two hours followed by a water quench to room temperature, then aging at 400°C for 16 hours. These specimens were subsequently stored in a freezer maintained at -22°C, until they were required for testing, in order to prevent any room temperature aging which might affect microstructure and/or damping behavior.

B. DIFFERENTIAL SCANNING CALORIMETRY

Differential scanning calorimetry (DSC) is a thermal analysis technique which can be used to monitor and characterize material reactions or phase transformations. In DSC, the material being studied and a reference material are placed in separate sample pans and covered. The pans are placed in individual sample holders in a thermal block which is under a dynamic atmosphere of inert gas. The material samples are then heated, and/or cooled, at a programmed rate by individual heating elements. The

differential scanning calorimeter (DSC) is shown schematically in Figure 3.1. A differential power control loop maintains the two sample holders at the same temperature, while an average temperature control loop changes the temperature of the sample holders at a programmed rate. The outputs of these control loops are sent to a strip chart recorder. Endothermic transitions, increases in heat capacity of the material, are noted as a power deficit and indicated by an upscale departure from the ordinate baseline on the strip chart. Exothermic reactions are sensed as a power excess and shown as a downscale departure from the baseline (i.e., a pen deflection to the right of the baseline). The ordinate of the strip chart represents heat flow rate (calories/second). The abscissa represents temperature and is calibrated in degrees Kelvin. To conform to these conventions, the reference material is always placed in a certain sample holder (in this case the right hand one). A sketch of an endothermic transition on a strip chart recording is shown in Figure 3.1. [Ref. 31]

The DSC reference sample was made by filling an aluminum sample pan with 99.9% pure aluminum cut from a rod of stock reference aluminum and covering it with an aluminum cover. The mass of the reference sample (including pan and cover) was 0.0713 grams. DSC samples for the materials of interest were prepared following their individual heat treatments. Samples were cut by an oil-cooled high-concentration diamond

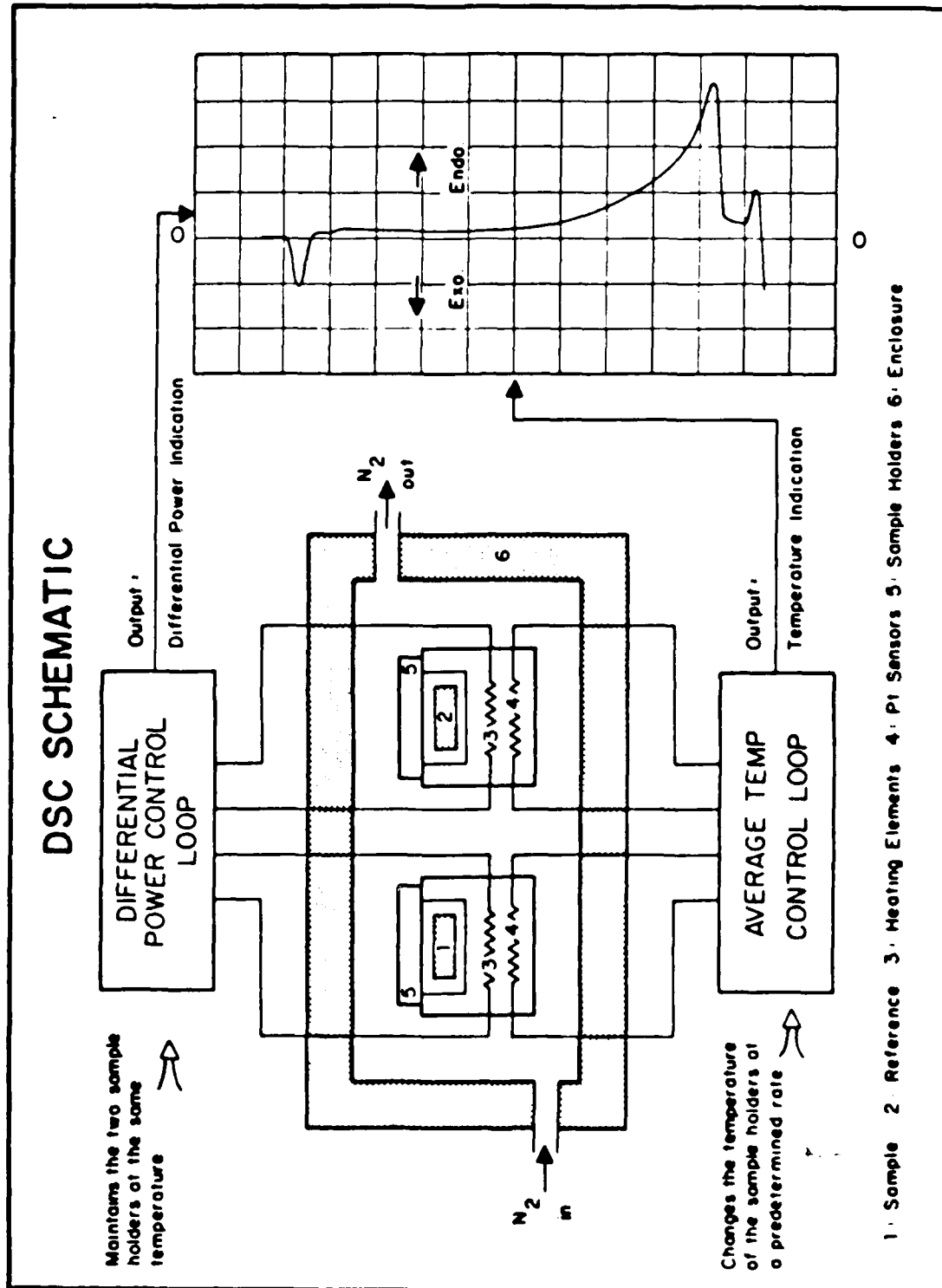


Figure 3.1 Schematic of Differential Scanning Calorimeter and Strip Chart Recorder Output

wafering blade in a low speed saw. Thin slices, approximately 0.5 mm thick, were cut from the extreme edge of the clamped end of the cantilever beam specimens. These slices were cleaned by soaking in ethanol, in order to prevent impurities from influencing DSC results. The DSC samples were constructed such that their mass was approximately equivalent to that of the Al reference sample.

The objective of this portion of the research was to determine whether or not any thermally-activated phase transformations were observable in the alloy within a temperature range ( $22^{\circ}\text{C}$ - $110^{\circ}\text{C}$ ) where damping behavior could be studied. If so, the microstructure changes associated with the phase transformations might be correlated to fluctuations in damping behavior at or near the same temperatures.

Calorimetric measurements were made using a Perkin-Elmer DSC-2C Differential Scanning Calorimeter. The DSC results were recorded on a two-pen Perkin-Elmer Model 56 strip-chart recorder. A photograph of this equipment is shown in Figure 3.2. The DSC sample holders were kept under a dynamic atmosphere of dry nitrogen flowing at 20 ml/min at 20 psig.

Temperature calibration was performed as outlined in the Perkin-Elmer DSC-2C Operating Instructions [Ref. 31:pp. 3-12--3-16]. A calibration standard check proved the temperature measurement accurate to within two degrees Kelvin. Temperature ranges of interest were scanned at

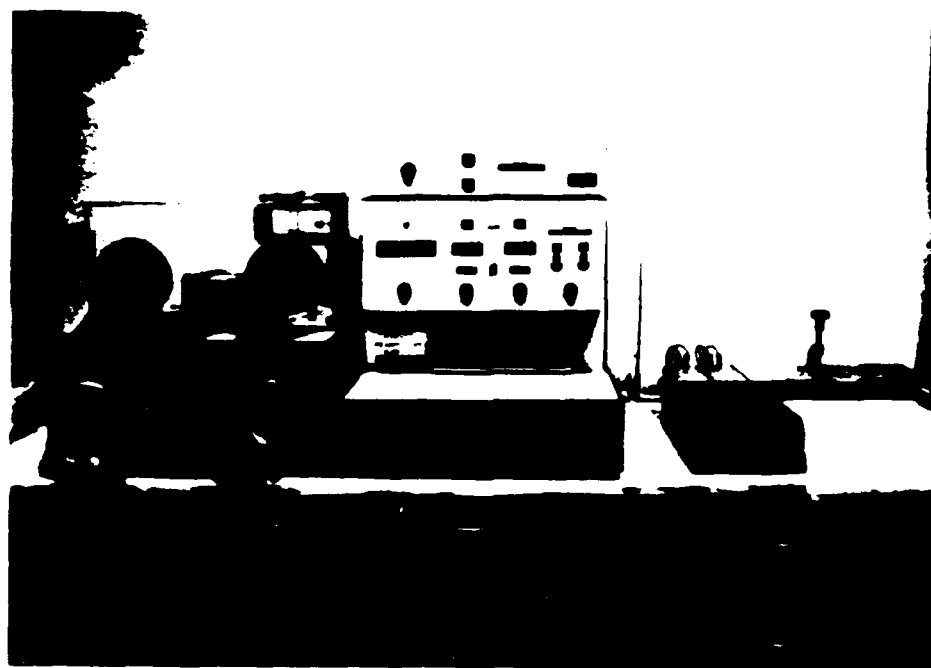


Figure 3.2 Photograph of Differential Scanning Calorimeter and Strip Chart Recorder

programmed rates as low as 10 K/min. for heating and 2.5 K/min. for cooling, in order to obtain maximum resolution. Calibration was done at a scanning rate of 10°/min. Therefore, if any other scanning rate was used, the observed transition temperature must be corrected as follows:

$$T \text{ (true)} = T \text{ (obs.)} - 0.085 (dT/dt) + 0.85 \quad (3.1)$$

where:

$T$  (true) = actual transition temperature

$T$  (obs.) = DSC observed transition temperature

$dT/dt$  = DSC heating or cooling rate.

Since temperature was the only parameter sought here, the ordinate which normally indicates heat flow rate in cal/sec, was not calibrated.

### C. SPECTRAL ANALYSIS

Damping measurements were performed using a modified resonant dwell technique. This method uses forced random vibration to determine loss factor (also known as internal friction, see Equation (1.7)) of cantilever beams by measuring their response to excitation at modal frequencies. The system's input and output were measured by accelerometers mounted just above the beam root and at the beam tip, respectively. The accelerometer outputs were compared by a signal analyzer to produce the transfer function frequency response for the beam. Based on this data, specific damping capacity (SDC) of the beam material was calculated. For each material studied, SDC was determined as a function of strain and as a function of temperature.

The geometry of the cantilever beam specimen is defined in Figure 3.3 [Ref. 6:p. 20]. The beam width and grip length are specified, but the vibrating length ( $L_v$ ) and thickness are left as variables. In some cases, beams used

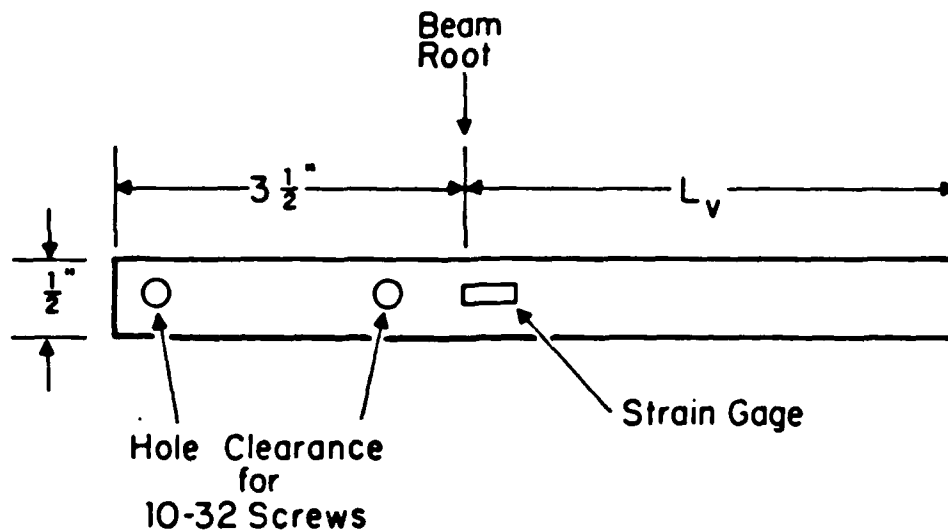


Figure 3.3 Resonant Dwell Method Specimen Geometry

in previous research [Refs. 23,30] were reused for the present measurements. Beam dimensions (following heat treatment, if applicable) are provided in Table II.

When using the technique of modal analysis, use is made of the fact that beams have multiple resonant frequencies. When forced vibration occurs at one of these resonant frequencies, certain points along the beam vibrating length will approach their maximum displacement amplitude. The corresponding shape or response is called the "normal mode"



TABLE II  
DAMPING SPECIMEN DIMENSIONS

ALLOY SYSTEM	THICKNESS (inches)	WIDTH (inches)	VIBRATING LENGTH (inches)
Ti-Ni	0.08	0.54	5.16
Cu-Zn-Al	0.07	0.49	4.47
Fe-Cr-Mo	0.06	0.52	6.99
Cu-Mn-Al	0.08	0.50	4.83
1020 Steel	0.06	0.53	6.38

for that resonant frequency. The first three normal modes for a cantilever beam are depicted in Figure 3.4.

The mode 1 (lowest) resonant frequency is known as the natural frequency,  $\omega_n$ . The first three vibration modes were employed to measure damping in this research. [Ref. 3:pp. 132,198]

A photograph of the equipment utilized in this damping analysis is presented in Figure 3.5. Two basic equipment configurations were used: one measured the transfer function frequency response and the other measured the strain distribution with frequency.

The equipment setup for measuring transfer function is outlined in Figure 3.6. A Scientific-Atlanta SD380Z 2-channel signal analyzer was used to generate a 2V broadband random noise signal, which was amplified at adjustable gains by a MB Dynamics 2125MB power amplifier. The amplified

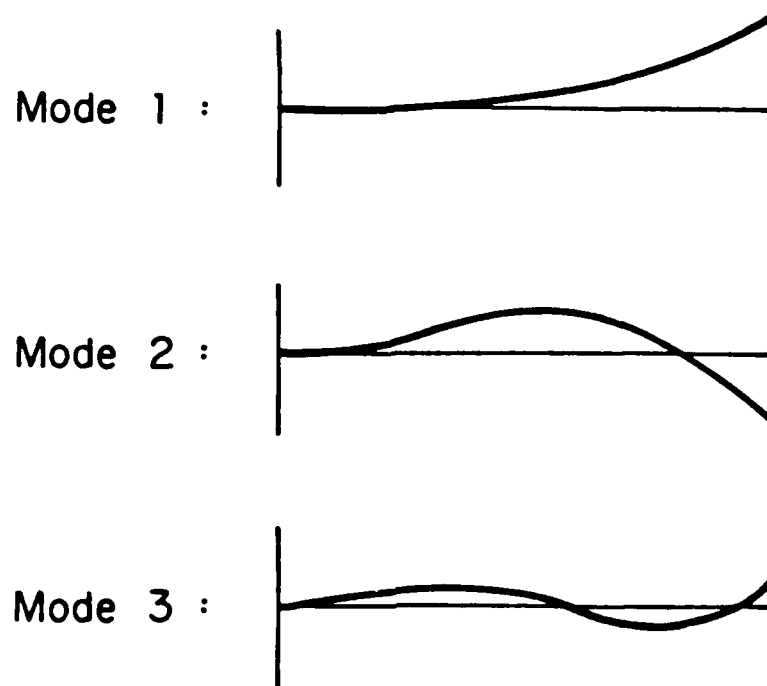


Figure 3.4 First Three Modes of Cantilever Beam Response

signal was used to drive a MB Dynamics PM-25 Vibramate Exciter. This electromagnetic shaker, which is cooled by low pressure air, provides the driving force used to excite the specimen (see Figure 3.7). The excitation force was transmitted to the beam via a "stinger" rod connected to the base of the beam clamp. The beam clamp assembly provides a 3.5 inch grip length on the beam, leaving the remainder of the beam free to vibrate (see Figure 3.3). The jaws of the



Figure 3.5 Modified Resonant Dwell Technique Equipment Arrangement

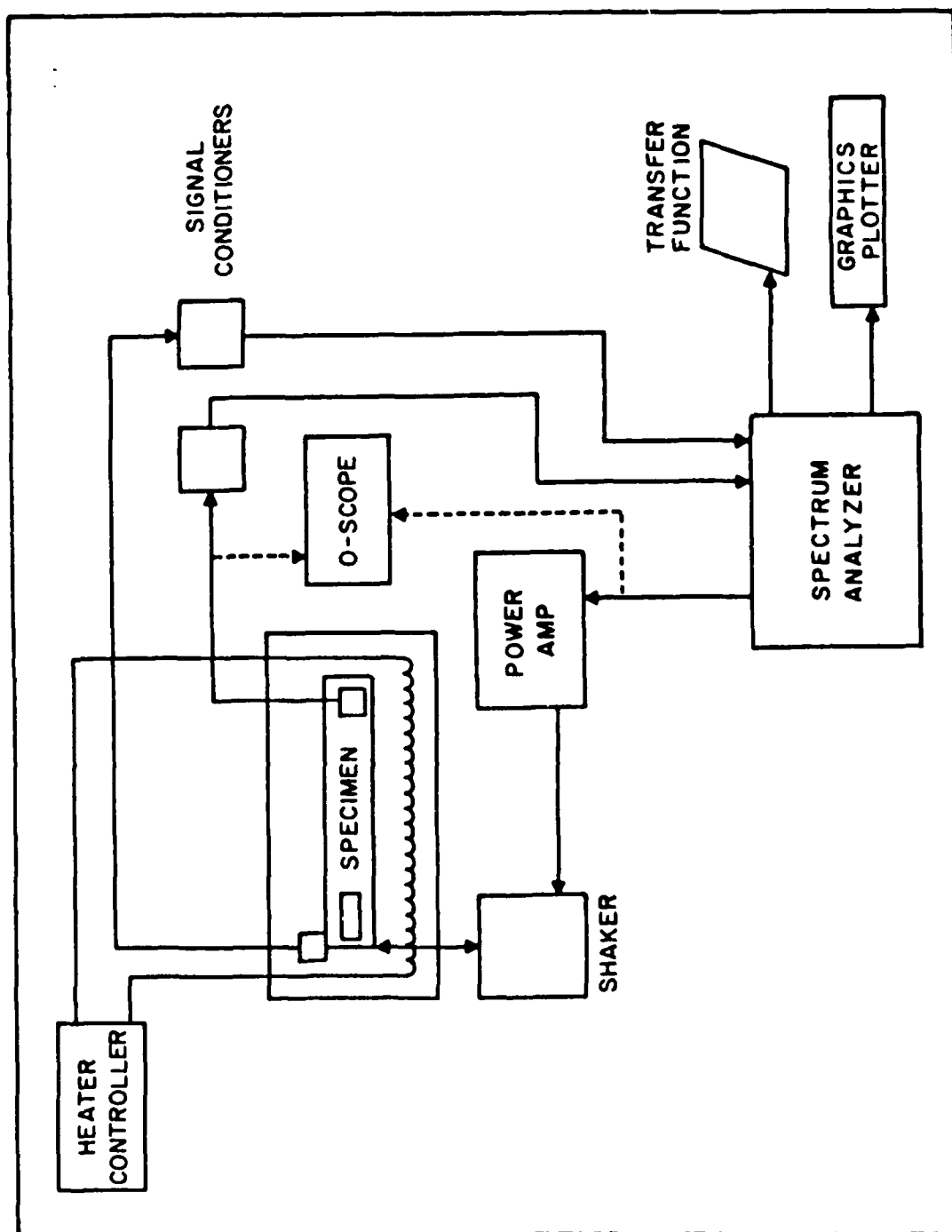


Figure 3.6 Block Diagram of Equipment Setup to Obtain SDC

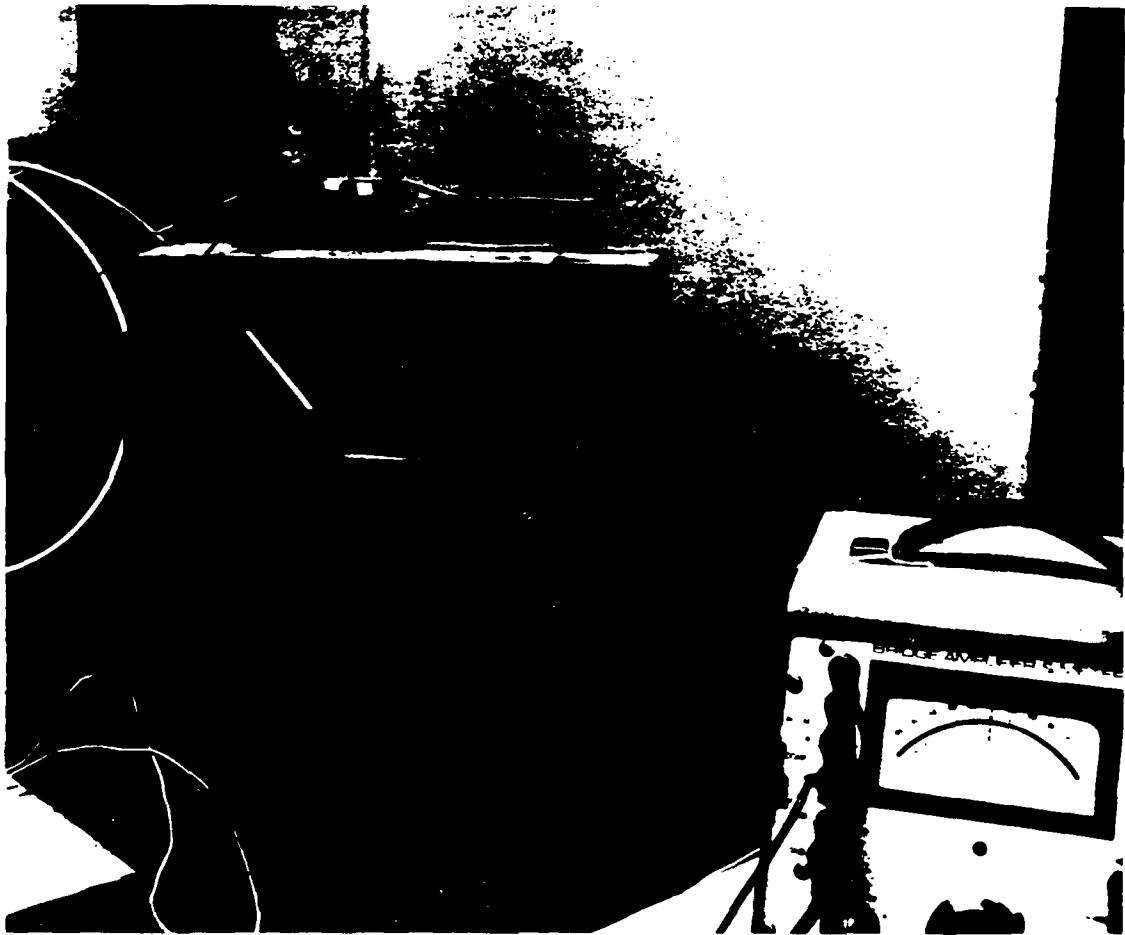


Figure 3.7 Photograph of Electromagnetic Shaker and Beam Assembly

clamp are set back, so that the "stinger" rod, the beam root, and the system input accelerometer (mounted on the top of the clamp) are vertically aligned. The system output accelerometer is mounted at the beam tip. Endevco Model 2250A-10 integral electronics shear accelerometers were used; these generate a voltage which is proportional to

their respective acceleration amplitudes. Each accelerometer was attached via a coaxial cable to an Endevco Model 4416A signal conditioner. These signal conditioners provide a constant-current source of power to the accelerometers, and also amplify the accelerometer voltage output by a factor of ten. The voltage outputs of the signal conditioners were fed into separate input channels of the signal analyzer. The signal analyzer was programmed to calculate the material transfer function response and display this information on the screen. The signal analyzer display can be printed by the attached Hewlett-Packard 7470A plotter, and/or the data can be stored on a micro floppy disk operated within the signal analyzer.

The equipment setup for measuring strain distribution with frequency is diagrammed in Figure 3.8. The excitation signal path to the beam was the same as described previously for the transfer function setup. Only now, the system response was measured by a foil strain gage mounted longitudinally at the beam root (see Figure 3.3). The absolute maximum stress or strain for any mode occurs at the root. The strain gages used throughout the study were Measurements Group, Inc., type CEA-13-250UN-350, with a gage factor of  $2.12 \pm 0.5\%$  and a resistance of  $350 \text{ ohms} \pm 0.3\%$ . Strain induced in the beam causes a change in the length of the elements of the attached strain gage and results in a change in the resistance of the gage. This resistance

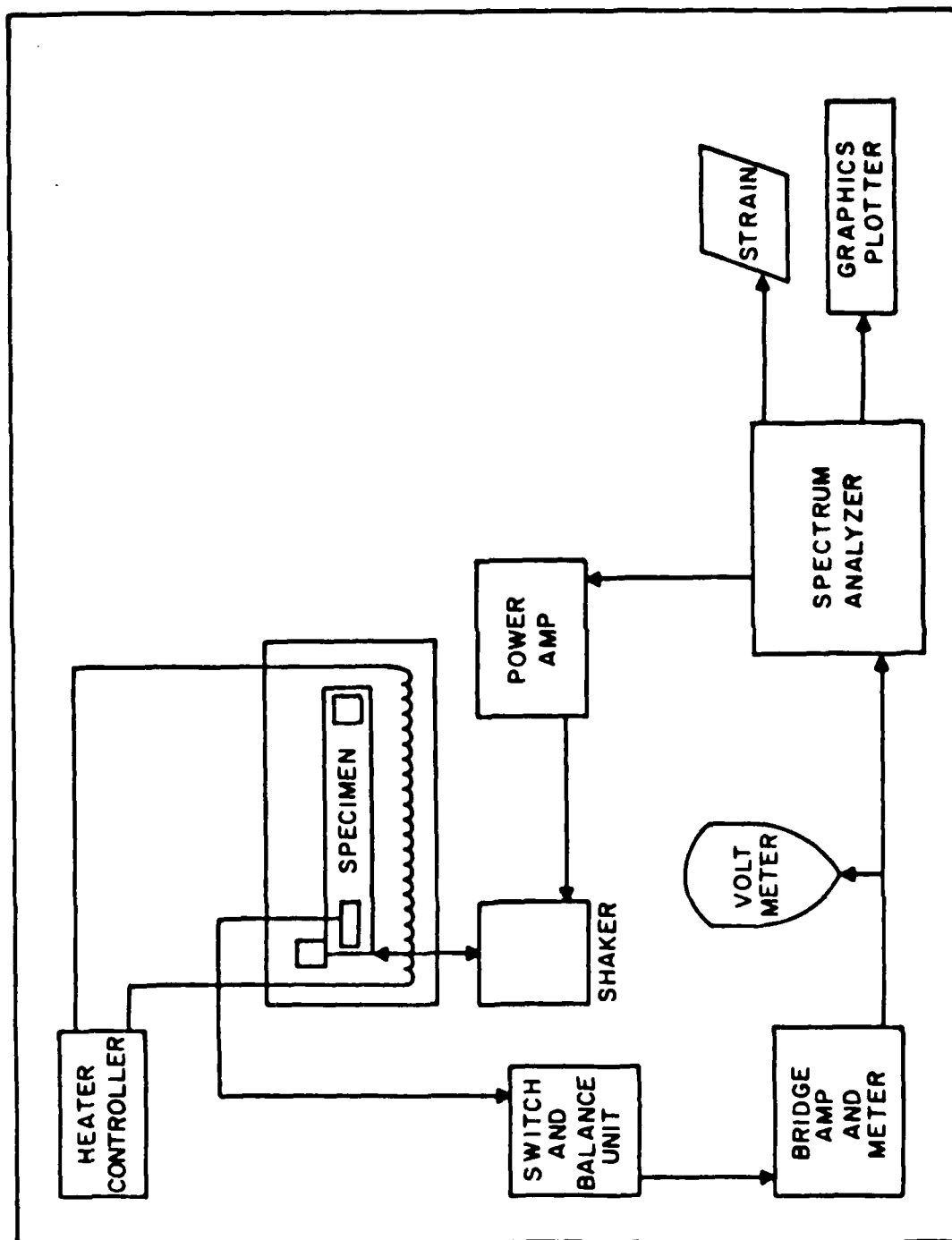


Figure 3.8 Block Diagram of Equipment Setup to Measure Strain

change is measured through a loop which originates in the Measurements Group, Inc. BAM-1 bridge amplifier and meter. This generates a D.C. excitation voltage via an internal battery and sends it through a Wheatstone bridge, which includes the resistance strain gage and an Ellis Associates Model BSG-6 switch and balance unit. The bridge is balanced by using the gain knob on the switch and balance unit to zero the reading on the digital voltmeter while there is no applied strain on the beam. The BAM-1 also serves to calibrate the strain gage system, in order to have a certain change in resistance (or voltage drop) equal to a strain value. Calibration was carried out as outlined in the BAM-1 Instruction Manual [Ref. 32]. The voltage output from the BAM-1 is input to the signal analyzer, which converts the voltage to a "dummy variable" in so-called engineering units (EU). The analyzer is programmed such that one EU equals one microstrain. The strain (EU) frequency response is displayed on the analyzer screen, and may also be printed on the attached plotter or stored on a micro floppy disk.

In order to study the temperature dependence of damping in the metals of interest, an elevated temperature control system was designed and constructed. The system was designed to be simple in nature and easy to use, to fit existing equipment with minimal modifications, and to provide a stable and easily controlled test temperature.



A thermally insulated test environment containment box was made to fit snugly down over the shaker assembly's foundation cross beam to enclose the cantilever beam and its clamp assembly (see Figure 3.9). The inner casing of the box was made from a thermally insulating phenaloc material. A one inch layer of ceramic fiber insulation was placed between the inner casing and the aluminum outer casing. Four glass tubes were mounted longitudinally in the inner casing to provide support for the wire of the heating element. Nickel-chromium heating element wire was woven around the tubes along the length of the box such that the cantilever beam and its clamp were enclosed from above and along both sides. Heat reflective aluminized-tape was placed along the top of the steel foundation cross beam. A 3/4 inch diameter hole was drilled through the lower-rear wall of the box, behind the clamp, in order to provide access for the heating element, thermocouples, strain gage wiring, and accelerometer cables. A second hole was drilled through the upper-rear wall of the box to provide access for the temperature controlling thermocouple. This thermocouple was of sufficient length to protrude along the length of the box to a location directly above the center of the beam's vibrating length. An Omega Engineering Model 49 proportioning controller was wired through a contactor coil and coupled to the heating element wire at a junction box on the outer rear casing of the containment box. The test



Figure 3.9 Photograph of Elevated Test Temperature Control System

environment containment box and the heater controller are shown schematically in Figures 3.6 and 3.8.

A maximum test temperature limit was established at approximately 115°C due to operating temperature limits on some of the system components. For example, the accelerometers and their cables have a maximum operating temperature of 125°C. Forced air cooling for the shaker was installed and aligned to prevent its overheating due to heat conduction. Elevated temperatures also necessitated the use of Aron Alpha high strength adhesive to mount accelerometers, whereas in the past, a soft wax was used for room temperature measurements. Additionally, a high temperature rated tape was used to secure all wiring along the beam and/or clamp, this so as to prevent it from contact with the heating element and to reduce vibration of the wiring, and thus reduce spurious noise in the system.

The elevated test temperature system had to be calibrated prior to use. Ultimately, intentions were to use a single thermocouple, mounted on the beam clamp face above the beam root, to define the beam test temperature. A beam was fitted with a thermocouple at the beam root and another at a distance of 3.5 inches from the root. These were compared against the clamp thermocouple. These three temperatures were plotted versus heating time at several controller set points (see Figures 3.10 and 3.11). These plots showed the existence of a beam-to-clamp thermal

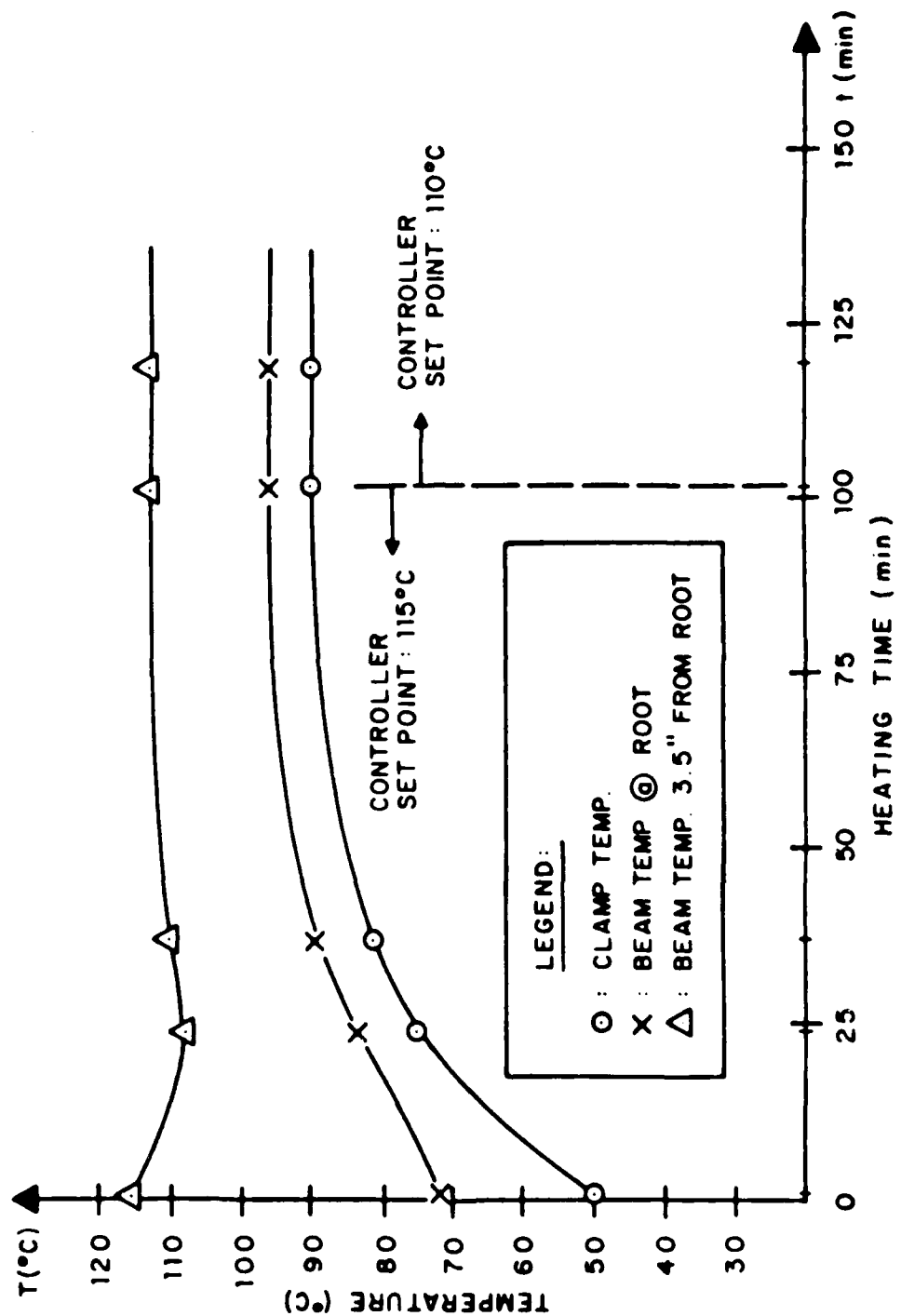


Figure 3.10 Test Temperature Settling Time at 110°C Set Point

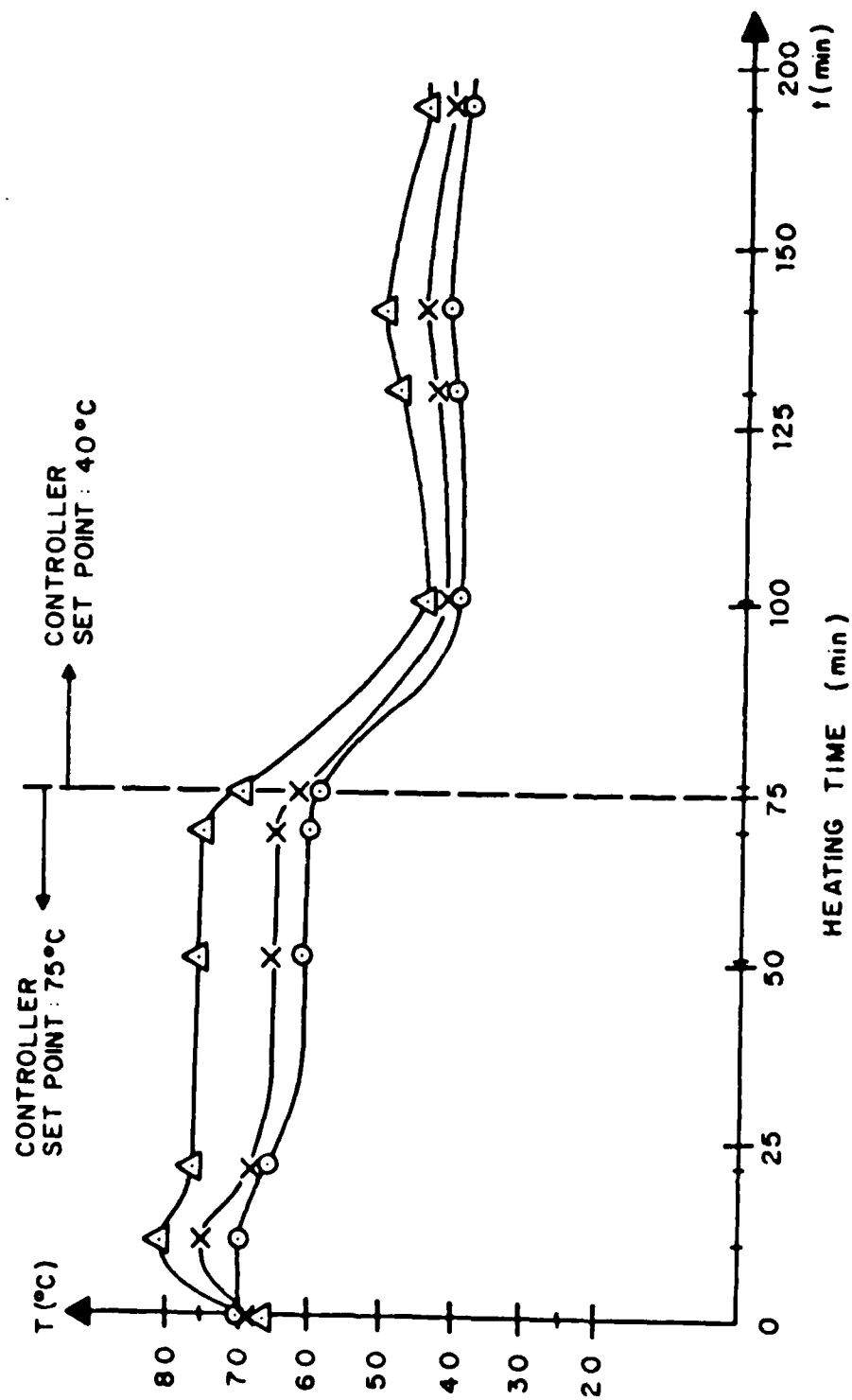


Figure 3.11 Test Temperature Settling Time at 75°C and 40°C Set Points

gradient, which varied in magnitude with controller set point. Additionally, the plots were used to determine the apparatus steady state temperature setting time at these controller settings.

Sheets of fibrous thermal insulation were inserted in the lower portion of the beam clamp assembly in order to minimize the heat conduction and thus decrease the thermal gradient. A precise characterization of beam temperature gradient was then performed at controller settings of 110°C, 70°C, and 40°C. Five thermocouples were mounted along a beam, and the system was heated for the previously established settling time at a given set point. Temperatures were recorded at points along the beam and at the clamp. Clamp temperature was subtracted from the temperature at each location along the beam, and the results, plotted in Figure 3.12, showed a temperature gradient along the beam for a given heater controller set point. Thereafter the single thermocouple on the clamp face was used to define the beam test temperature.

The heart of spectral analysis equipment is the signal analyzer (Figure 3.13). Eleven different setup pages are used to program the analyzer for operation. The optimum setups were determined and programmed for both the transfer function and strain measurements. These programs were stored on micro floppy disk and in the analyzer's internal memory. The analyzer was programmed to average 150

## BEAM TEMPERATURE CHARACTERIZATION

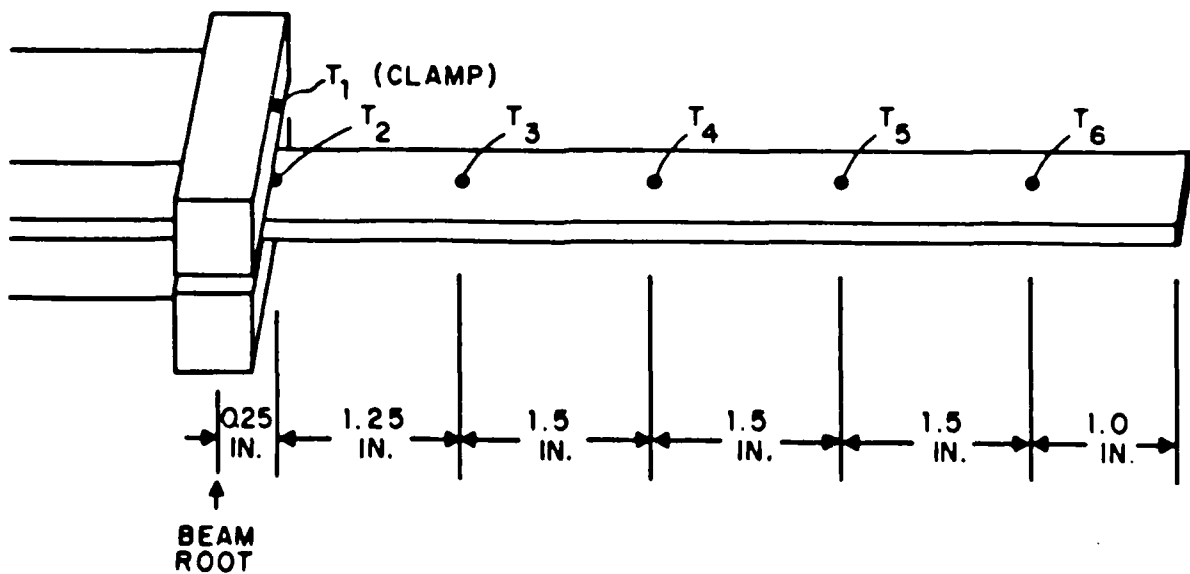
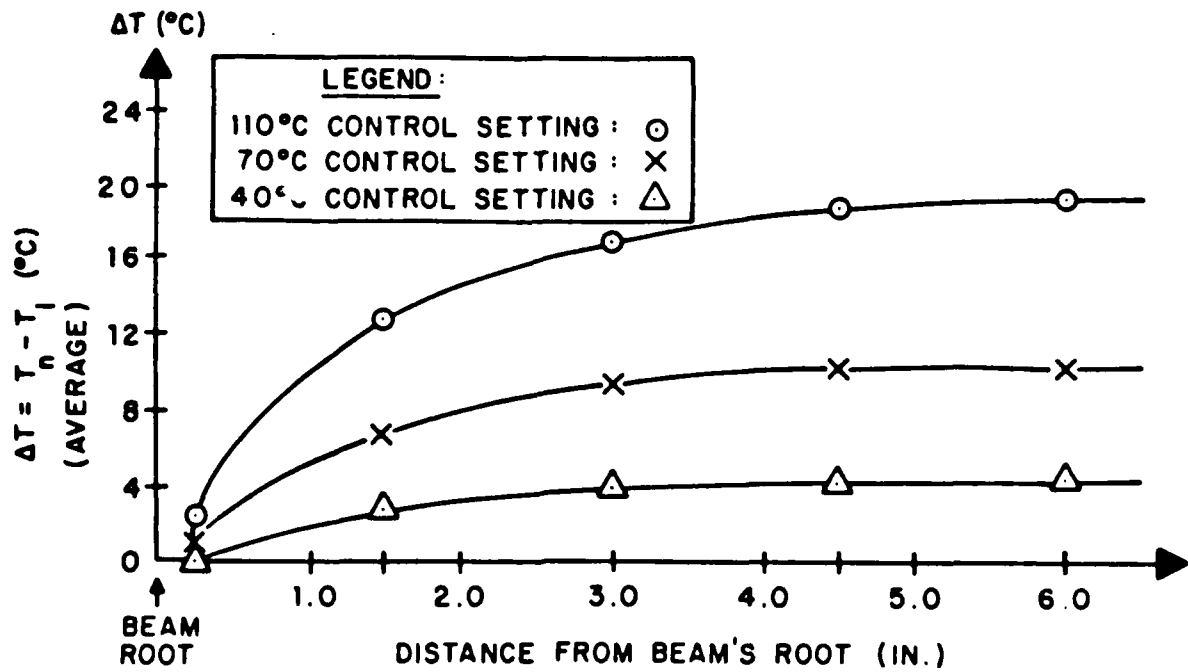


Figure 3.12 Beam Temperature Characterization

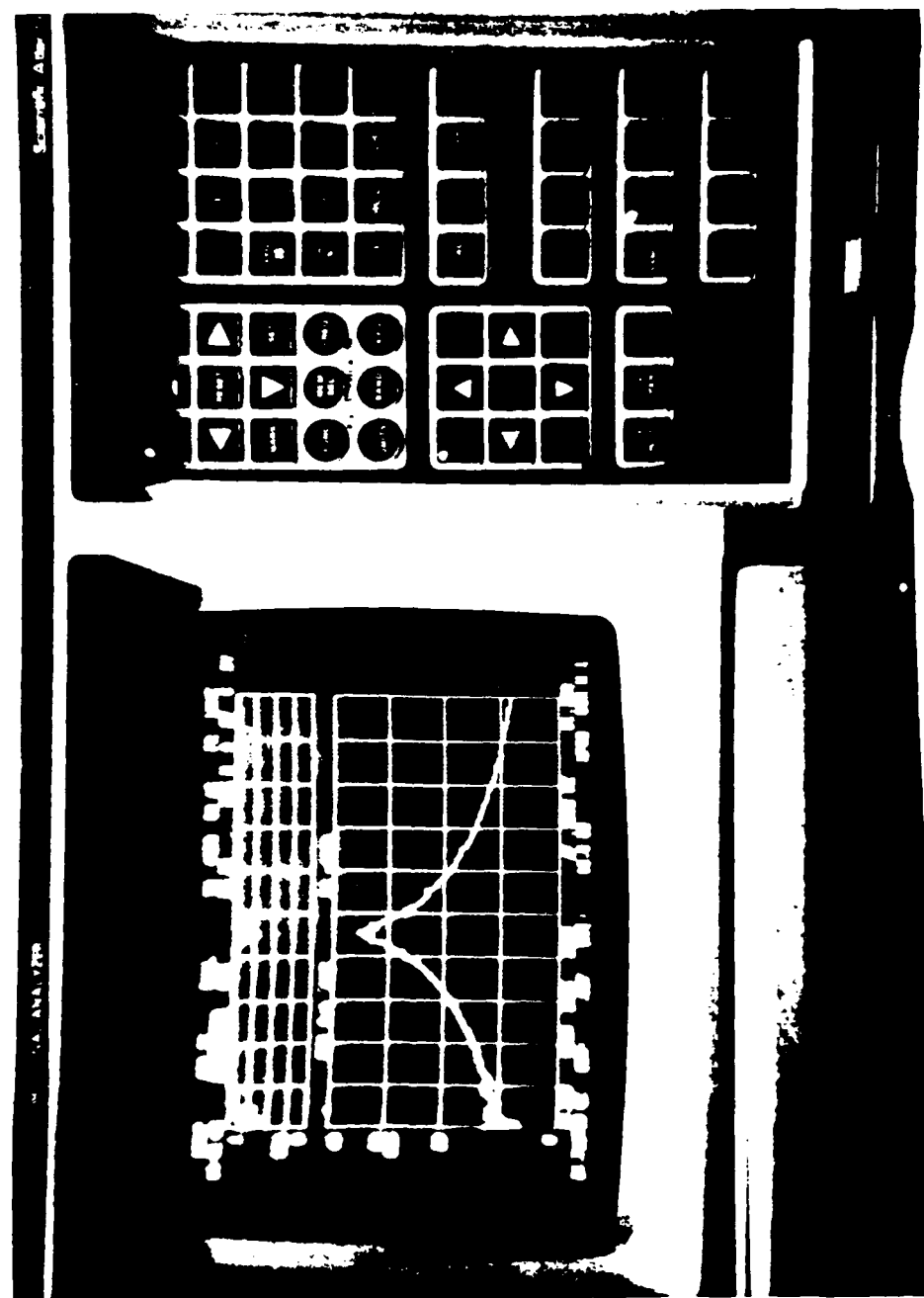


Figure 3.13 Photograph of Signal Analyzer



different data samples to establish the various output displays utilized in this study. All output displays were stored on micro disk.

Specific damping capacity (SDC) was calculated using equation (1.13) with the data taken from the transfer function frequency response curves. The first three modal frequencies were estimated using a low resolution, base band transfer function (T/F) plot, as shown in Figure 3.14. For improved accuracy, the analyzer was then programmed to focus in on a narrow bandwidth centered near the estimated modal frequency. Thus a high resolution, narrow band T/F plot was generated (Figure 3.15). By doing this, the frequency resolution was improved by a factor of 16. This provided more data in the vicinity of the modal resonant frequency ( $\omega_n$ ), allowing it to be more accurately defined. Three different displays of this data were used to determine the best choice of  $\omega_n$ . For example, the frequency at the maximum point on the T/F and coherence (COH) plot, was compared to the frequency at which the phase shift ( $\phi$ ) was nearest to  $\pm 90^\circ$  on the T/F and  $\phi$  plot (Figure 3.16), and to the frequency at which the real (RE) magnitude was closest to zero on the real and imaginary (IM) T/F plot (Figure 3.17). Then the DB magnitude at  $\omega_n$  was recorded, and at a magnitude of 3DB down from there  $\omega_2$  and  $\omega_1$  were picked off the T/F plot.

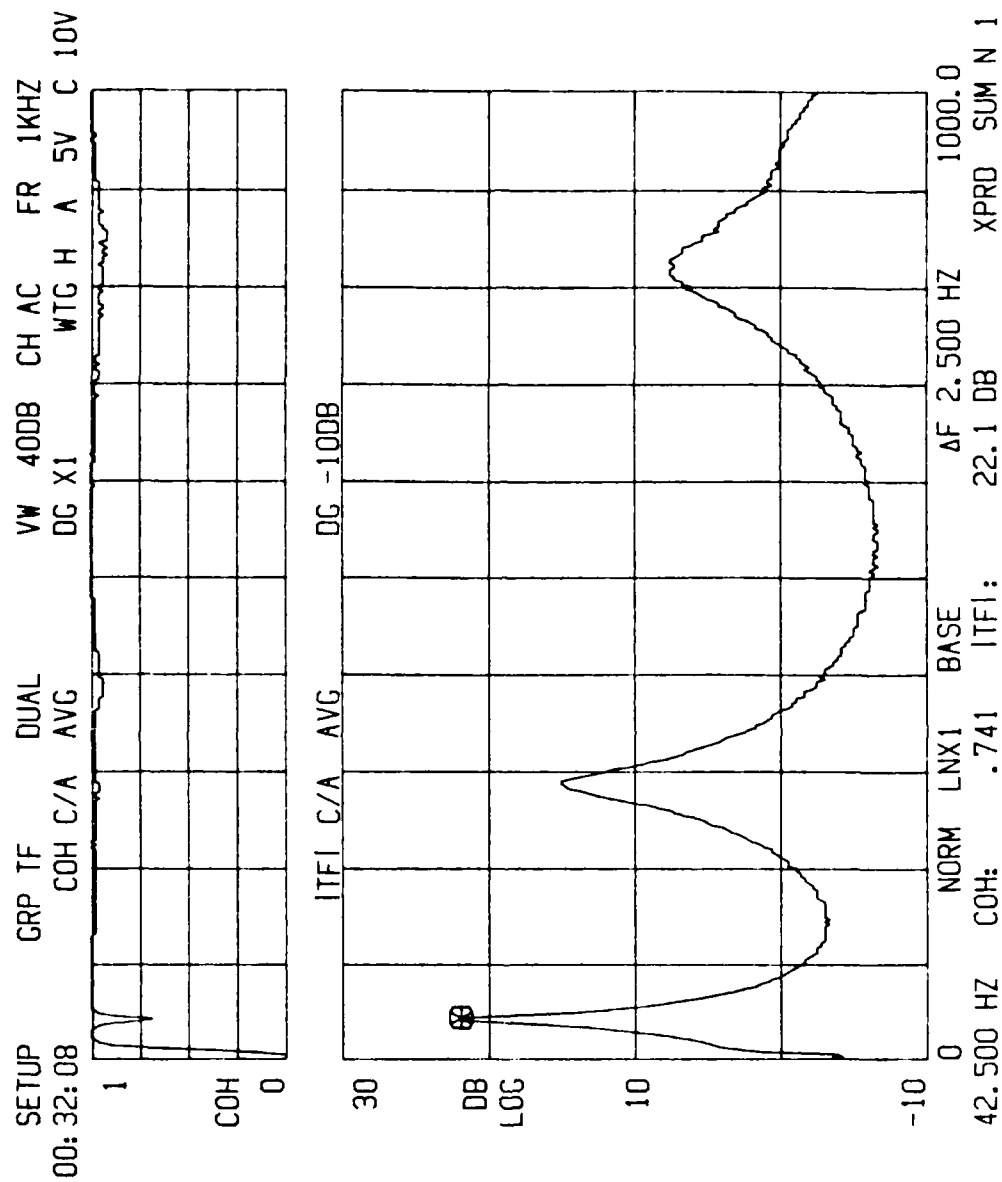


Figure 3.14 Broad Band Transfer Function and Coherence

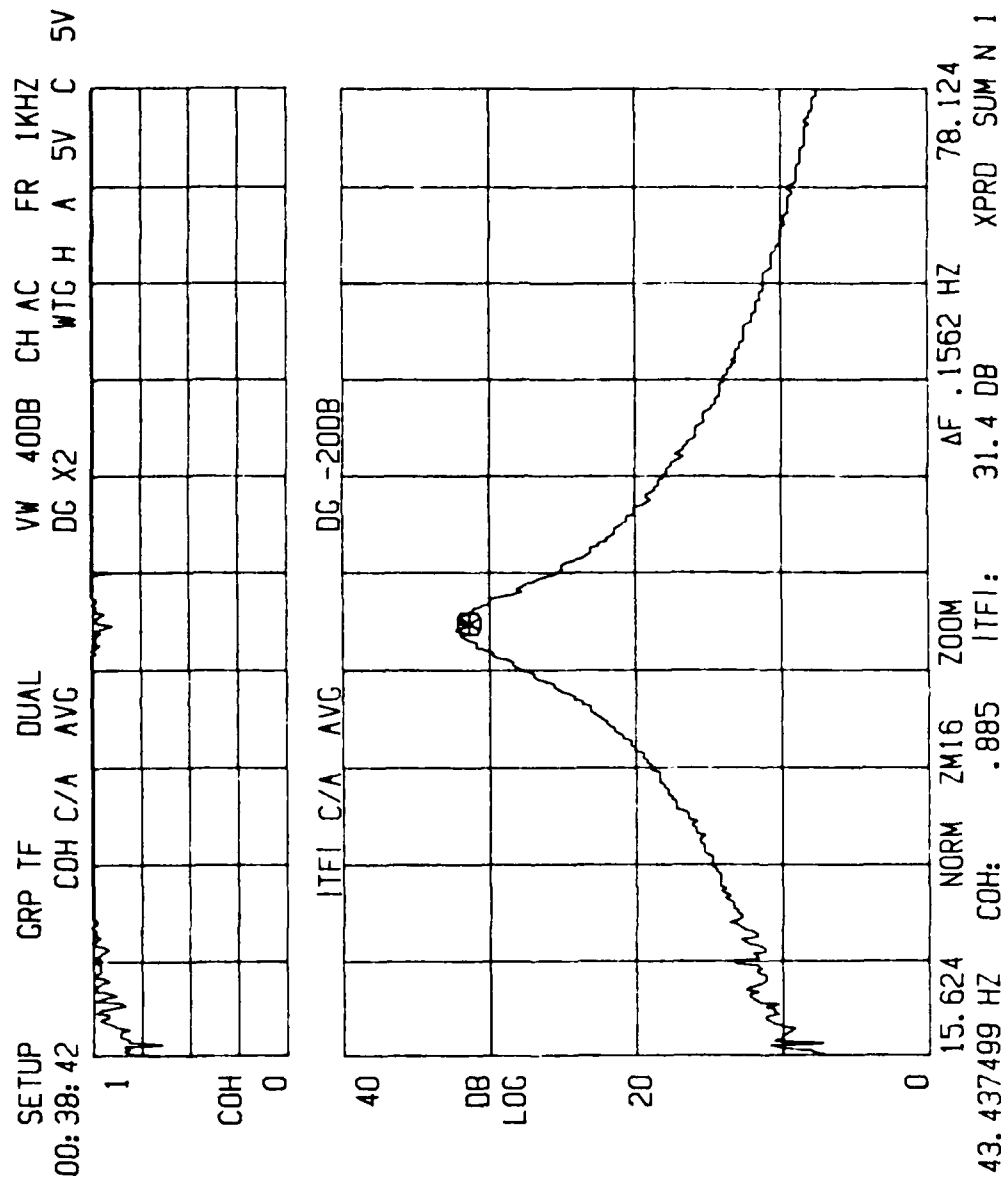


Figure 3.15 Narrow Band Transfer Function and Coherence

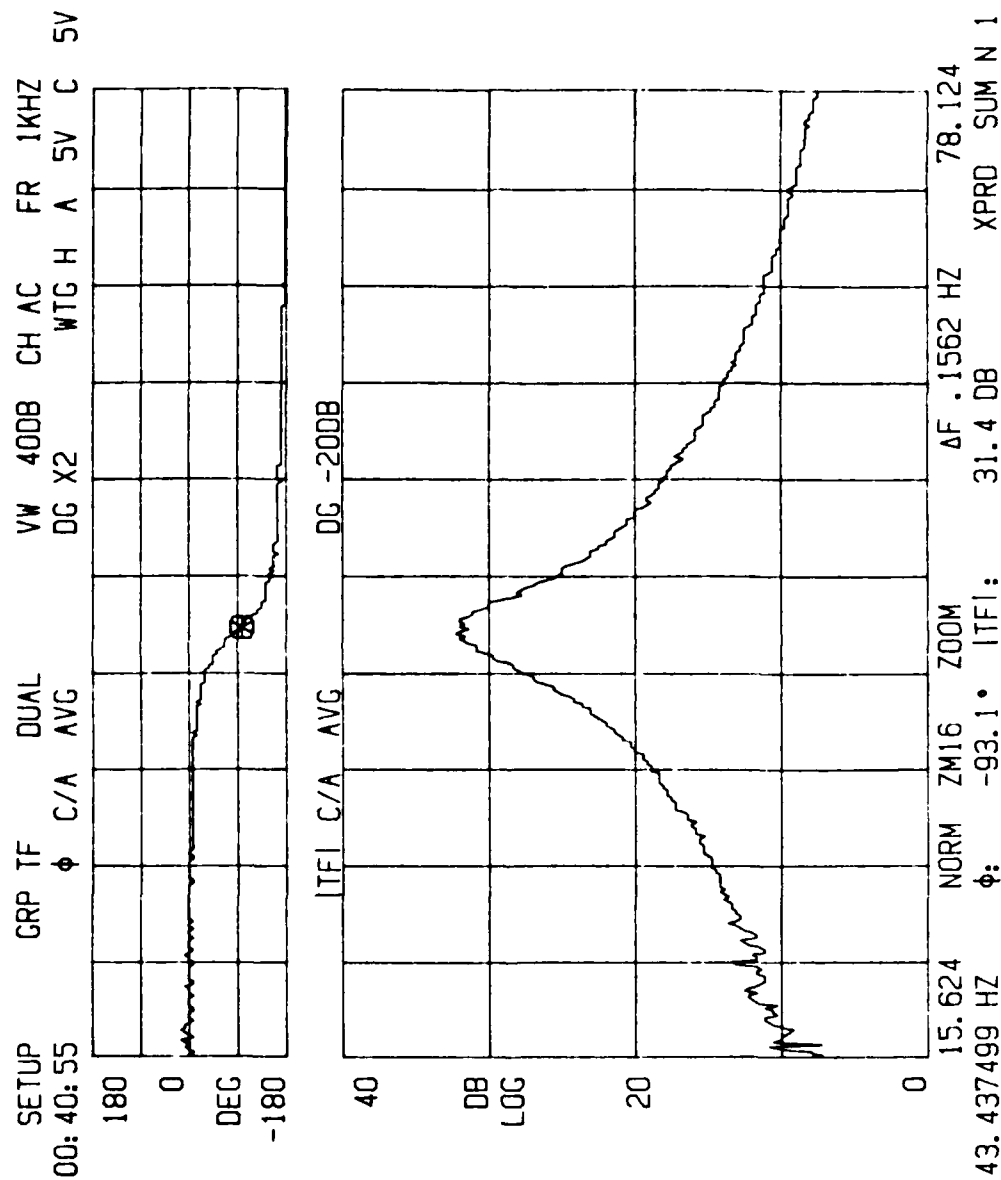


Figure 3.16 Narrow Band Transfer Function and Phase

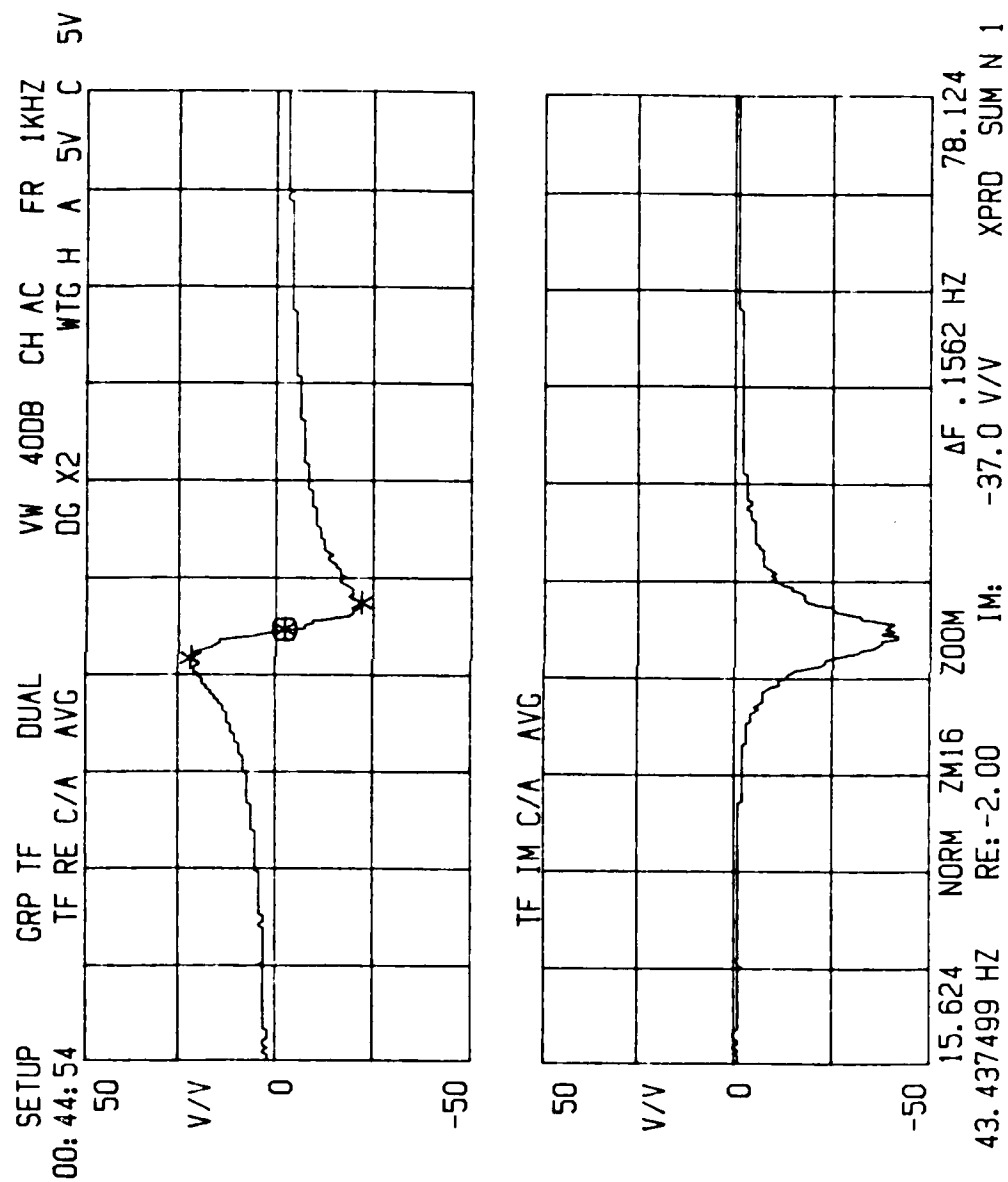


Figure 3.17 Narrow Band Transfer Function Real and Imaginary

A parameter known as coherence (COH) is plotted in the upper portion of Figures 3.14 and 3.15. Coherence is an indication of the purity of the system's transfer function. It indicates how much of the system output is caused by the system input. Structural nonlinearities and/or mechanical noise contamination will reduce system T/F coherence. COH magnitude varies from zero to one. Comparison of the COH magnitude at  $\omega_n$  in Figures 3.14 and 3.15 shows that coherence improved as frequency resolution was increased.

Strain magnitudes at resonance were read directly from a data display generated by the signal analyzer. As described earlier, the signal analyzer was programmed to display strain values as a dummy variable in so-called EU (engineering units, 1 Eu = 1 microstrain). The general frequency dependence of strain magnitude was displayed in low resolution, baseband plots such as Figure 3.18. These showed that the beams experienced maximum strains when vibrated at the modal resonant frequencies. Additionally, the strain magnitudes were largest for mode 1 deformation and smallest for mode 3 deformation. Accurate strain amplitudes were obtained from high resolution, narrow bandwidth plots such as Figure 3.19.

#### D. DAMPING MEASUREMENT REPRODUCIBILITY

Accuracy of measurement and reproducibility of results must be of central concern in any research program. An extensive effort was made in the present work to optimize

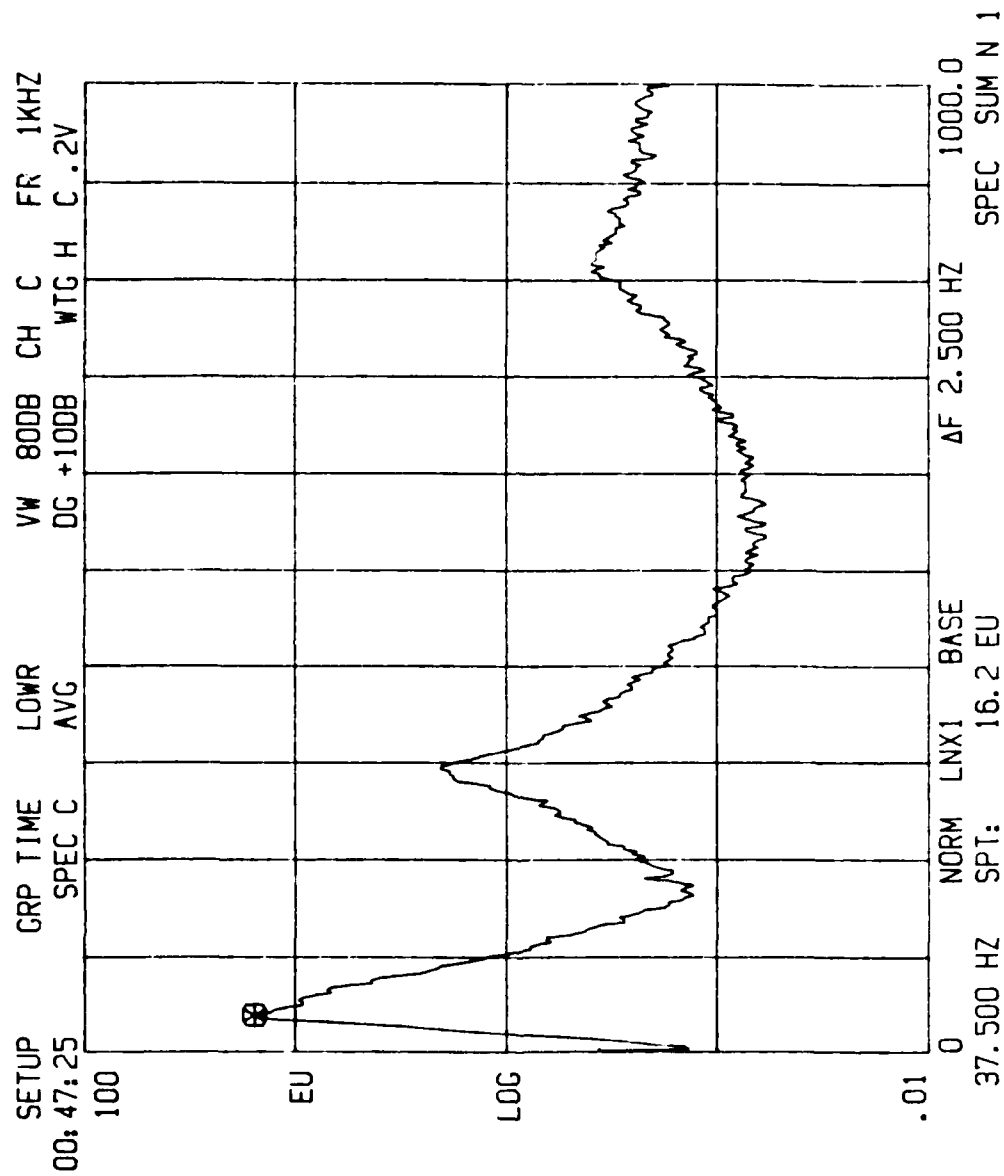


Figure 3.18 Broad Band Strain (EU) Distribution

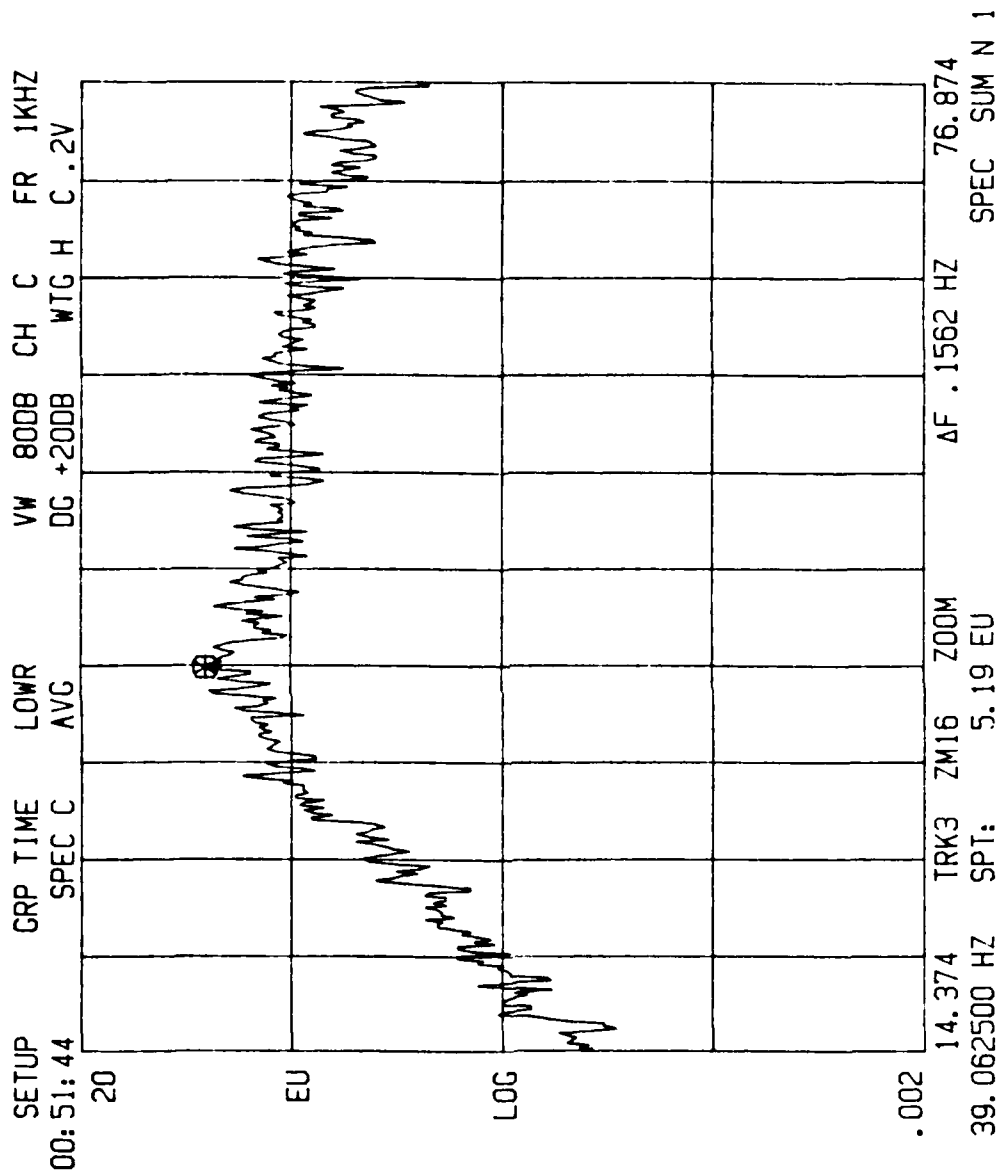


Figure 3.19 Narrow Band Strain (EU) Distribution



the procedures and the capabilities of all equipment utilized in the modified resonant dwell damping measurement technique. Procedures and equipment setups were optimized through consultation with faculty, factory technical representatives, previous thesis students, and the laboratory technical staff, and thorough study of equipment operating manuals, scientific literature, and previous theses.

The damping measurement system setup was detailed in the previous section. However some of the particulars in the programming of the signal analyzer merit attention, since they directly affect the reproducibility of results. For example the average target count ( $N$ ) was set at 150. This means that 150 ensembles of data were averaged to establish each display. This was found to give verifiable results without requiring an exceedingly lengthy run time.

Fast Fourier Transform (FFT) is performed by the analyzer on the input signals to produce frequency spectrum data. When random excitation (i.e., broadband noise) is used to generate inputs that are analyzed by FFT, a phenomenon called leakage results. The FFT uses frequency windows to collect response data. But since the excitation is not periodic, not all of the response signal can be captured within its associated excitation signal's frequency window. The result is a distortion of data along the frequency spectrum. The most popular technique to minimize

these leakage effects is to artificially force the signal to zero at the beginning and end of each data collection window. This is done by multiplying the actual data record by a mathematical curve, known as a weighting function, before processing by the FFT. The weighting function known as the Hanning window is the one most often used for random noise excitation. [Ref. 33:p. 28]

The signal analyzer employed had one limitation which was not accounted for in its setup programming software. Scientific Atlanta could not guarantee a 5.0 volt output level on its signal analyzer-generated broadband noise signal. When set to produce a 5 volt signal, it fluctuates between 2.0 and 5.0 volts. However, the software in the signal analyzer allows selection of the 5.0 volt broadband noise signal. Inadvertent selection of this stronger signal would produce higher strain rates, but the amplitudes would fluctuate with the signal voltage. Thus the constant change in excitation signal strength would prohibit the reproduction of results.

The major programmable factor affecting the accuracy of data for damping calculation is frequency resolution. It influences the frequency readings and the T/F DB magnitudes. Resolution is defined by:

$$\Delta F = \frac{F.P.}{N_L} \left( \frac{1}{Z.M.} \right) \quad (3.2)$$

where:

F.R. = broad band frequency range

$N_L$  = number of resolution lines

Z.M. = zoom multiplier.

$\Delta F$  is the frequency spread between consecutive data points. It can be seen in Equation (3.2) that the programmed settings F.R.,  $N_L$ , and Z.M. have an important role in determining data accuracy. The first three modal frequencies of all cantilever beam specimens studied fell within either the 1 kHz or 2 kHz band.  $N_L$  was set at 400 for all measurements in this study. This meant that 400 frequency data points were used in each FFT. A Scientific Atlanta applications expert informed this researcher that to program for the ZOOM analysis band with  $N_L = 800$  was an illegal setup, which would generate false displays. Therefore for maximum resolution over all analysis bands and for ease of programming,  $N_L$  was kept constant. Permutations of selectable values for Equation (3.2) setup factors proved that a  $\Delta F$  equal to 0.1562 Hz provided plenty of frequency resolution. Therefore, F.R. and Z.M. were manipulated to maintain  $\Delta F = 0.1462$  Hz whenever any data were being extracted from displayed information. In this manner, reproducible results were obtained in a reasonably short data processing time.

Another potential problem in data reproducibility lies in the selection of the modal resonant frequency ( $\omega_n$ ), which is the basis for the half-power method of damping measurement. As described in the previous section,  $\omega_n$  was chosen at the frequency which optimized the facts that:

- a. T/F magnitude should peak (see Figure 3.15)
- b. phase shift should be  $\pm 90$  degrees (see Figure 3.16)
- c. real magnitude should equal zero (see Figure 3.17).

Therefore an alternate damping calculation method, the vector technique, was used to verify SDC results from the half-power method. In this method, noted for being quite accurate, SDC is defined as:

$$\text{SDC (\%)} = 200 \pi \left[ \frac{(f_2/f_1)^2 - 1}{(f_2/f_1)^2 + 1} \right], \quad f_2 > f_1 \quad (3.3)$$

where  $f_2$  and  $f_1$  are the frequencies at the maximum and minimum peaks in the T/F REAL plot (see Figure 3.17). [Ref. 34:pp. 44-45] Comparison of the data in Figure 3.20 (SDC via half-power method) with that in Figure 3.21 (SDC via vector technique) shows that the half power method SDC results are accurate.

Some other measures were taken to ensure that the data generated and subsequent results were meaningful. Lock-nuts were added to the "stinger" rod which transmits the excitation force from the shakes to the beam assembly (see Figures 3.7 and 3.9). These prevented the threaded

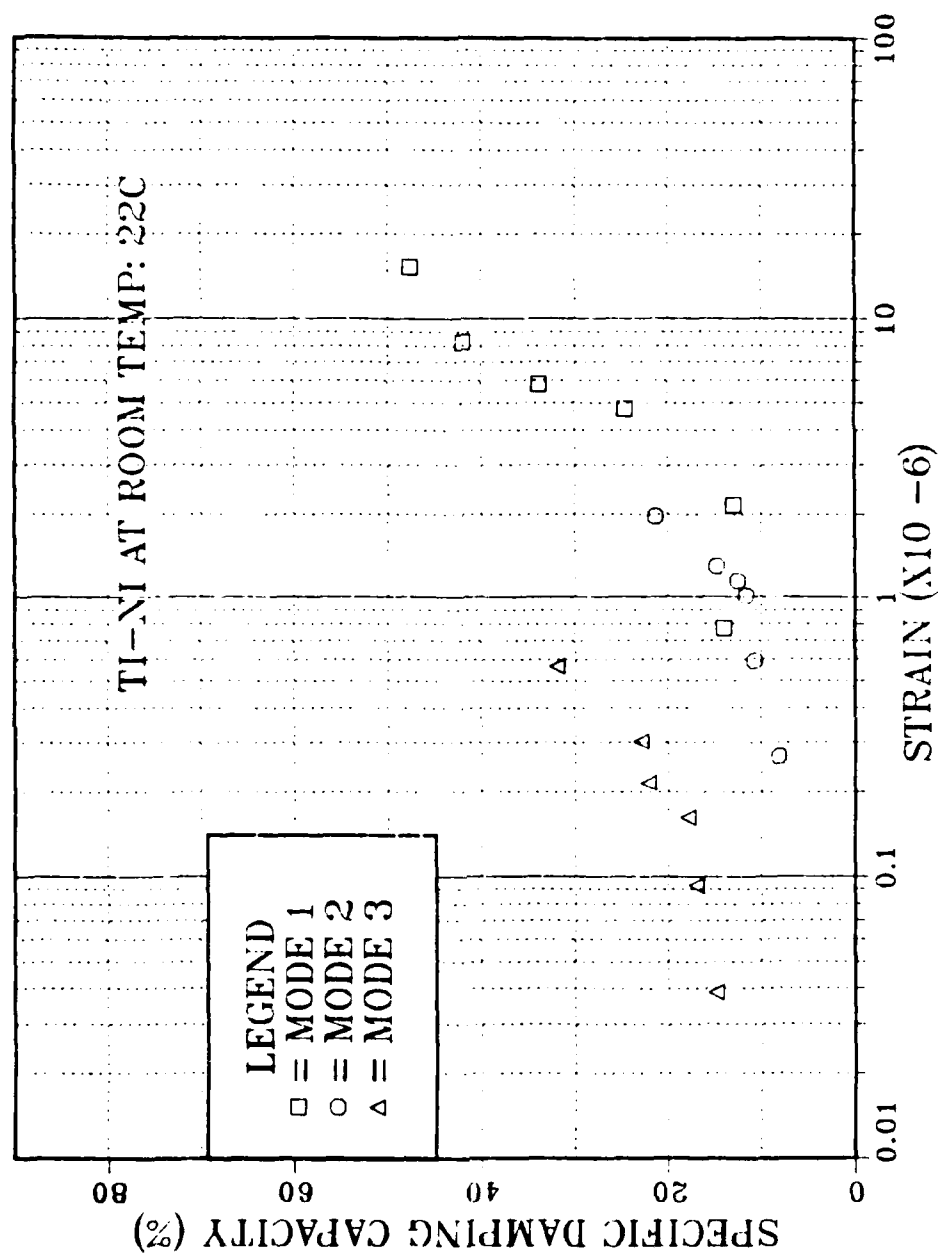
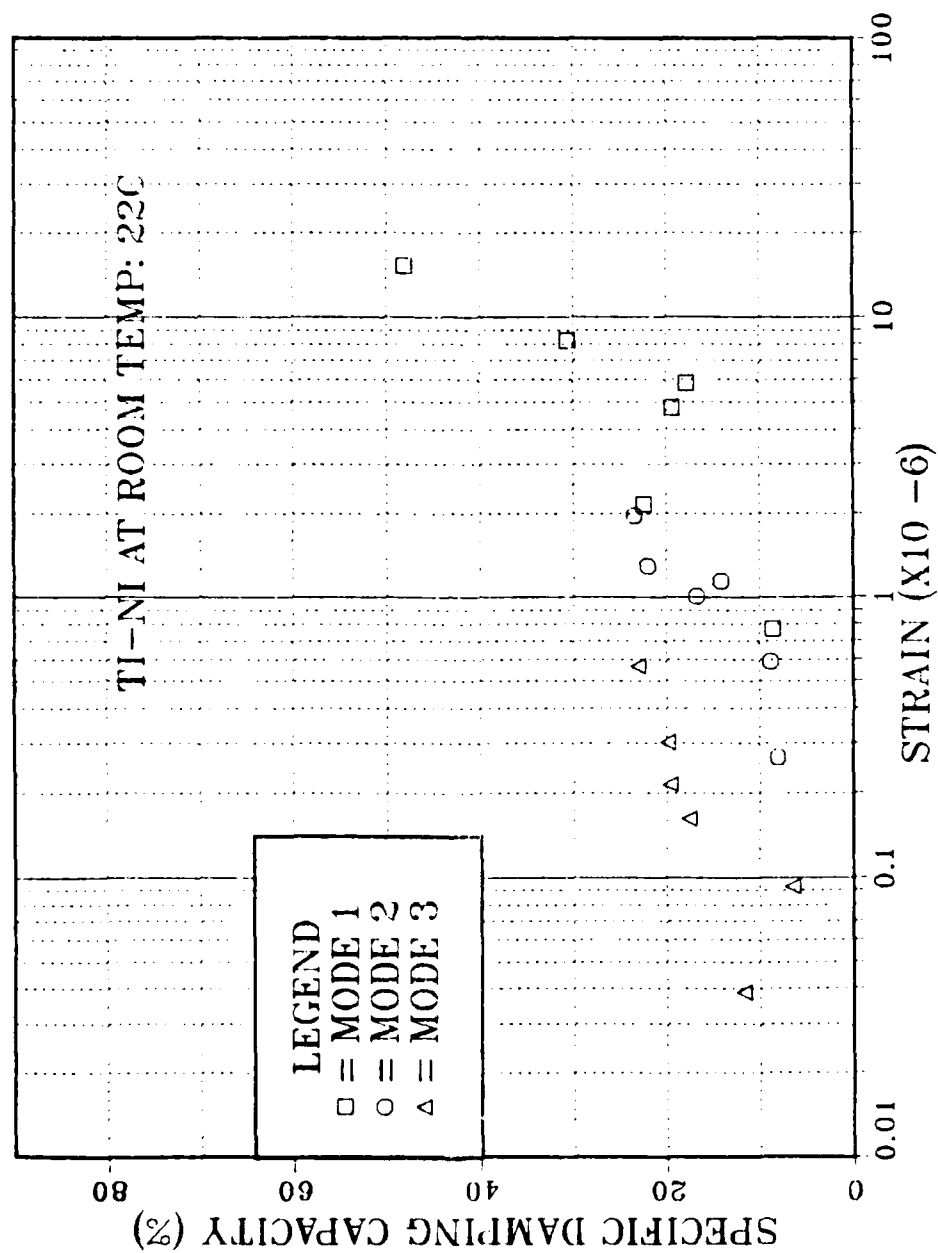


Figure 3.20 SDC Data Via Half-Power Method



connection points from vibrating loose and adding noise to the system. Additionally, all system wiring in the vicinity of the beam and the system response transducers were taped down in an effort to prevent spurious noise generation. Also, the electronically generated noise levels were observed by running the system with the amplifier gain set at zero. This was used to verify that measured system output levels were well above electronic noise levels.

Finally a comprehensive system tightness or clarity check was performed. This was accomplished by using a dual-channel oscilloscope to compare a signal analyzer generated sine wave to the resultant system response signal being sent back to the analyzer from the accelerometers (see Figure 3.6). If the system was "tight," the simultaneous display showed two clean sine waves. This procedure was carried out each time any changes were made to the mechanical system.

#### IV. RESULTS AND DISCUSSION

##### A. SHAPE MEMORY ALLOYS

###### 1. Ti-Ni

The differential scanning calorimetry (DSC) results for Ti-Ni are depicted in Figure 4.1. It was used to define the start and finish temperatures of the martensitic and austenitic phase changes listed in Table III.

TABLE III  
TI-NI PHASE TRANSFORMATION TEMPERATURES

<u>Transformation Point</u>	<u>Temperature (°C)</u>
A <sub>S</sub>	44
A <sub>F</sub>	81
M <sub>S</sub>	66
M <sub>F</sub>	28

Specific damping capacity (SDC) of this alloy was first measured at room temperature (22°C). The results (Figure 4.2) indicate that damping mechanisms were activated at a cyclic strain amplitude of approximately one microstrain. Once damping was activated it continued to increase out to a value of 47.6% at the highest strain measured ( $15.3 \times 10^{-6}$ ). Since the test temperature was



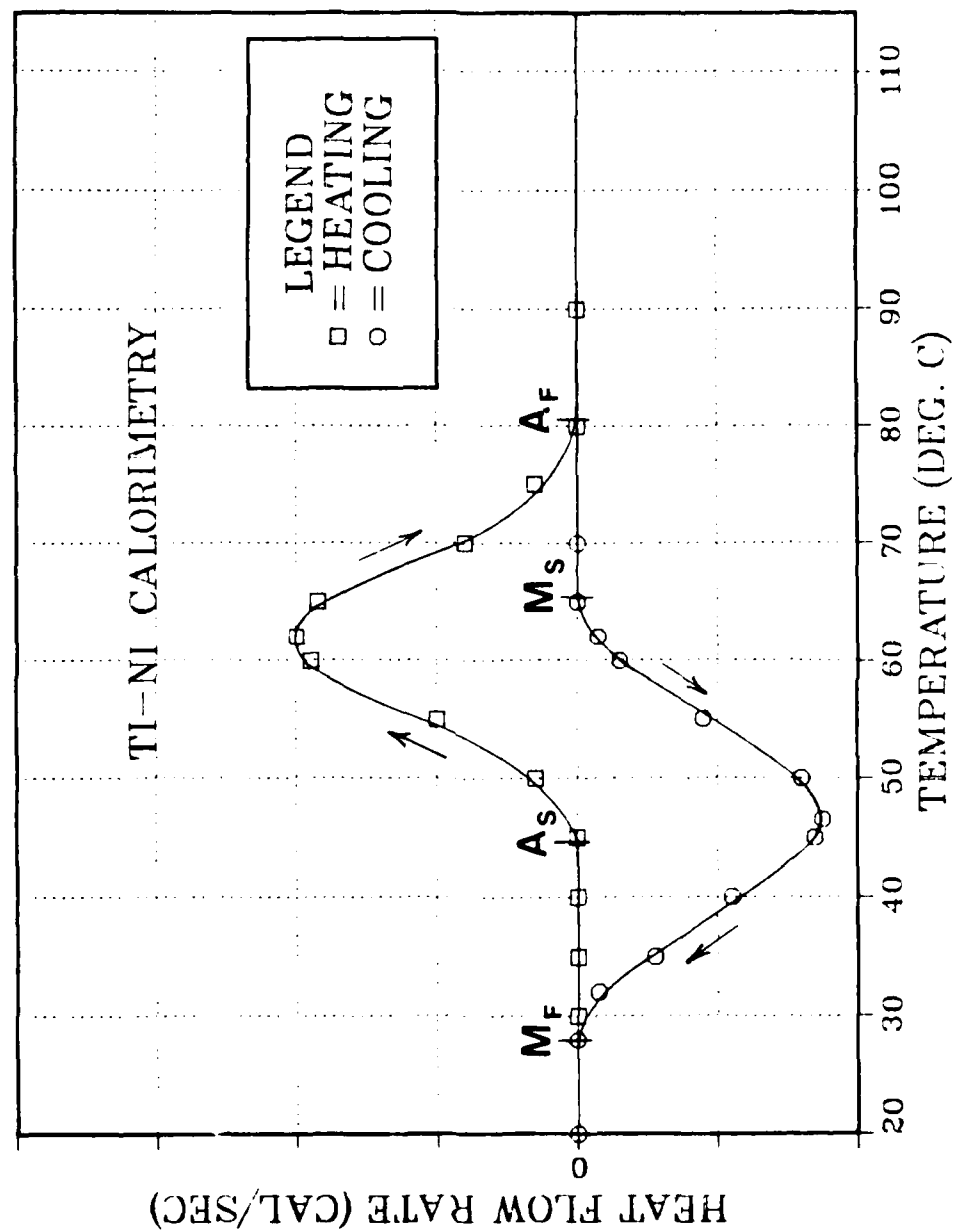


Figure 4.1 Ti-Ni Calorimetry

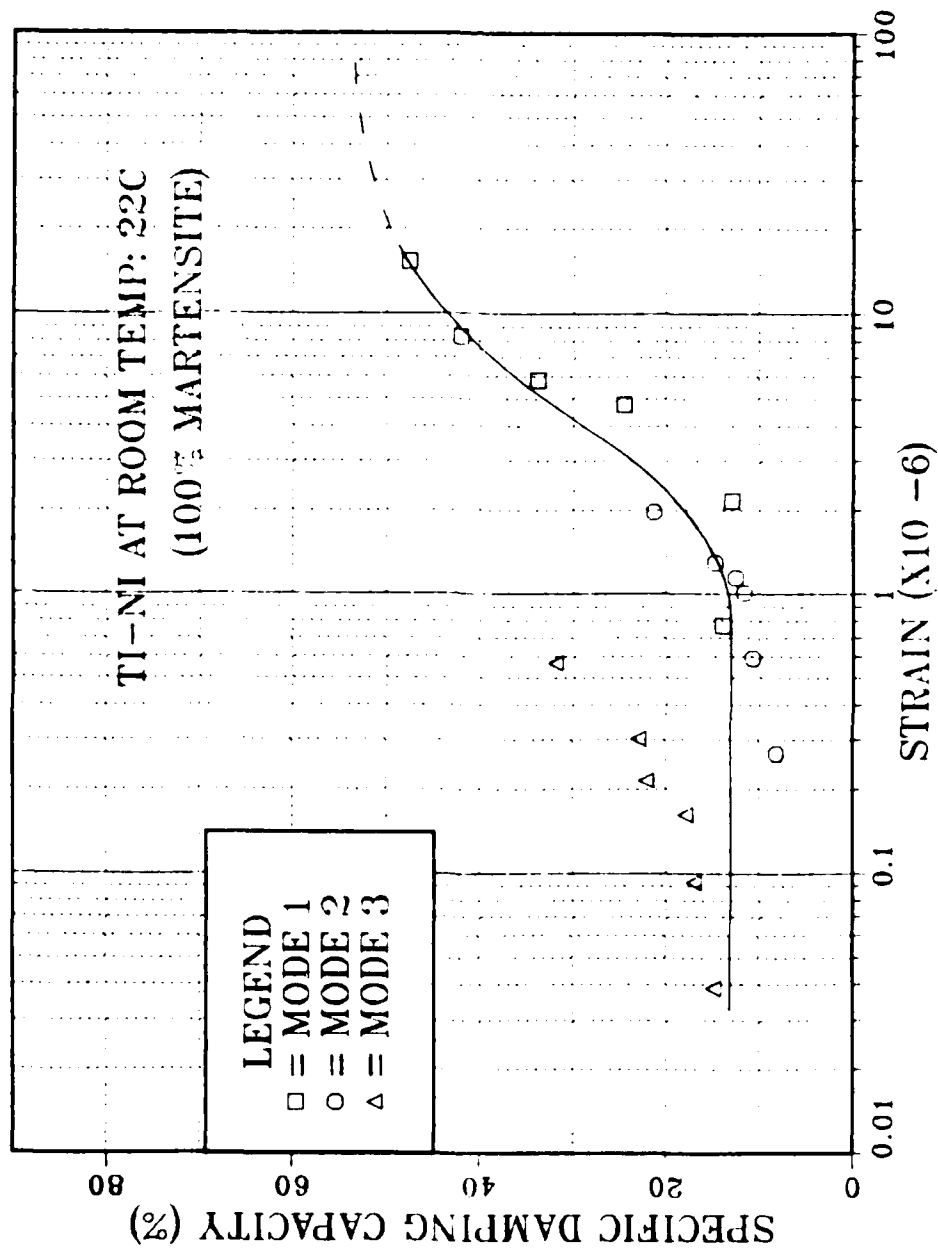


Figure 4.2 Cyclic Strain Dependence of SDC in 100% Martensitic Ti-Ni

below martensite transformation finish temperature (see Table III), the energy dissipation mechanism probably originated from hysteresis due to lattice friction upon inter-variant boundary motion. If this is the case, it would be expected that SDC would continuously increase to a maximum as cyclic strain is increased, after which it might decrease with larger strains. Unfortunately, the system utilized in this study could not generate sufficient strain amplitudes to confirm this behavior.

It is noted that on the SDC versus strain plots the data is discontinuous from mode to mode. But generally the SDC in overlapping regions is not more than about 10%. Therefore, it is assumed throughout this study that the strain-dependent SDC data is continuous between modes.

The specimen was then heated to a temperature that ranged from 57°C to 64°C (the temperature variance is due to the thermal conduction-induced temperature gradient along the beam, see Figure 3.12). This test temperature is approximately half way through the temperature range for the transformation from martensite to austenite (see Table III). The cyclic strain dependence of SDC for this alloy condition is shown in Figure 4.3. A major portion of the material's SDC was lost, no doubt because the damping-critical martensitic microstructure of this shape memory alloy was vanishing. It is possible that some martensitic transformation was being induced at the largest strain

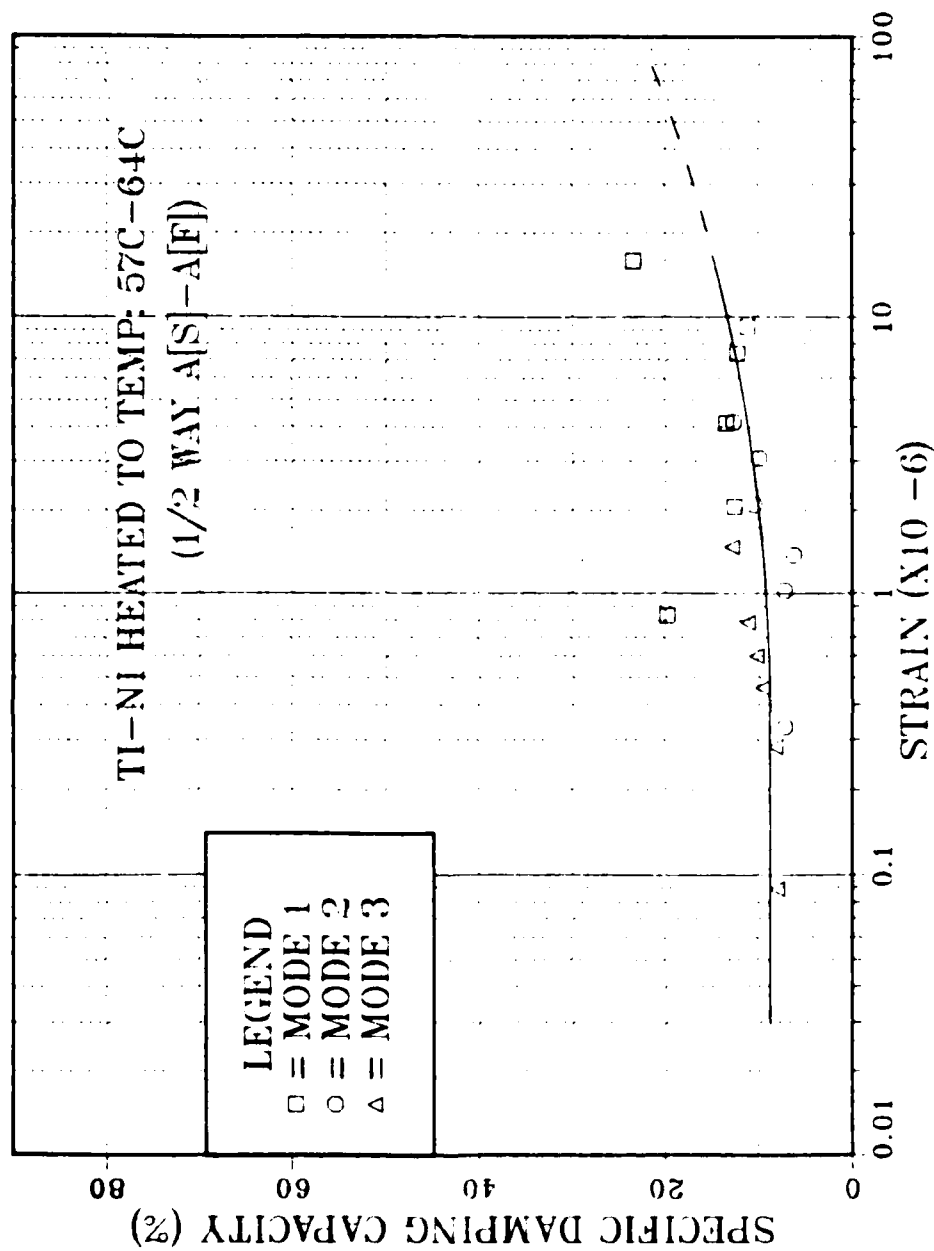


Figure 4.3 Strain Dependence of SDC for Ti-Ni Heated to 57°C-64°C

amplitudes, and that this elevates the damping to some extent in this strain range (see Figure 4.3).

The temperature was then elevated to a range of 93°C to 109°C along the beam. This test temperature established the alloy's microstructure as fully austenitic. The cyclic strain dependence of SDC for this alloy condition is depicted in Figure 4.4. It is clear that in the austenitic microstructural state, the alloy had quite low damping capability, and no strain-dependence of damping.

Subsequently, the same Ti-Ni beam was cooled to a temperature of 40°C to 46°C, or approximately two-thirds of the way through the temperature range of the austenite-to-martensite phase transformation (see Table III). The cyclic strain dependence of SDC for this alloy condition is displayed in Figure 4.5. It is obvious that the initiation of the martensitic phase transformation has generated some martensite plates, and that an increasing degree of lattice friction is generated as more and more inter-variant boundaries are mobilized by the cyclic strain. In this manner, the damping capacity increases with cyclic strain amplitude, but not as strongly as when in the fully martensitic condition. A summary of this damping behavior in Ti-Ni as a function of cyclic strain and test temperature is shown in Figure 4.6.

It was decided to attempt a direct evaluation of the sensitivity of SDC to temperature change, by carrying out

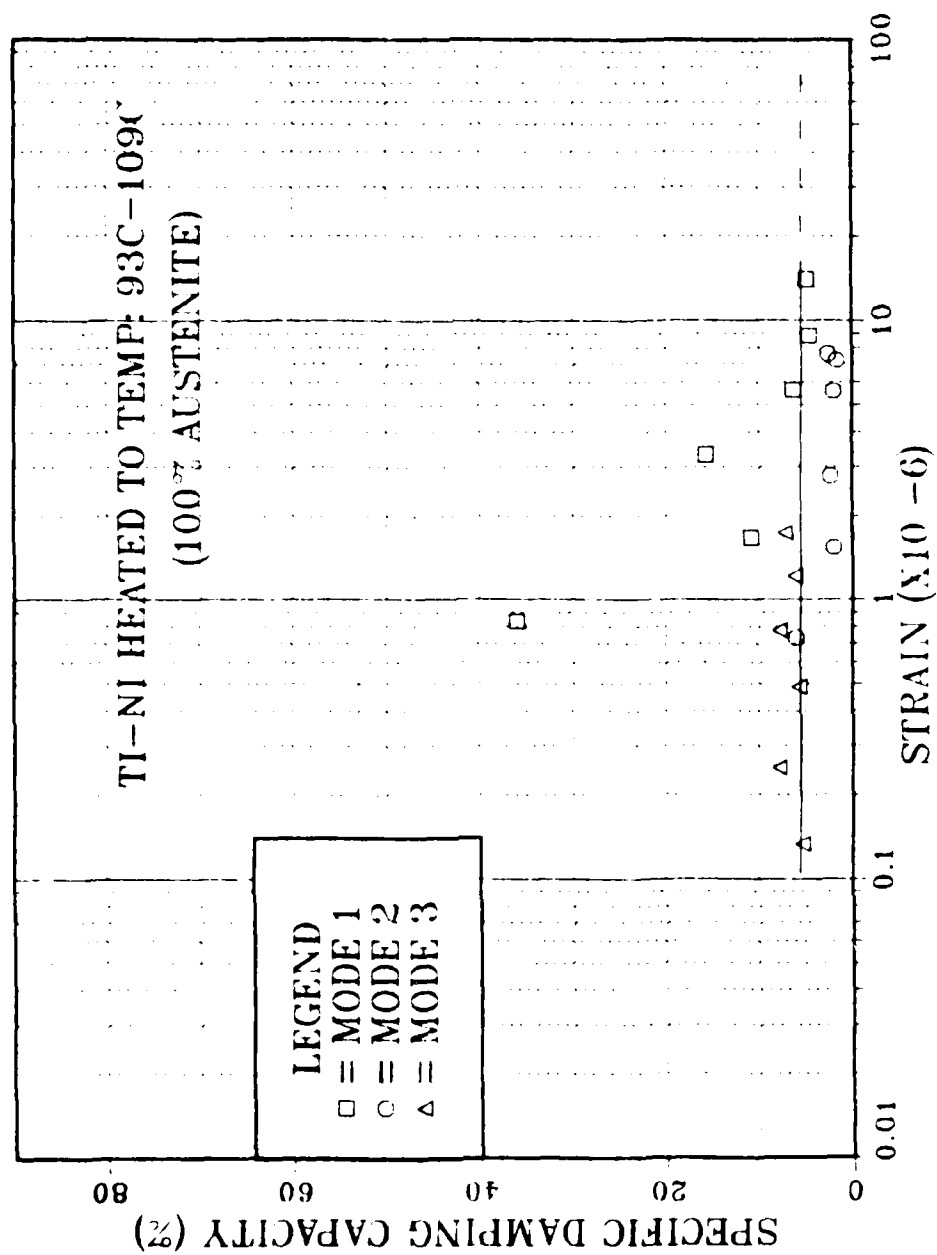


Figure 4.4 Strain Dependence of SDC for Ti-Ni Heated to 93°C-109°C

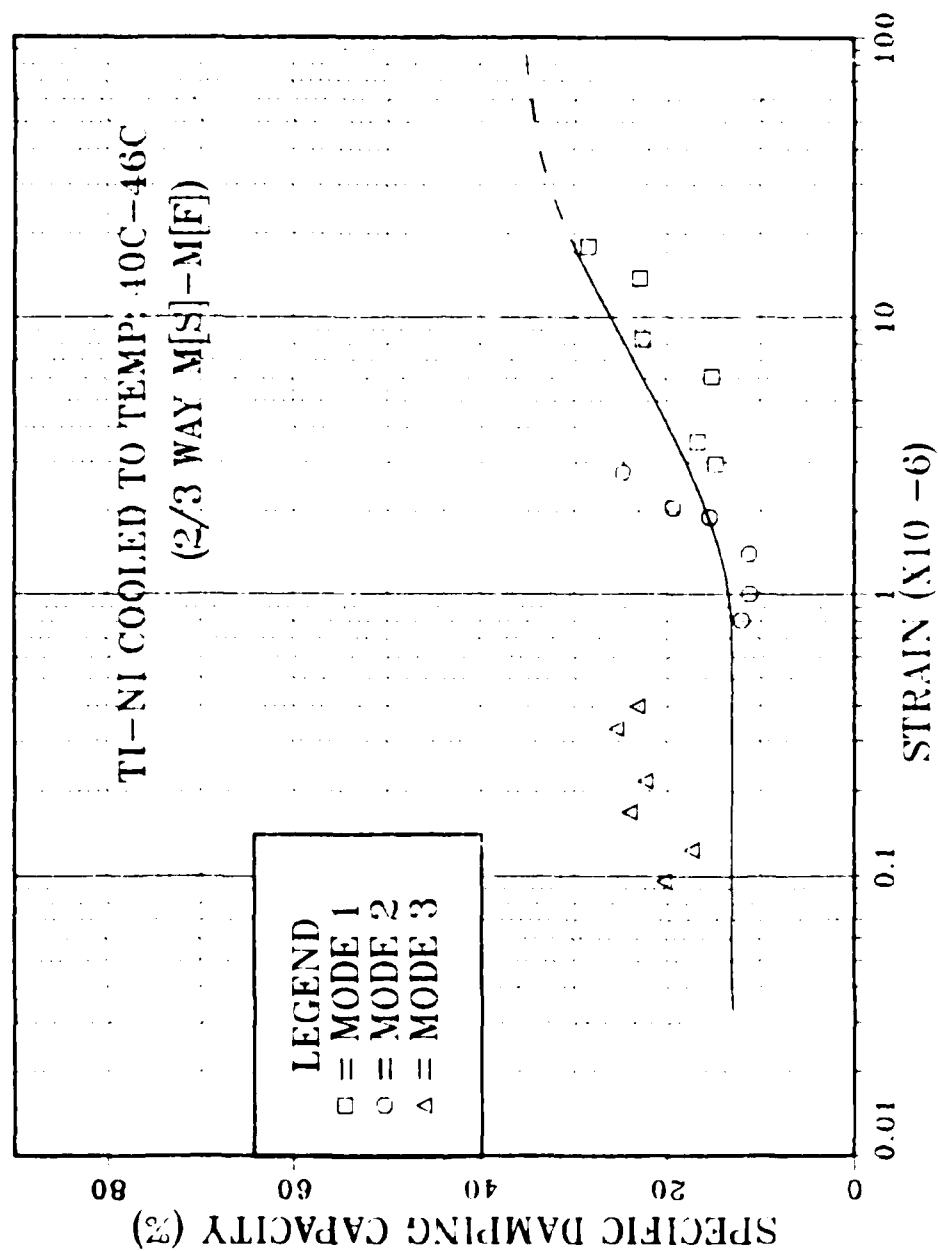


Figure 4.5 Strain Dependence of SDC for Ti-Ni Cooled to 40°-46°C

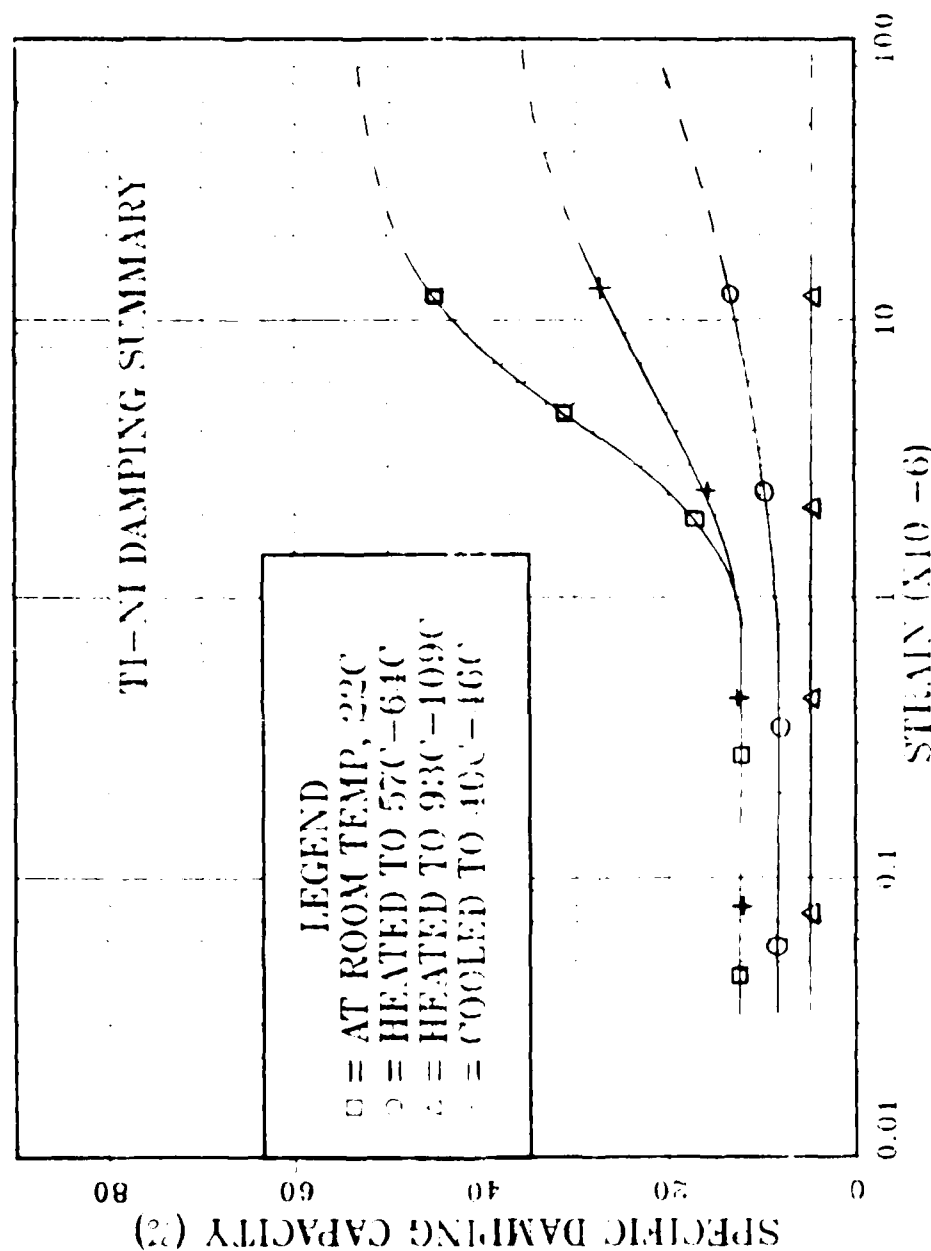


Figure 4.6 Summary of Damping in Ti-Ni as a Function of Cyclic Strain and of Test Temperature



temperature variations while measuring SDC, all at a constant value of cyclic strain. For this experiment, the amplitude of the cyclic strain applied was  $15 \times 10^{-6}$ . The alloy was progressively heated from a temperature just above room temperature to  $102^{\circ}\text{C}$ , and subsequently cooling data was collected. The results of this experiment are plotted in Figure 4.7. On the heating ramp, the SDC remained high and constant until temperature reached approximately  $43^{\circ}\text{C}$ . After that a nearly constant rate of decrease in SDC developed over a temperature range of approximately  $30^{\circ}\text{C}$  width. This was followed by a leveling out of SDC value to a constant at approximately  $87^{\circ}\text{C}$ . Upon cooling, SDC began to increase when temperature dropped to approximately  $76^{\circ}\text{C}$ . Once again, the SDC developed a somewhat steady rate of change for approximately a  $30^{\circ}\text{C}$  wide temperature range. As temperature was reduced to approximately  $32^{\circ}\text{C}$ , SDC re-stabilized. This data represents an SDC hysteresis loop.

It can be seen in Figure 4.7, that the Ti-Ni SDC hysteresis loop provided the potential to maximize the damping ability of the material at a given temperature. If the operating temperature falls within the temperature range of the hysteresis loop, there are two possible SDC's at any given temperature. The SDC value is higher on the heating (upper) portion of the loop than on the cooling (lower) portion. Therefore in order to maximize the damping

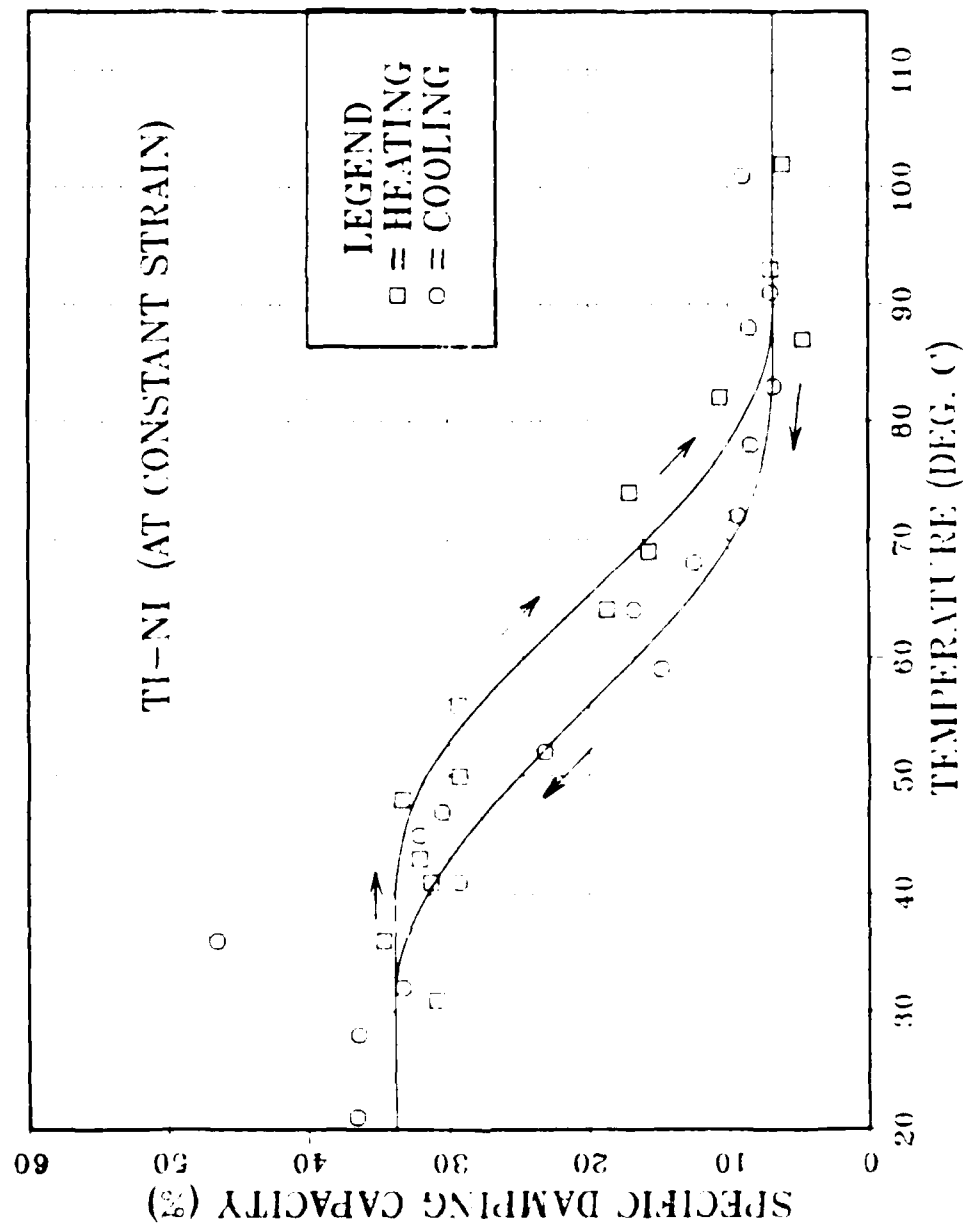


Figure 4.7 SDC Sensitivity to Temperature Change, at a Constant Strain

capacity of the material, the operating temperature should be approached from the low side of the temperature scale.

When comparing the SDC versus temperature data to the calorimetry traces, some interesting observations can be made. The heating portions of Figures 4.1 (calorimetry) and 4.7 (SDC vs. temperature) were plotted together in Figure 4.8. Upon heating SDC began to drop at a temperature which corresponds closely to the austenite start ( $A_S$ ) transformation temperature determined by calorimetry. SDC continued to decrease through the entire martensite-to-austenite phase transformation temperature region. However, it appears that a somewhat elevated level of SDC remains for a small range above the austenite finish ( $A_F$ ) temperature. The cooling portions of Figure 4.1 (calorimetry) and Figure 4.7 (SDC vs. temperature) were plotted together in Figure 4.9. Before the thermally-induced martensitic phase transformation started (i.e., above  $M_S$ ), SDC began to increase. SDC then increased along a sigmoidal curve to a maximum level and stabilized below the martensitic phase transformation finish temperature,  $M_F$ .

The existence of damping capacity outside of the thermally-induced martensite temperature region is remarkable. This SDC is believed to be a result of thermoelastic martensitic transformation induced by the relatively large external stress that was applied.

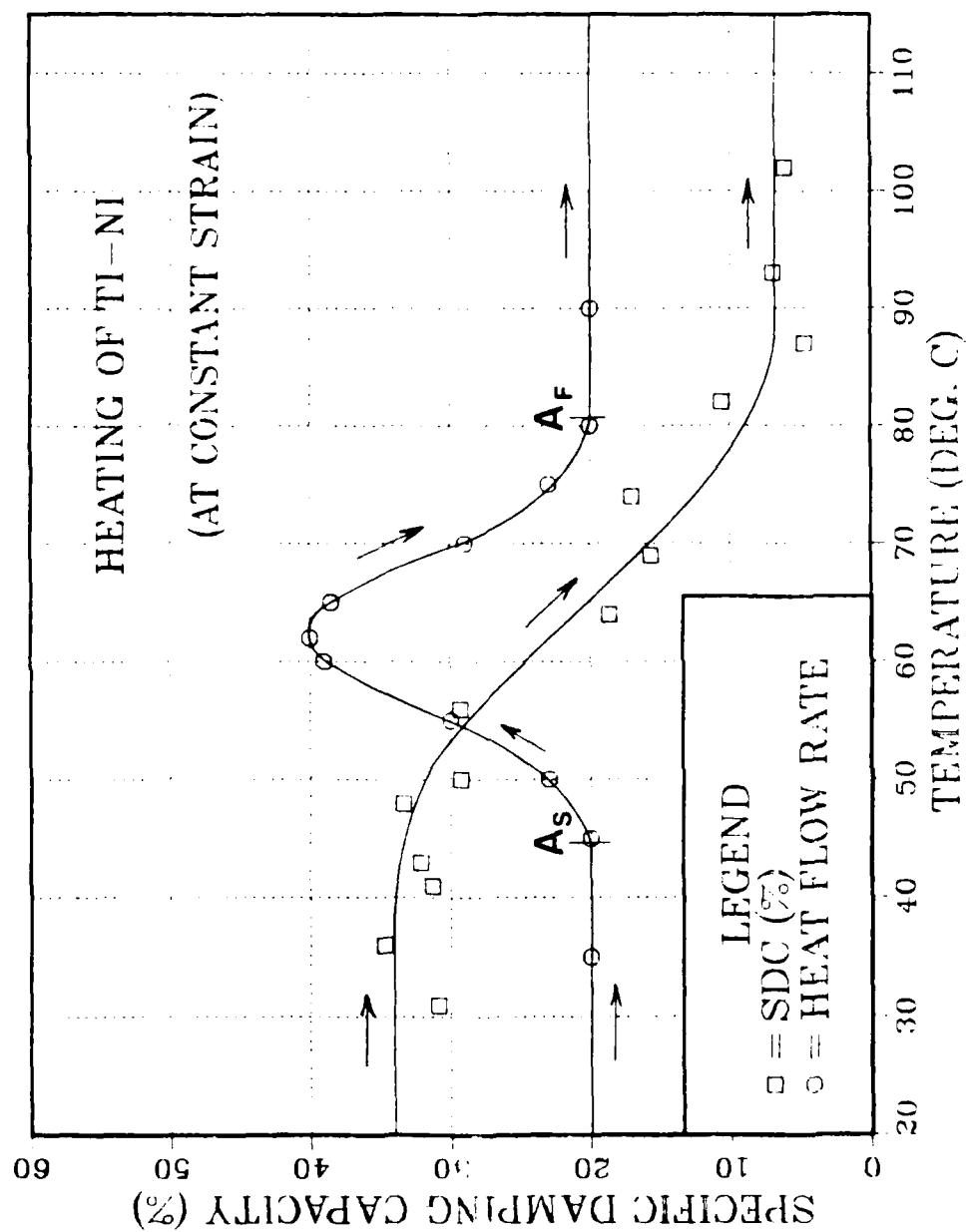


Figure 4.8 Comparison of Heating Portions of Ti-Ni Calorimetry and SDC-Temperature Sensitivity Study

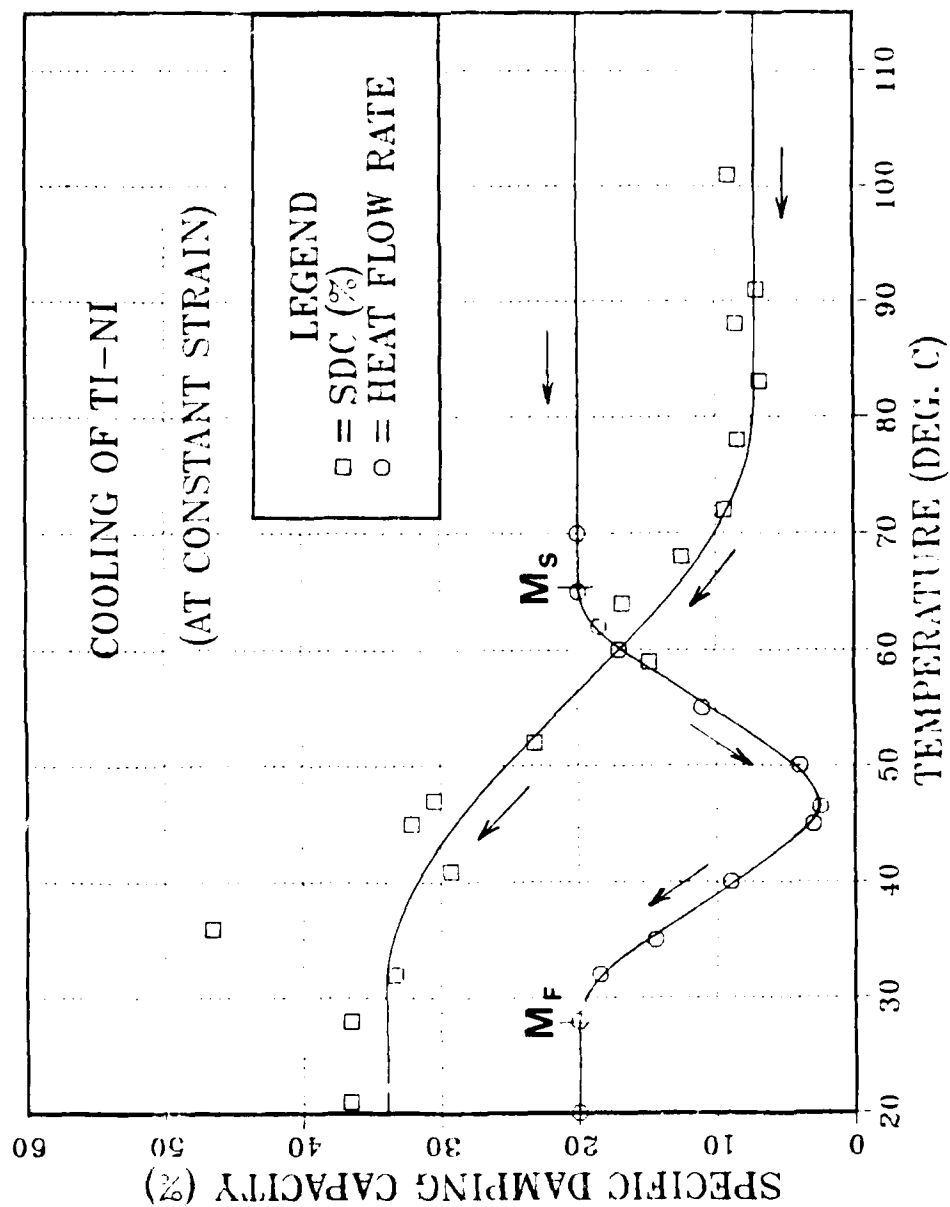


Figure 4.9 Comparison of Cooling Portions of Ti-Ni Calorimetry and SDC-Temperature Sensitivity Study

## 2. Cu-Zn-Al

Differential scanning calorimetry (DSC) provided no indication of a thermally-induced phase transformation of the Cu-Zn-Al alloy microstructure developed for this study. After this, the specific damping capacity (SDC) of the material was measured at room temperature and again at an elevated beam temperature that ranged between 88°C and 105°C. The SDC data (see Figures 4.10 and 4.11) shows that high damping was not provided by this material in this condition. It was later determined that in a previous study of this alloy system, the (high damping) martensitic microstructure was developed only by using a different sequence of cooling from the parent phase, namely a conditioning sequence involving water quenching to 150°C, an isothermal hold for 10 minutes, and then a final quench to room temperature. Thus the direct water quench to room temperature that was utilized in the present study was not a proper treatment to develop the damping microstructure in this alloy system.

### B. INCRAMUTE (CU-MN-AL)

Strain dependence of SDC in this material is shown in Figures 4.12, 4.13, and 4.14. Since aging was expected to occur at or above room temperature, exposure time was monitored relative to the time that the specimen was removed from storage in a freezer. SDC-strain data was first recorded at room temperature (Figure 4.12). Damping

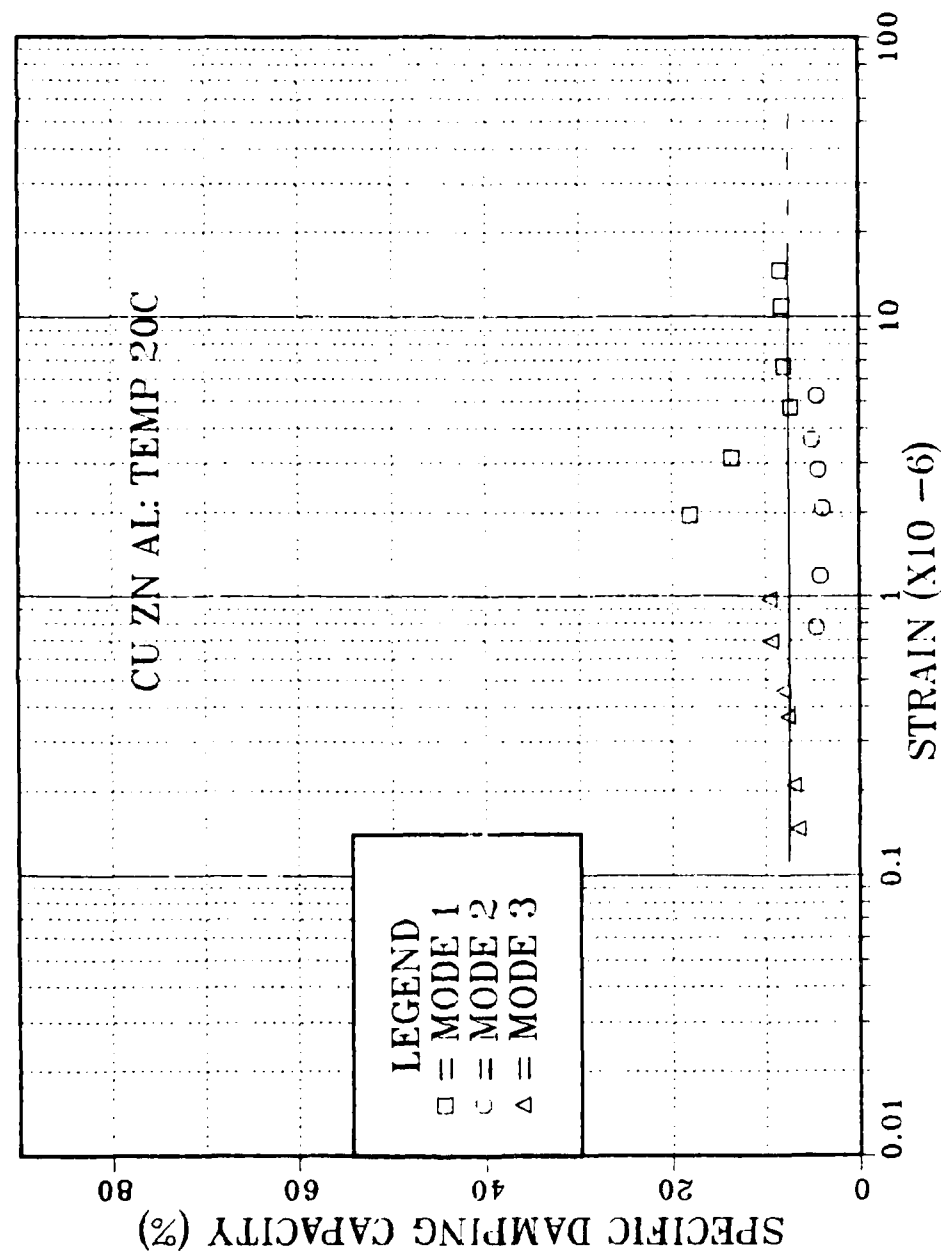


Figure 4.10 Strain Dependence of SDC for Cu-Zn-Al at Room Temperature

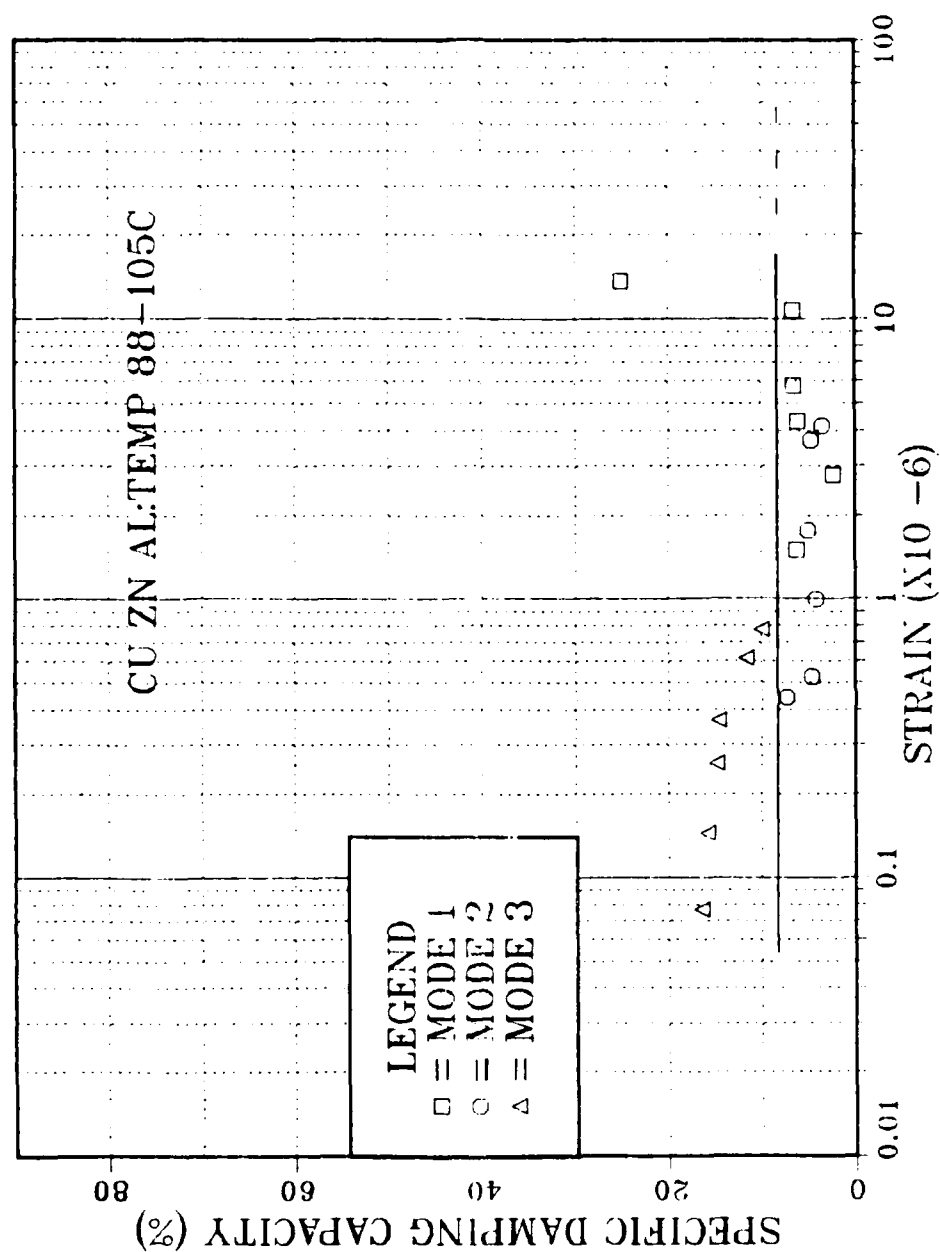


Figure 4.11 Strain Dependence of SDC for Cu-Zn-Al Heated to 88°C-105°C



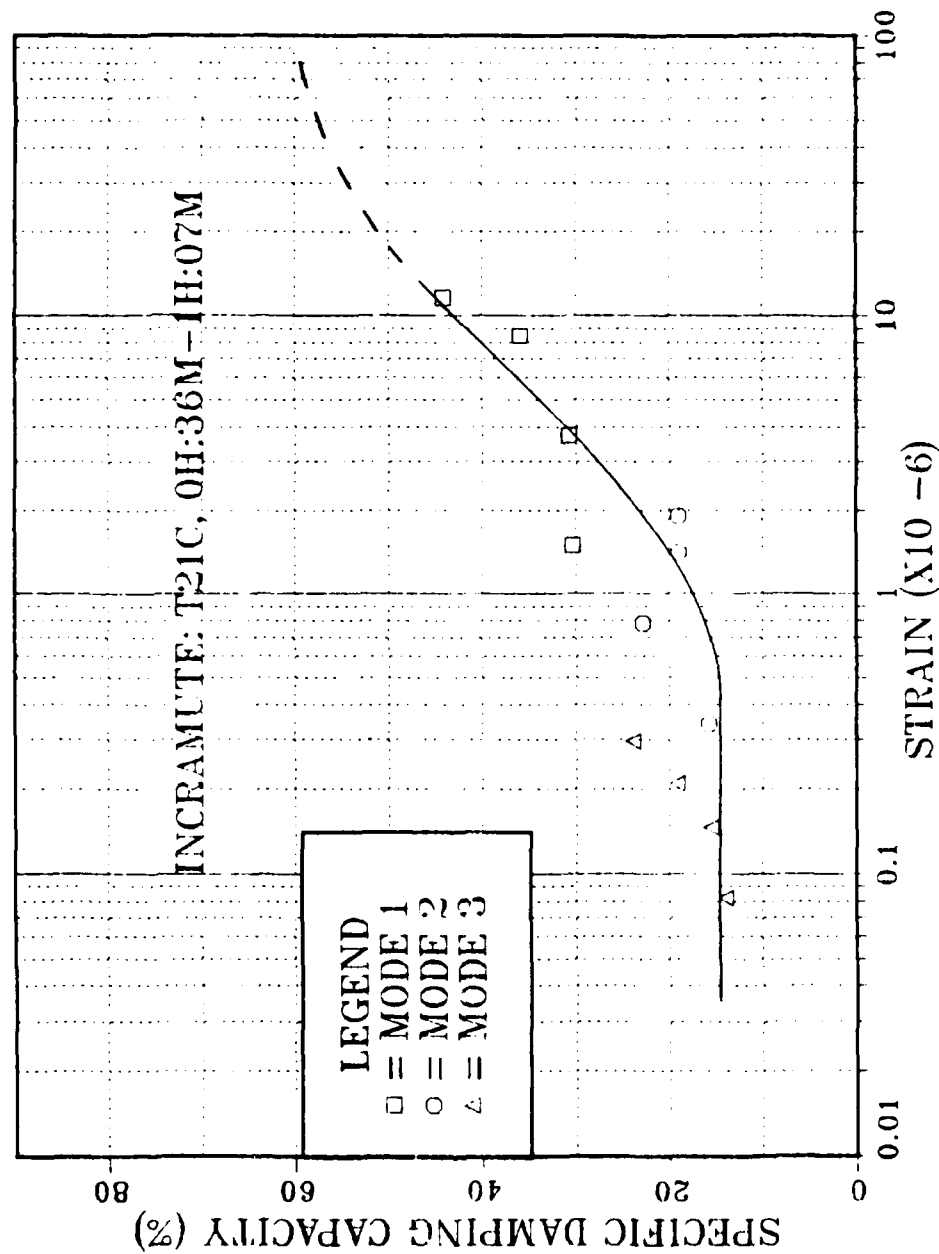


Figure 4.12 Strain Dependence of SDC for INCRAMUTE at Test Temperature 21°C

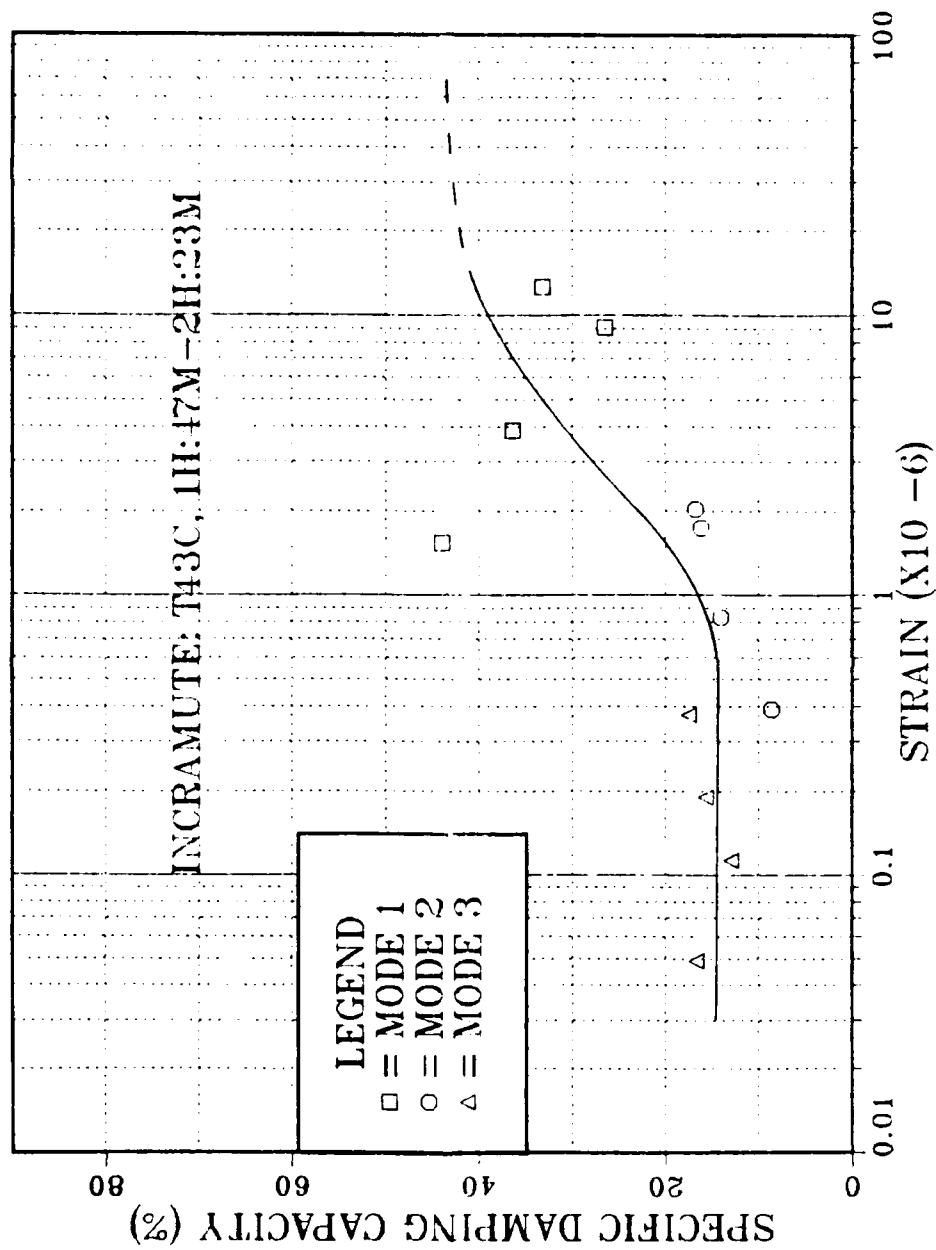


Figure 4.13 Strain Dependence of SDC for INCRAMUTE at Test Temperature 43°C

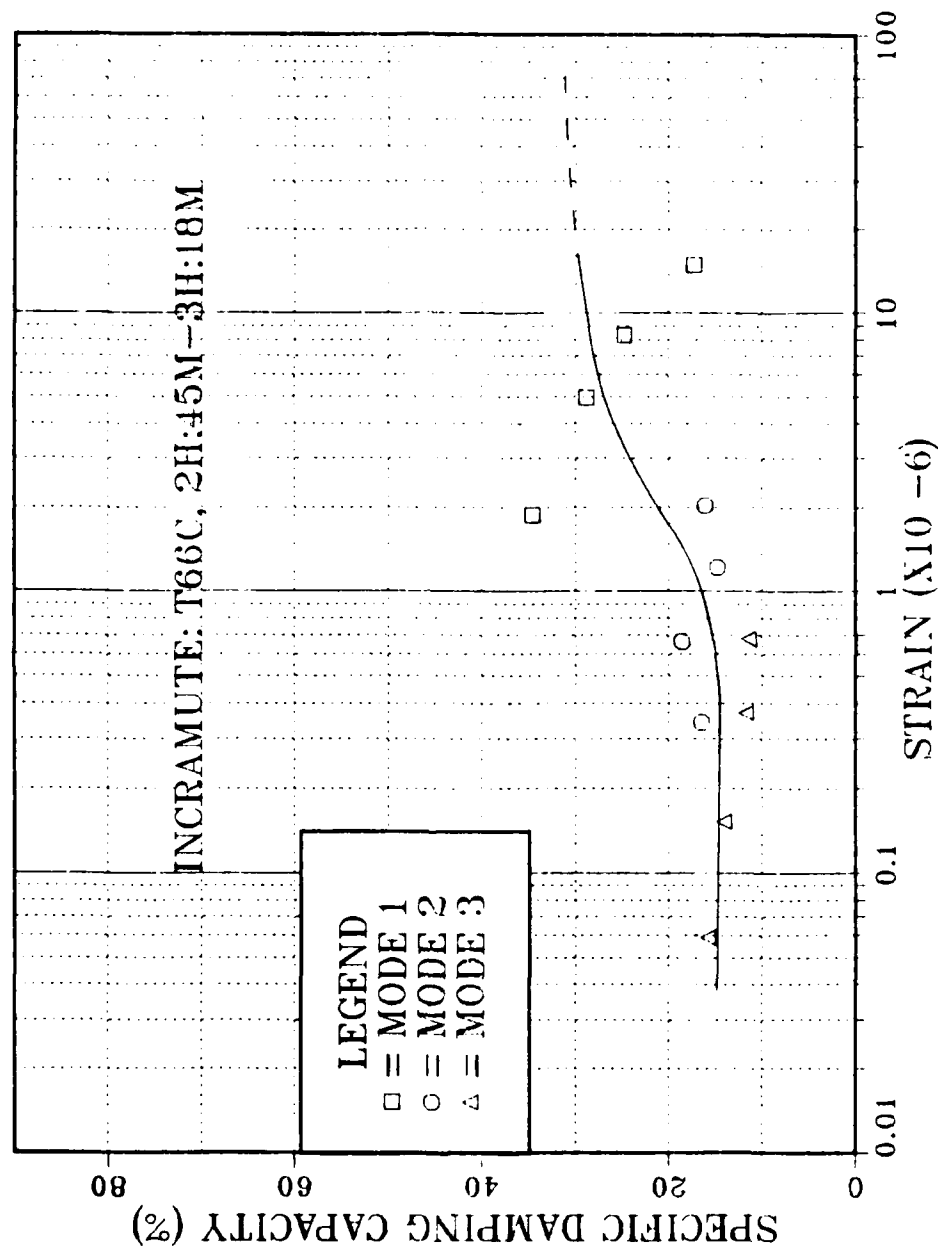


Figure 4.14 Strain Dependence of SDC for INCRAMUTE at Test Temperature 66°C

appeared to be activated by strain at an amplitude of approximately 0.6 microstrains. SDC increased with increasing cyclic strain to the highest magnitude of 44.2% at 11.6 microstrains. Based on previous research [Ref. 23], this trend would be expected to continue until a damping saturation point was reached.

After raising the test temperature to 43°C, the SDC-strain results shown in Figure 4.13 were measured. These indicate activation of the damping mechanism at the same strain amplitude noted in the room temperature test. Again an increasing SDC trend was observed, however the SDC magnitudes appeared to be lower than before.

When the test temperature was elevated to 66°C, the SDC data were as shown in Figure 4.14. Once again higher damping was activated at or near the 0.6 microstrain level. But the SDC magnitudes generated were much lower than at the lower temperatures.

Finally the test temperature was raised to 100°C, and SDC at a constant strain of 15 microstrains was measured relative to exposure time. These results are given in Table IV.

Based on these results it is obvious that aging during initial heat treatment (16 hours at 400°C) was sufficient to raise the FCC to FCT transformation temperature high enough to allow the formation of a high damping microstructure upon quenching. It is thought that the damping mechanism

TABLE IV  
INCRAMUTE'S SDC VARIATION WITH EXPOSURE TIME\*

<u>Exposure Time</u> <u>(hours: minutes)</u>	<u>SDC</u> <u>(%)</u>
2H: 56M	13.1
3H: 06M	12.1
3H: 28M	15.6
6H: 06M	16.9
7H: 15M	8.4

\*Temperature = 100°C and Strain =  $15 \times 10^{-6}$ .

activated by the cyclic stress was a cooperative realignment of the FCT microstructure. Additionally, it is clear that SDC magnitudes (observed in Figures 4.12, 4.13, 4.14, and Table IV) are sensitive to aging time at room temperature and/or test temperature. Further research is in order to determine which of these is the dominating factor and specifically what effect these factors have on the material's microstructure.

#### C. FE-CR-MO

Based on the Fe-Cr binary phase diagram (Figure 1.4), indications are that the alloy will undergo a magnetic transformation as it passed through the Curie temperature (approximately 725°C for this alloy).

The strain dependence of specific damping capacity (SDC) in this material was measured at room temperature and at

three other temperatures up to and including 109°C (see Figures 4.15 through 4.18). In each case the Fe-Cr-Mo alloy proved to be a highly capable damping material exhibiting SDC as high as 60-65% at cyclic strain amplitudes of about  $5 \times 10^{-6}$ . This expected trend of SDC stability should continue at temperatures up to the Curie temperature, after which the damping ability would vanish as the material transformed to a paramagnetic state.

Each plot of the strain dependence of SDC in this alloy revealed a common SDC-activation strain amplitude of approximately  $0.2 \times 10^{-6}$ . All data showed a trend of increasing SDC as cyclic strain amplitudes increased. The primary damping mechanism at work here is thought to be magnetostriction. This is an irreversible strain and an associated change in material magnetization. This results in the ordering of magnetic domains in the direction of resultant strain and in magneto-mechanical hysteresis energy loss (i.e., damping). A secondary damping mechanism is stress-induced dislocation motion.

Upon consideration of the damping in operation, it is expected that a peak in SDC with increasing strain would eventually occur. Some sort of damping saturation condition would develop in which movement of magnetic domain walls and dislocations would be inhibited. It is felt that this behavior could have been proven had the test equipment been capable of generating larger cyclic strains.

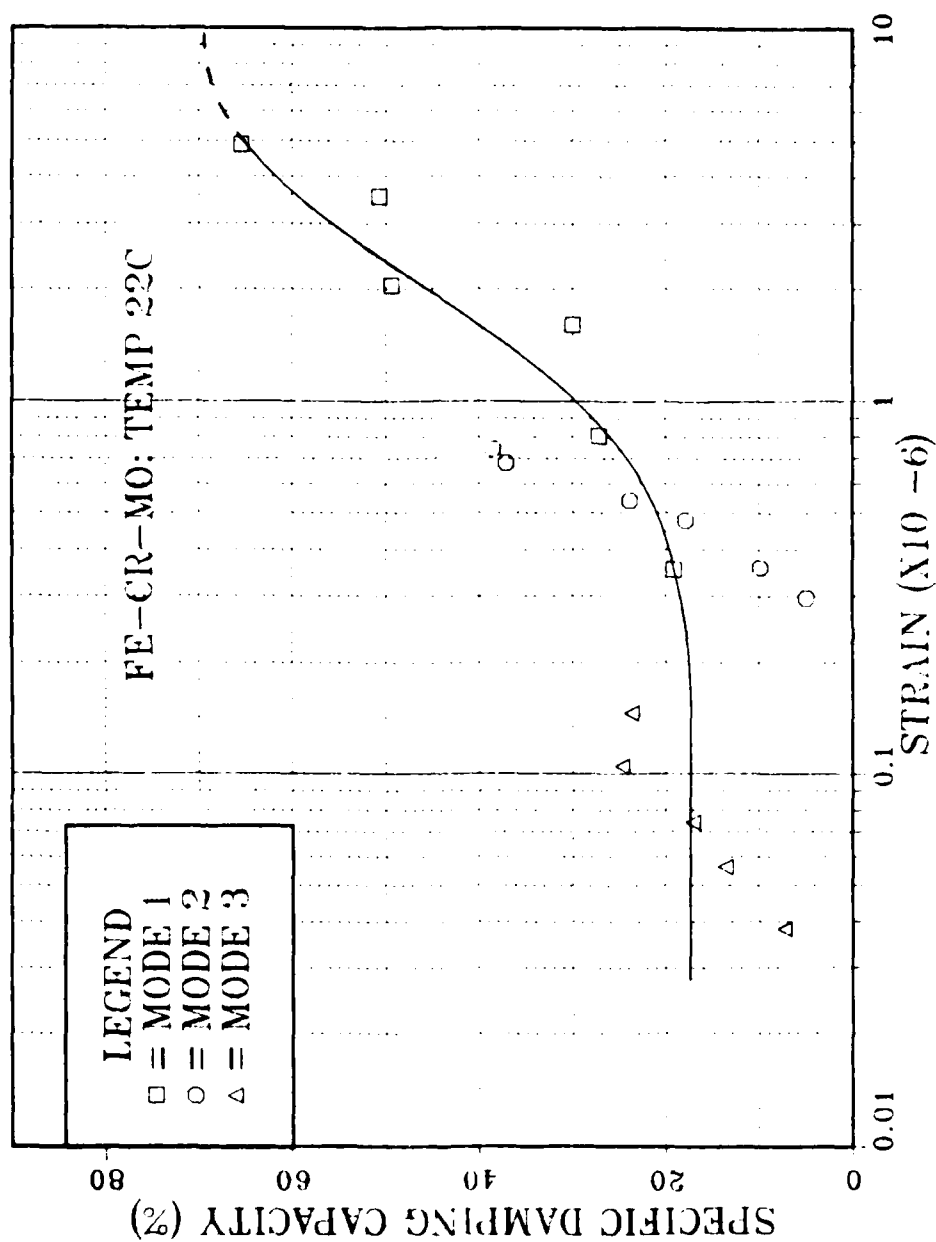


Figure 4.15 Strain Dependence of SDC for Fe-Cr-Mo at Room Temperature

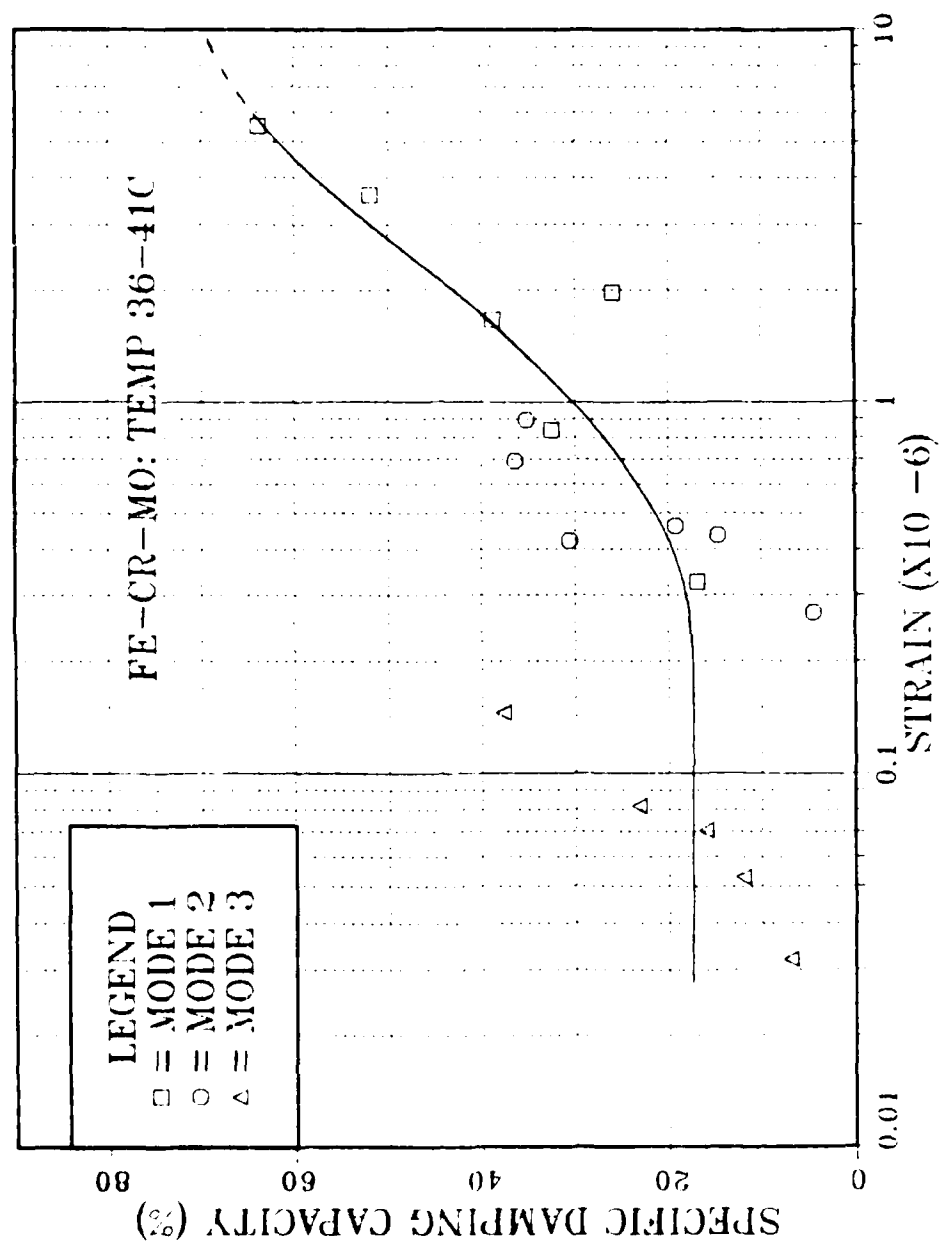


Figure 4.16 Strain Dependence of Fe-Cr-Mo Heated to 36°C-41°C



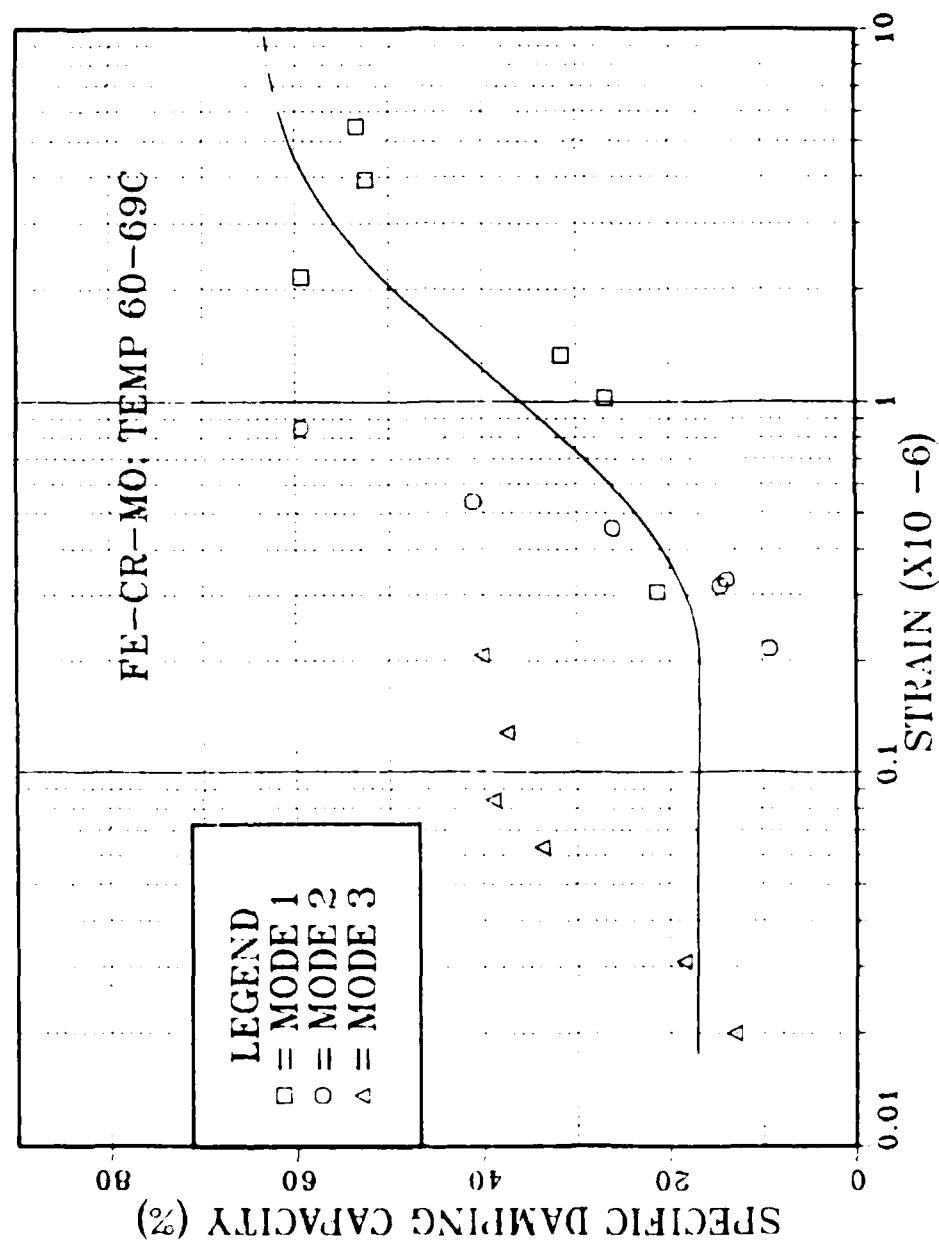
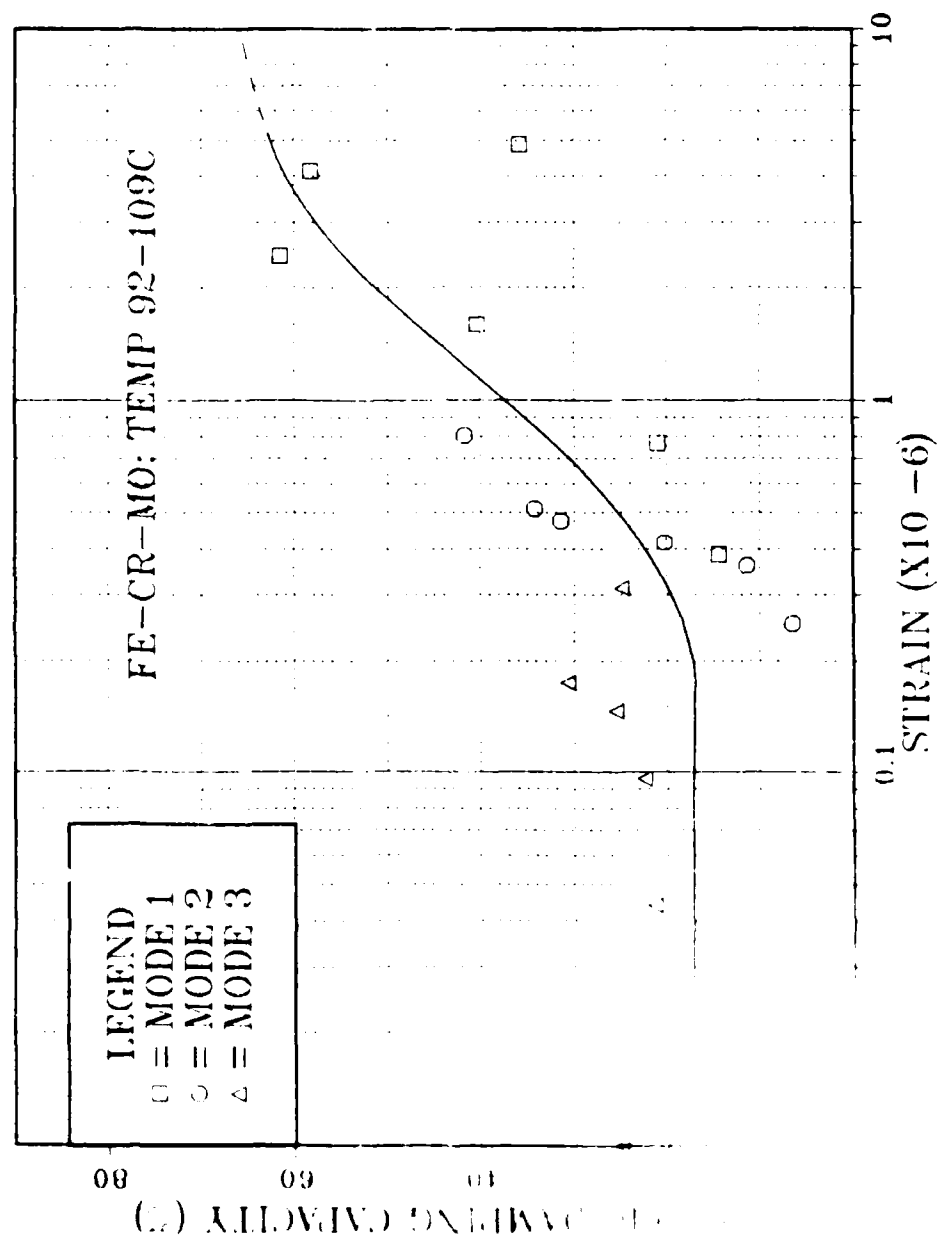


Figure 4.17 Strain Dependence of Fe-Cr-Mo Heated to 60°C-69°C



Dependence of Fe-Cr-Mo Heated to 92°C-109°C

AD-A184 118

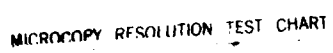
A COMPARISON OF HIGH DAMPING SHAPE MEMORY ALLOYS WITH  
CU-NI-BASED AND FE-CR-BASED ALLOYS(U) NAVAL  
POSTGRADUATE SCHOOL MONTEREY CA J T CRONAUER JUN 87

2/2

UNCLASSIFIED

F/G 11/6.1 NL





#### D. 1020 STEEL

As a basis of comparison with a "normal" the strain dependence of 1020 Steel at room temperature is shown in Figure 4.19. This data, on a well-known "low-damping" material are provided to contrast the SDC magnitudes of the shape memory alloys and the Cu-Mn-based and Fe-Cr-based quiet metal alloys.

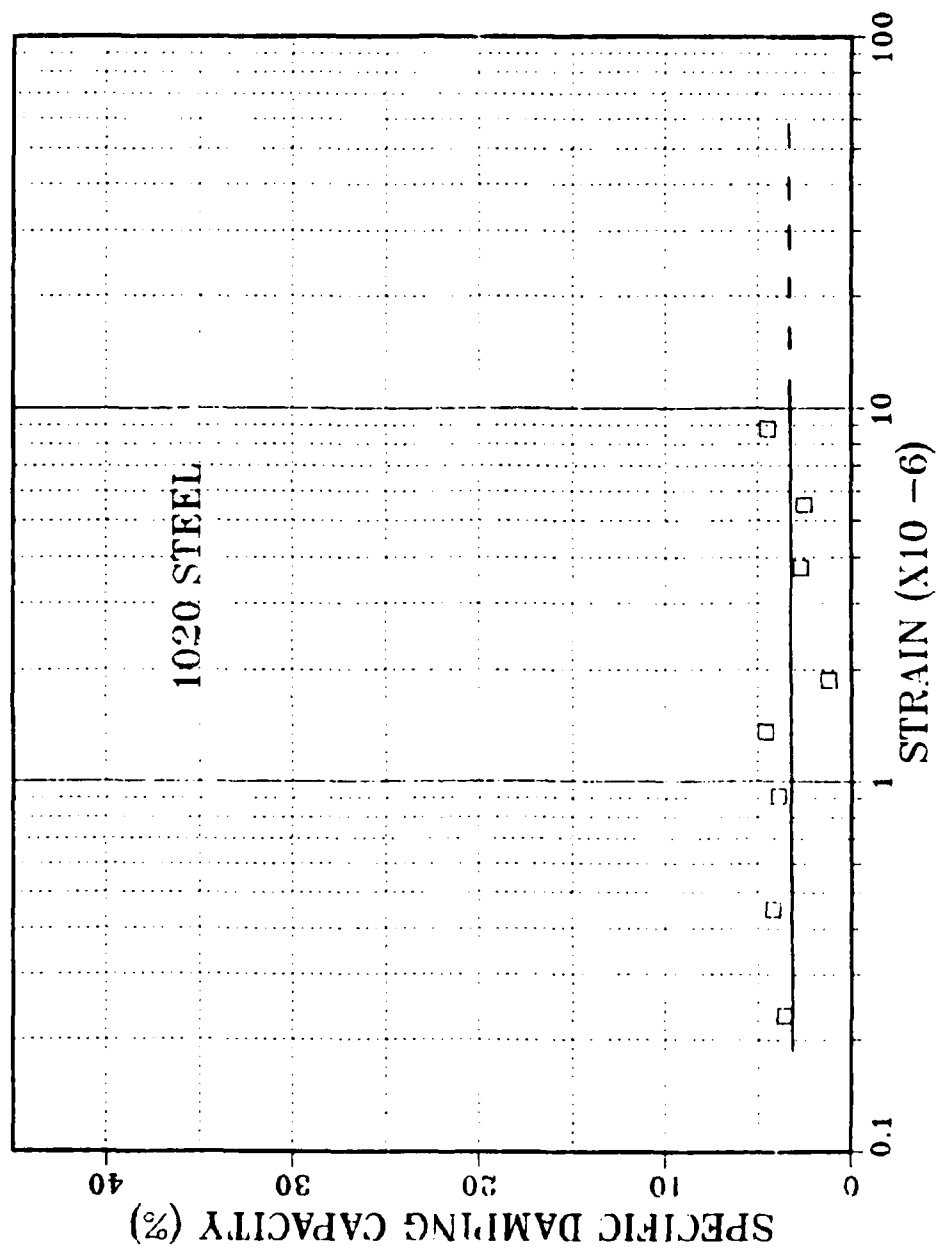


Figure 4.19 Strain Dependence of SDC for 1020 Steel at Room Temperature

## V. CONCLUSIONS

The following conclusions are presented for this research:

- (1) The experimental technique that has been developed to study the damping behavior of materials is accurate and reproducible. However, at present, an equipment capacity limitation prevents generation of cyclic strain amplitudes large enough to fully study potential damping saturation effects in some quiet metal alloys.
- (2) Damping in the Ti-Ni-alloy was found to be directly related to the progress of martensitic transformation. Thus damping capacity was characterized as being sensitive to both temperature and cyclic strain amplitude. Although a high damping capacity was developed at relatively low cyclic strain amplitudes, this capacity (at a constant strain) was shown to fall off rapidly over a temperature range only about 45°C in width. Therefore some good engineering work would be required to strike a balance between these parameters and maximize the damping potential of this Ti-Ni-based alloy for practical applications.
- (3) The Cu-Zn-Al alloy studied was not conditioned properly to develop the thermoelastic martensitic microstructure required for high damping shape memory behavior.
- (4) The previously determined optimum damping behavior in Cu-Mn-Al and Fe-Cr-Mo alloy systems was reproduced and verified.
- (5) Investigation of the damping behavior of the Cu-Mn-Al alloy in the present research was not sufficient to determine whether it was a change in test temperature or the effects of time at temperature that cause this alloy to lose its damping capacity.
- (6) The Fe-Cr-Mo alloy possessed a high damping potential that was activated at relatively low cyclic strain amplitudes and was insensitive to temperature changes up to 110°C. This insensitivity to temperature is expected to remain up to approximately 700°C.

## VI. RECOMMENDATIONS FOR FURTHER STUDY

The following recommendations for further research are provided:

- (1) Obtain a higher-powered electromagnetic shaker, capable of generating higher strain amplitudes, and thereby allowing study of damping saturation behavior in materials. An alternative may be to investigate other types of excitation signals (for example swept sine wave), which might generate greater strain amplitudes.
- (2) Develop a method of integrating a larger computer system (and its associated memory capacity) into the present damping technique. This would provide rapid access to memory for all data produced for various alloys by different studies. It also may provide the potential to program the computer to numerically manipulate the raw damping data. The elimination of manual data manipulation promises great savings in overall testing time.
- (3) Determine the optimum high damping conditioning treatment for the Cu-Zn-Al alloy, and subsequently compare that optimum damping behavior with that of other high damping alloys.
- (4) Continue investigating damping behavior in the Cu-Mn-Al alloy by isolating the effects of temperature (i.e., SDC versus temperature, at a constant strain) and of time at temperature (i.e., SDC versus strain, at a constant temperature, at recorded time intervals).



### LIST OF REFERENCES

1. Schetky, L.M. and Perkins, J., "The 'Quiet' Alloys," Machine Design, pp. 202-206, 6 April 1978.
2. Bert, C.W., "Material Damping: An Introductory Review of Mathematical Models, Measures and Experimental Techniques," Journal of Sound and Vibration, Vol. 29, No. 2, pp. 129-153, 1973.
3. Thomson, W.T., Theory of Vibration with Applications, Prentice-Hall, Inc., 1981.
4. de Batist, R., Internal Friction of Structural Defects in Crystalline Solids, North-Holland publishing Co., Amsterdam, 1972.
5. Reed-Hill, R.E., Physical Metallurgical Principles, Brooks/Cole Engineering Div., 1973.
6. Bolt, Beranek, and Newman, Inc., Cambridge, Massachusetts, "Operations Manual for the Bolt, Beranek, and Newman, Inc., Resonant Dwell Apparatus," January 1973.
7. Sugimoto, K., "Internal Friction Phenomena Associated with Diffusionless Phase Transformations in Alloys," Journal de Physique, Vol. 42, pp. C5-971--C5-982, October 1981.
8. de Batist, R., "High Damping Materials: Mechanisms and Applications," Journal de Physique, Vol. 44, pp. C9-39--C9-50, December 1983.
9. Kennon, N.F. and Dunne, D.P., "Shape Memory Behaviour," Metals Forum, Vol. 4, No. 3, pp. 130-134, 1981.
10. Olson, G.B. and Cohen, M., "Thermoelastic Behavior in Martensitic Transformations," Scripta Metallurgica, Vol. 9, p. 1247, 1975.
11. Adachi, K., Perkins, J., and Wayman, C.M., "Type II Twins in Self-Accommodating Martensite Plate Variants in a Cu-Zn-Al Shape Memory Alloy," Acta Metallurgica, Vol. 34/12, pp. 2471-2485, 1986.
12. Dean, R.S., Long, J.R., Graham, T.R., Roberson, A.H., and Armantrout, C.E., "The Alpha Solid Solution of the Copper-Manganese-Aluminum System," Transactions of the AIME, Vol. 171, pp. 70-88, 1947.

13. Vintaykin, Ye. Z., Litvin, D.F., and Udovenko, V.A., "Fine Crystalline Structure in Highly Shock-Absorbing Alloys of Manganese and Copper," Physics of Metals and Metallography (in Russian, Fiz. metal. metalloved.), Vol. 37, No. 6, pp. 1228-1237, 1974.
14. Bichinashvili, A.J., Vintaykin, Ye. Z., Litvin, D.F., and Udovenko, V.A., "X-Ray Investigation of the FCC-FCT Transformation in Manganese Copper Alloy," Physics of Metals and Metallography (in Russian, Fiz. metal. metalloved.), Vol. 41, No. 1, pp. 112-117, 1976.
15. Vintaykin, Ye. Z., Dmitriyev, V.B., and Udovenko, V.A., "Antiferromagnetism in Heterogeneous Manganese-Copper Alloys," Physics of Metals and Metallography (in Russian, Fiz. metal. metalloved.), Vol. 44, No. 5, pp. 107-113, 1979.
16. Vitek, J.M. and Warlimont, H., "On a Metastable Miscibility Gap in  $\gamma$ -Mn-Cu Alloys and the Origin of Their High Damping Capacity," Metal Science, Vol. 10, No. 1, pp. 7-13, January 1976.
17. Men'shikov, A.Z., Favstov, Yu. K., Kochetkova, L.P., Konoplev, L.M., and Dorofeyev, Yu. A., "Structural Transformations During the Tempering of High-Damping Manganese-Copper Alloys," Physics of Metals and Metallography (in Russian, Fiz. metal. metalloved.), Vol. 39, No. 4, pp. 793-800, 1975.
18. Guseva, L.N., Dolinskaya, L.K., and Skurikhin, M.N., "Aging of Alloy Cu + 72% Mn Alloyed with Nickel, Iron and Aluminum," Izvestiya Akademii Nauk SSSR. Metallurgy, No. 6, pp. 138-142, 1984.
19. Birchon, D., Bromley, D.E., and Healey, D., "Mechanism of Energy Dissipation in High-Damping-Capacity Manganese-Copper Alloys," Metal Science Journal, Vol. 2, pp. 41-46, 1968.
20. Hedley, J.A., "The Mechanism of Damping in Manganese Copper Alloys," Metal Science Journal, Vol. 2, pp. 129-137, July 1968.
21. Butler, E.P. and Kelly, P.M., "High Damping Capacity Manganese-Copper Alloys. Part I--Metallography," Transactions of the Metallurgical Society of AIME, Vol. 242, pp. 2099-2106, October 1968.
22. Butler, E.P. and Kelly, P.M., "High Damping Capacity Manganese-Copper Alloys," Proceedings of Sixth International Congress for Electron Microscopy, Kyoto, Maruzen Co., Ltd., Nihonbashi, Tokyo, pp. 451-452, 1966.

23. Reskusich, J. and Perkins, J., "Damping Behavior of INCRAMUTE: Strain Dependence and Heat Treatment Effects," Naval Postgraduate School Technical Report No. NPS 69-87-001, Monterey, California, September 1986.
24. Barrett, C.R., Nix, W.D., and Tetelman, A.S., The Principles of Engineering Materials, Prentice-Hall, Inc., 1973.
25. Schilling, J.W. and Houze, G.L., "Magnetic Properties and Domain Structure in Grain-Oriented 3% Si-Fe," IEEE Transactions on Magnetics, Vol. MAG-10, No. 2, pp. 195-222, June 1974.
26. Schneider, W., Schrey, P., Hausch, G., and Torok, E., "Damping Capacity of Fe-Cr and Fe-Cr Based High Damping Alloys," Journal De Physique, Colloque C5, Supplement au no. 10, Tome 42, pp. C5-C35, October 1981.
27. DeGauque, J., Astie, B., and Kubin, L.P., "Evidence for the Interaction Between Magnetic Domain Walls and Dislocations in High-Purity Iron from Magnetomechanical Damping Experiments," Phys. Stat. Sol., Part A, Vol. 45, pp. 493-501, 1978.
28. Metals Handbook, 8th ed., Vol. 8, American Society for Metals, 1973.
29. Peckner, D. and Bernstein, I.M., Handbook of Stainless Steels, McGraw-Hill, Inc., 1977.
30. O'Toole, J.F. and Perkins, J., "Damping Behavior of an Fe-Cr-Mo Alloy: Strain Dependence and Heat Treatment Effects," Naval Postgraduate School Technical Report No. NPS 69-87-002, Monterey, California, December 1986.
31. The Perkin-Elmer Corporation, Norwalk, Connecticut, "Instructions Model DSC-2 Differential Scanning Calorimeter," 1979.
32. Measurements Group, Inc., Raleigh, North Carolina, "BAM-1 Bridge Amplifier and Meter Instruction Manual," 1976.
33. Hewlett-Packard Co., Palo Alto, California, "The Fundamentals of Modal Testing, Application Note 243-3," 1986.
34. Scientific Atlanta Spectral Dynamics Division, "Using the SD380 for Structural Measurements," 1986.

INITIAL DISTRIBUTION LIST

	No. Copies
1. Defense Technical Information Center Cameron Station Alexandria, Virginia 22304-6145	2
2. Library, Code 0142 Naval Postgraduate School Monterey, California 93943-5002	2
3. Department Chairman, Code 69Hy Department of Mechanical Engineering Naval Postgraduate School Monterey, California 93943-5000	1
4. Professor A.J. Perkins, Code 69Ps Department of Mechanical Engineering Naval Postgraduate School Monterey, California 93943-5000	10
5. Professor Y.S. Shin, Code 69Sg Department of Mechanical Engineering Naval Postgraduate School Monterey, California 93943-5000	1
6. Lt. Joseph T. Cronauer, USN 803 Market Street Summerhill, Pennsylvania 15958	4
7. Mr. Robert Hardy, Code 2803 David W. Taylor Naval Ship R&D Center Annapolis, Maryland 21402	5
8. Ms. Cathy Wong, Code 2812 David W. Taylor Naval Ship R&D Center Annapolis, Maryland 21402	5

END

10-87

DTIC